

TOPICS IN DESIGNING LOW THERMAL EXPANSION LATTICES AT THE
MICROSCALE

by

John Chu

A thesis submitted in conformity with the requirements
for the degree of Master of Applied Science
Graduate Department of Aerospace Science and Engineering
University of Toronto

Copyright © 2011 by John Chu

Abstract

Topics in Designing Low Thermal Expansion Lattices at the Microscale

John Chu

Master of Applied Science

Graduate Department of Aerospace Science and Engineering

University of Toronto

2011

Microscale bi-material lattices with near zero thermal expansion are designed to create a thermally stable optical surface for applications in a space telescope. To facilitate the design, the thermal expansion of a unit cell with spacers is derived analytically and validated via finite element studies. Predicting the lattice behaviour also requires knowledge of the constituent properties. To this end, molecular dynamics simulations are performed to determine the thermal expansion and recrystallization behaviour of aluminum and titanium thin films, and nanoindentation experiments are conducted to extract their elastic-plastic properties. Unit cell configurations giving near zero thermal expansion are obtained through iterative analysis. The resulting designs are analyzed and validated via finite element simulations and shown to exhibit long term stability.

Acknowledgements

I would like to express my thanks and gratitude to Professor Craig A. Steeves for his help and guidance in completing this thesis. His encouragements and suggestions have been tremendously helpful over the course of my research. I would also like to thank Professor Prasanth B. Nair for being the second reader of this document.

This thesis has been made possible due to the work by our collaborators at the California Institute of Technology. I would like to thank Professor Chiara Daraio, Professor Abha Misra, and Eleftherios Gdoutos for their contributions toward my research and hospitality during my brief visits.

Last but not least, I would like to thank my family and friends for their help and encouragement in my studies. Special thanks goes to Serena Lee who has provided me with inspiration and unwavering support throughout my endeavour.

Financial assistance for this work has been jointly provided by the Keck Institute for Space Studies and the University of Toronto Institute for Aerospace Studies.

Computational resources for the work in this thesis were provided by the SciNet HPC Consortium, funded by the Canada Foundation for Innovation under the auspices of Compute Canada, the Government of Ontario, Ontario Research Fund - Research Excellence, and the University of Toronto.



JOHN CHU

University of Toronto Institute for Aerospace Studies

April 15, 2011

Contents

1	Introduction	1
1.1	Background Information	1
1.1.1	Low Thermal Expansion Materials	1
1.1.2	Properties of Bi-material Lattices	3
1.2	Motivation and Scope of Research	5
1.3	Thesis Organization	7
2	Analytical and Numerical Study of Spacers	8
2.1	Low Thermal Expansion Lattices	8
2.1.1	Pinned Joint Lattices	9
2.1.2	Bonded Joint Lattices	10
2.1.3	New Lattice Geometry	12
2.2	Analytical Study	14
2.2.1	Thermal Expansion of New Geometry Assuming Pinned Joints . .	14
2.2.2	Thermal Expansion of New Geometry Assuming Bonded Joints .	19
2.3	Numerical Investigation	26
2.3.1	Finite Element Model	26
2.3.2	Results and Comparison	28
3	Molecular Dynamics Study of Amorphous Materials	34
3.1	Overview of Molecular Dynamics	34
3.1.1	Background Information and Applications	34
3.1.2	Governing Equations	35
3.1.3	Interatomic Potentials	37
3.1.4	Limitations	39
3.1.5	Parallel MD Codes and Scalability	40

3.2	Thermal Expansion and Recrystallization of Amorphous Al and Ti	42
3.2.1	Literature Review	42
3.2.2	Simulation Method	44
3.2.3	Results and Discussion	50
4	Mechanical Properties of Al and Ti Thin Films	61
4.1	Identifying Material Properties via Nanoindentation	61
4.1.1	Young's Modulus	61
4.1.2	Plastic Properties	65
4.2	Elastic-Plastic Properties of Al and Ti Thin Films	68
4.2.1	Experimental Method and Analysis	68
4.2.2	Results and Discussion	70
5	New Lattice Configuration with Low Thermal Expansion	76
5.1	Lattice Design	76
5.1.1	Configuration Assuming Nanocrystalline Films	77
5.1.2	Configuration Assuming Amorphous Films	78
5.2	FE Analysis of Lattice	79
5.2.1	Method	79
5.2.2	Results and Discussion	81
6	Conclusions	87
6.1	Summary of Research	87
6.2	Recommendations for Future Work	88
	Bibliography	88

Chapter 1

Introduction

1.1 Background Information

1.1.1 Low Thermal Expansion Materials

Materials with low thermal expansion are desirable in situations where there are large variations and gradients in temperature. Systems in extreme thermal environments are susceptible to large thermal strains and thermo-mechanical fatigue which may ultimately lead to structural failure. Variations in temperature can also lead to unwanted geometric changes in sensitive applications requiring very fine precision. Systems in space are particularly vulnerable to large temperature changes when passing in and out of sunlight. The exterior surfaces of space vehicles are also subject to extremely high temperatures upon atmospheric re-entry.

To preserve structural stability and reduce thermal stresses, it is desirable to employ materials that have a low coefficient of thermal expansion (CTE). In addition to minimal CTE, a candidate material must also exhibit sufficient rigidity and robustness to bear loads. Materials that have all of the aforementioned properties, however, do not currently exist. Figure 1.1 plots the families of structurally robust materials in the space of stiffness and thermal expansion. Ceramics are not included in this graph because they are brittle and prone to cracking. Invar, an iron-nickel alloy, is noted for having an anomalously low CTE, roughly 1 part per million per Kelvin (ppm/K). It is both stiff and robust, however its property of low thermal expansion is only observed at temperatures below 373 K [20]. Carbon composites have high stiffness and low CTE over a wide temperature range when used in a matrix, but robustness issues and fabrication complexities limit its application

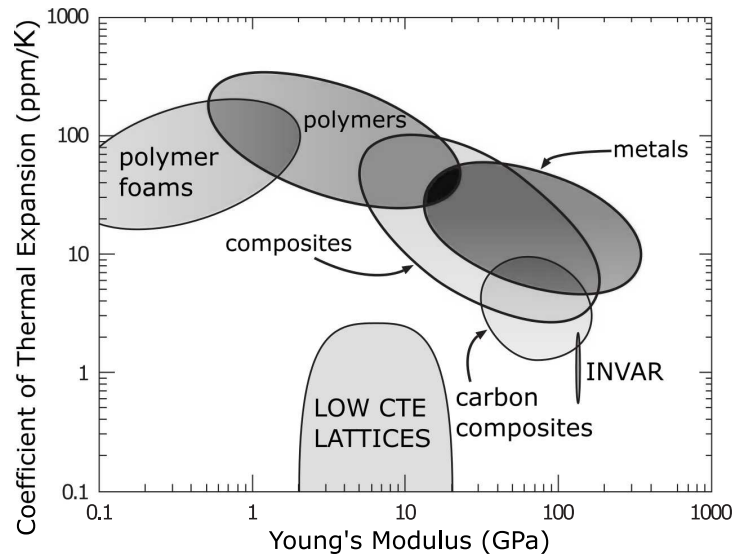


Figure 1.1: Young's modulus and CTE range of various structurally robust materials (excluding ceramics) adapted from Steeves et al. [61].

[61]. Metals and composites have similar characteristics; both materials have moderate to high stiffness and thermal expansion. As seen in Figure 1.1, polymers and polymer foams have very large CTEs and are also lacking in rigidity. Bi-material lattices have been proposed as a new family of materials with low thermal expansion that are both stiff and robust, thus solving the deficiencies encountered with other materials. Starting with rigid and reliable metals, a lattice composed of two constituents with empty space is designed such that its overall thermal expansion is below that of either material. By using components with widely varying CTEs, the thermal expansion of the members are accommodated through rotations at the joints. Depending on the materials used and the geometry of the bi-material lattice, the CTE can be tailored according to the needs of a given application.

Low thermal expansion lattices have been proposed and studied by other researchers, most notably by Lakes [38], Sigmund and Torquato [58], Jefferson et al. [33], and Steeves et al. [61], whose unit cell configurations are shown in Figure 1.2. All four designs incorporate two materials with high and low thermal expansion as illustrated by the red and blue members respectively. The lattice by Lakes [38] was created to have arbitrarily large thermal expansion, but can also be designed to have a CTE of zero. It has, however, poor stiffness qualities and strength since the members support mechanical loads through bending. Sigmund and Torquato [58] used topology optimization to design a bi-material

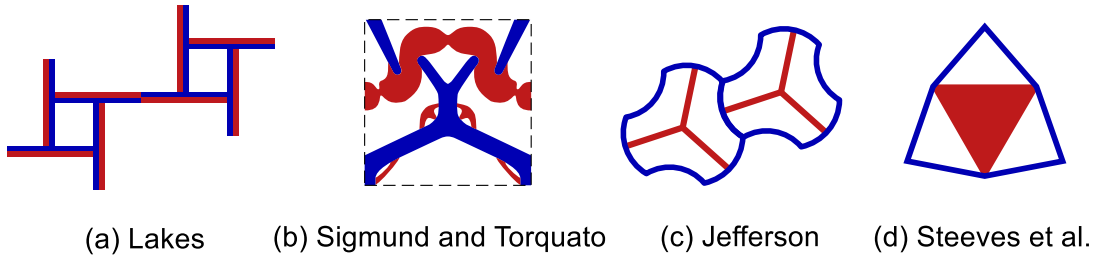


Figure 1.2: Unit cells by (a) Lakes [38], (b) Sigmund and Torquato [58], (c) Jefferson et al. [33], and (d) Steeves et al. [61] with red and blue constituents representing materials with high and low CTE respectively.

lattice with zero thermal expansion while maximizing the bulk modulus. Although the bulk modulus was optimized, the in-plane uniaxial stiffness is lacking. The complicated configuration and geometry of the unit cell by Sigmund and Torquato [58] also limits its application due to difficulty in manufacturing. The lattice by Steeves et al. [61] is relatively simple, stiff, and can be designed to have zero thermal expansion. The net CTE of the lattice is in fact tailorable by altering the geometry and/or materials. Steeves et al. [61] has shown that the biaxial stiffness of the unit cell is near the theoretical limits for bi-material lattices with zero thermal expansion as derived by Gibiansky and Torquato [27].

1.1.2 Properties of Bi-material Lattices

The configuration of the lattice plays an important role in determining its stiffness and strength. Stretching-dominated lattices are favoured over bending-dominated topologies due to significant advantages in stiffness as noted by Deshpande et al. [17]. Both architectures are illustrated and contrasted in Figure 1.3. The bending-dominated structure shown on the left collapses when it is loaded as the struts are free to rotate about the pin-joints. On the other hand, the stretching-dominated structure shown on the right remains intact because the additional strut allows the applied load to be supported through tension and compression in the members. For cellular structures, it has been shown that stiffness is correlated to the relative density, $\bar{\rho}$, which is defined as the density of the material divided by the density of the solid block from which the cell walls are formed [29]. For planar lattices, the stiffness scales linearly with $\bar{\rho}$ for stretching-dominated topologies, while for bending-dominated architectures the stiffness is proportional to $\bar{\rho}^3$

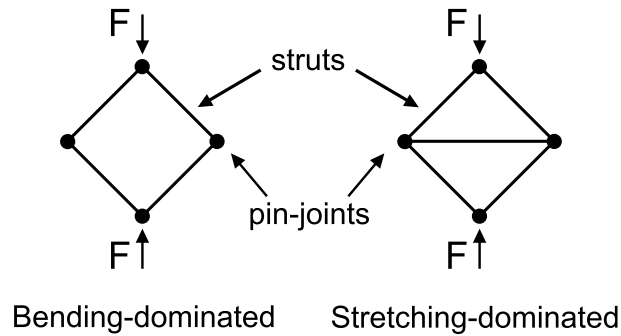


Figure 1.3: Illustration of bending and stretching-dominated architectures adapted from Deshpande et al. [17].

[29]. Typical values of $\bar{\rho}$ will be between 0.1–0.5 for the bi-material lattices of interest [61]. Therefore planar stretching-dominated architectures will be approximately one to two orders of magnitude stiffer than their bending-dominated counterparts.

As elucidated by Steeves et al. [61], a lattice must possess certain characteristics to obtain the properties of low thermal expansion and sufficient rigidity. The key traits are summarized in the following points:

1. The topology should be at minimum three-phase, incorporating empty space with two materials having different CTE. The coefficients of thermal expansion for materials 1 and 2 are identified as α_1 and α_2 respectively, where $\alpha_1 < \alpha_2$.
2. A continuous periodic network of unit cells shaped as skewed polygons is constructed from constituent 1. Contained within the unit cells are unskewed polygons of material type 2. The skewness angle, θ , is an important geometric parameter that represents the deviation of constituent 1 members from a regular polygon.
3. Two types of nodes should exist within the structure: (i) lattice nodes — points at which the unit cells are attached to one another, and (ii) expansion nodes — interface points between the two constituents.
4. The unit cell must be completely triangulated such that the structure is stretching-dominated when mechanically loaded.
5. Length changes of the members should be absorbed through rotations at the nodes. This property is also important to ensure that the lattice has high stiffness and strength.

Examples of unit cells having the above characteristics are illustrated in Figure 1.4. Each is based on a regular polygon and it is observed that the complexity of the lattice increases

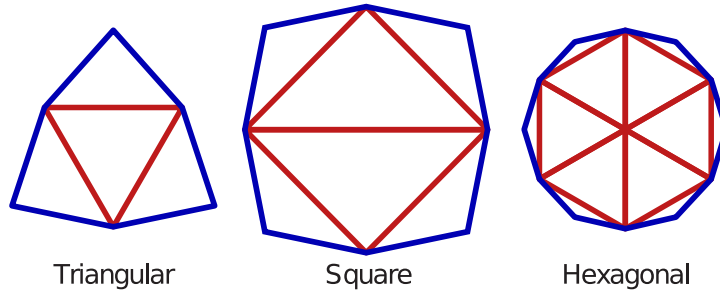


Figure 1.4: Schematic diagram of various polygonal unit cells that are fully triangulated and stretching-dominated, adapted from Steeves et al. [61]. Blue and red members represent materials 1 and 2 having α_1 and α_2 respectively.

with the numbers of edges. It is important to note that in theory, the overall thermal expansion of the lattice is independent of the configuration of constituent 2 members, provided they behave isotropically.

1.2 Motivation and Scope of Research

A bi-material lattice consisting of unit cells approximately 50 mm in length has been designed, fabricated, and validated experimentally to have near zero CTE by Steeves et al. [61, 62]. Their design consists of aluminum (Al) and titanium (Ti) constituents due to the ideal ratio of their CTEs, and serves as a basis for the work conducted in this thesis. The objective of the research presented in this report is to extend the work done by Steeves et al. [61] to the microscale, several orders of magnitude smaller than what has been currently achieved. At such small length scales, a number of important issues arise that need resolving.

This research is performed in collaboration with The Keck Institute for Space Studies (KISS) at the California Institute of Technology (Caltech) and is motivated by the application of low thermal expansion materials in space. More specifically, thermally stable materials are desired in the construction of optical elements in an infrared space telescope. KISS has put forth a technical development program which studies the concept and feasibility of a self-assembling, large space telescope. The primary mirror is a mosaic comprised of smaller segments that are launched on a number of low cost nano-satellites that will autonomously rendezvous and dock. As a part of this case study, thermally stable materials for constructing the mirrors are investigated to maintain the shape of

the optical elements without thermal protection. The concept of bi-material lattices are therefore applied to create an optical surface that has zero thermal expansion.

Due to the empty spaces in the three-phase lattice, the size of the unit cell must be small to avoid optical diffraction. For this particular application, it is desired that the length of a unit cell be on the order of microns. At these length scales, the lattice is manufactured from thin metallic films via electron-beam (e-beam) deposition and photolithography. Special considerations must therefore be made when dealing with microscale materials. During e-beam deposition, metal is evaporated using a beam of electrons and the vapour is deposited onto a substrate. When the atoms contact and settle on the substrate, they do not form a crystalline lattice. Instead, an amorphous structure is formed which has been confirmed by electron backscatter diffraction (EBSD) and x-ray diffraction (XRD) experiments performed by collaborators at Caltech. In an amorphous material, there exists no long range order and atoms do not sit neatly on crystallographic planes. As a result of differing microstructures, the mechanical and thermal properties of the thin metallic films may differ from their bulk crystalline forms.

This research aims to encompass the issues and questions that arise when designing and applying the concepts of low thermal expansion lattices at the microscale. The specific topics included and studied in this thesis are outlined as follows:

1. New features that have been incorporated into the design of the unit cell, known as spacers, are analyzed to determine their effect on the thermal expansion of the lattice. Analytical solutions are derived to obtain an expression for the theoretical CTE of the lattice for both pinned and bonded joint configurations. The theoretical predictions are subsequently verified through finite element (FE) simulations.
2. The thermal expansion of amorphous Al and Ti are undocumented in literature, thus their CTEs are studied and determined via molecular dynamics (MD) simulations. Furthermore, the recrystallization temperatures of amorphous Al and Ti are investigated and the resulting volume changes due to devitrification are quantified.
3. The elastic-plastic properties of Al and Ti films are determined using load-displacement curves obtained from nanoindentation experiments. The Young's modulus and constitutive stress-strain relationship are extracted and confirmed via FE simulations.
4. Microscale lattices having near zero thermal expansion are designed with the aid of information obtained from previous studies. Unit cell configurations are thermally cycled via FE simulations to validate their CTE and ensure stable long term

behaviour.

The exploration and study of the issues above will therefore facilitate the design of thermally stable materials for the application of orbital optics. It is critical for its development to understand the impact of spacers on the thermal expansion of the bi-material lattice, and know the material properties of Al and Ti thin films. This knowledge will allow accurate models and predictions to be made regarding the thermal and mechanical behaviour of the lattice.

1.3 Thesis Organization

The following content in this thesis will be divided into five chapters as follows. In Chapter 2, the CTE of a pinned and bonded joint lattice with spacers is derived. The effect of spacers on the thermal expansion of a bi-material lattice is discussed and the analytical solutions are compared with results from FE simulations. Next, the MD simulations for studying the thermal expansion and recrystallization of amorphous Al and Ti are described in Chapter 3. The methods for analyzing simulation data are presented and the results from the study are interpreted. In Chapter 4, the procedures in which the mechanical properties of Al and Ti thin films are extracted through nanoindentation are given. Elastic-plastic stress-strain relationships obtained from the analyses are discussed and confirmed using FE simulations. Next, unit cell configurations with near zero CTE are presented in Chapter 5. FE simulations are conducted to illustrate the thermal expansion behaviour and to confirm long term stability of the lattice. Lastly, conclusions and recommendations for future studies are given in Chapter 6.

Chapter 2

Analytical and Numerical Study of Spacers

In this chapter, the effect of adding spacers to the lattice by Steeves et al. [61] is analyzed and discussed. First, an overview of the existing unit cell geometry is given in Section 2.1, and the motivation for introducing spacers is explained. The thermal expansion of the new lattice geometry assuming pinned and bonded joints are then derived in Section 2.2. The resulting expressions and change in thermal properties are also discussed. Lastly, FE models are constructed and analyzed to provide a numerical comparison in Section 2.3. Results from theoretical and simulated models are compared and contrasted.

2.1 Low Thermal Expansion Lattices

The bi-material lattice designed by Steeves et al. [61] utilizes unit cells based on an equilateral triangle as illustrated in Figure 2.1. Constituents with low and high CTE are depicted in blue and red respectively. Important geometric parameters of the unit cell have been identified as θ , the skewness angle, ℓ_1 , the length of type 1 members, ℓ_2 , the length of type 2 members, and L , the overall length of the unit cell. For a lattice with a net CTE of zero, the stationary points (nodes that remain fixed during a change in temperature) are labeled as the centres of constituent 2 members and the lattice nodes.

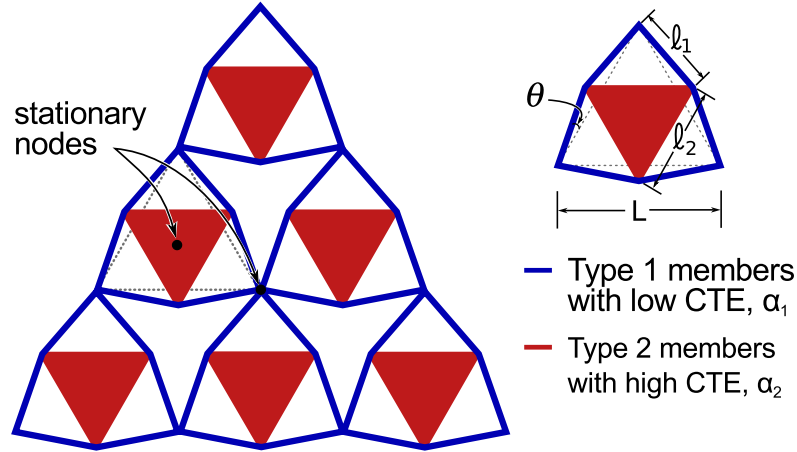


Figure 2.1: Illustration of bi-material lattice based on a triangular unit cell adapted from Steeves et al. [62]. Important geometric parameters of the unit cell are labeled and the stationary nodes for a lattice with a net CTE of zero are identified.

2.1.1 Pinned Joint Lattices

To predict the thermal behaviour of the bi-material lattice, an analytic expression for the net coefficient of thermal expansion, $\bar{\alpha}$, is desired. Considering a unit cell with an original length L , $\bar{\alpha}$ is defined to relate an incremental change in unit cell length, dL , due to an incremental change in temperature, dT . The relationship $dL = \bar{\alpha}LdT$ is therefore obtained. Similarly, the change in length of members 1 and 2 are given by $d\ell_1 = \alpha_1\ell_1dT$ and $d\ell_2 = \alpha_2\ell_2dT$ respectively. Using geometric relations, the normalized net thermal expansion of the lattice has been derived by Steeves et al. [61] for a pinned joint lattice (where members are allowed to rotate freely at the joints with no internal stress buildup) as follows:

$$\frac{\bar{\alpha}}{\alpha_1} = \frac{1 - \frac{1}{2} \left(\frac{\alpha_2}{\alpha_1} \right) \sin(2\theta) \left(\frac{1}{\sqrt{3}} + \tan\theta \right)}{1 - \frac{1}{2} \sin(2\theta) \left(\frac{1}{\sqrt{3}} + \tan\theta \right)} \quad (2.1)$$

From Equation 2.1, it is evident that the only parameters affecting the net thermal expansion of the lattice are the ratio of material CTEs, $\Sigma = \alpha_2/\alpha_1$, and the skewness angle, θ . It is important to note that the thermal expansion of the lattice is independent of the length of the unit cell. The lattice can therefore be scaled while maintaining its thermal properties, and Equation 2.1 is applicable to lattices fabricated at the microscale.

By selecting appropriate values of Σ and θ , it is possible to tailor the net thermal expansion of the lattice as desired to meet the needs of specific applications. Isolines of Equation 2.1 are plotted in Figure 2.2 for various values of $\bar{\alpha}/\alpha_1$, including zero. This

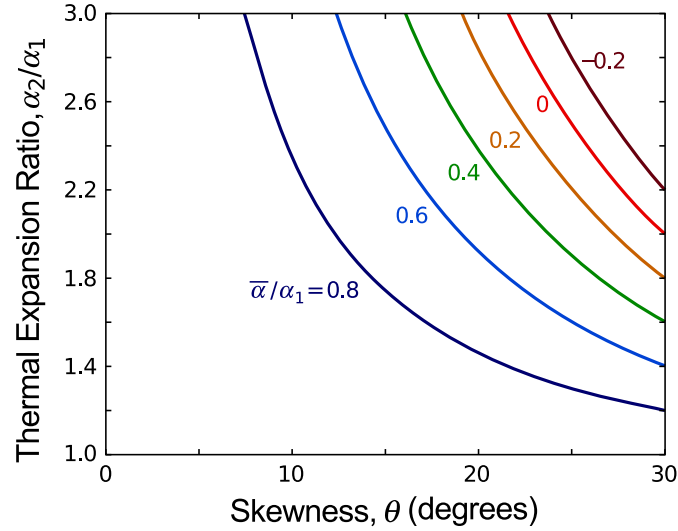


Figure 2.2: Contour plot of $\bar{\alpha}/\alpha_1$ in the design space of θ and $\Sigma = \alpha_2/\alpha_1$ obtained using Equation 2.1, adapted from Steeves et al. [62]

plot illustrates the required combination of Σ and θ to produce a lattice with the desired net CTE. As a general rule, increasing θ or Σ will lower thermal expansion of the lattice. Note that the upper limit on skewness for the triangular unit cell configuration is 30° , which in reality is unfeasible since type 1 members from adjacent unit cells would become overlapped. Without the void regions in between unit cells, the low thermal expansion property of the lattice is lost. It should also be noted that $\bar{\alpha}$ is not necessarily limited to be positive, but can take on negative values given the appropriate combinations of materials and skewness. To construct a lattice with zero thermal expansion, materials with disparate CTEs must be used, giving values of Σ greater than 2, along with relatively large angles of skewness. It has been noted by Steeves et al. [61] that for Al and Ti, $\Sigma \approx 2.5$ and thus a zero CTE bi-material lattice would exist when $\theta \approx 25^\circ$.

2.1.2 Bonded Joint Lattices

Equation 2.1 from the previous section gives the theoretical expression for a pinned joint lattice where the members are allowed to rotate freely with no internal stresses. In practice, the joints will be bonded rather than pinned due to simplicity in manufacturing. A bonded joint can carry moments and resist rotation, creating internal stresses and strains which therefore affect the thermal properties of the lattice. The normalized net

CTE for a bonded joint lattice has been derived by Steeves et al. [61] and is given by:

$$\frac{\bar{\alpha}}{\alpha_1} = 1 - \frac{(C_1 \tan \theta - 12\sqrt{3}) (\cos \theta + \sqrt{3} \sin \theta) \left(\frac{\alpha_2}{\alpha_1} - 1\right)}{C_1 (\sqrt{3} \cos \theta - \sin \theta) + 12 \left(\sqrt{3} + 2\frac{E_1 A_1}{E_2 A_2}\right) (\cos \theta + \sqrt{3} \sin \theta)} \quad (2.2)$$

E_1 , E_2 and A_1 , A_2 are the Young's moduli of elasticity and cross-sectional areas of their respective constituents, and $C_1 = A_1 \ell_1^2 / I_1$ where $I_1 = A_1 r_1^2$. I_1 represents the second moment of inertia of type 1 members having a radius of gyration r_1 . Equation 2.2 reveals that the thermal expansion of a bonded joint lattice is dependent on the mechanical properties and sizes of the members. Defining r_1/L to be the slenderness ratio of type 1 members, it can be shown that as $r_1/L \rightarrow 0$, Equation 2.2 reduces to Equation 2.1. That is, as constituent 1 members become more slender, the thermal expansion behaviour of a bonded joint lattice approaches that of a pinned joint lattice. To illustrate this effect, the normalized net CTE of a bonded joint lattice is plotted as a function of θ for increasing values of r_1/L in Figure 2.3 while assuming $E_1 A_1 / E_2 A_2 = 1$ and $\alpha_2 / \alpha_1 = 2.5$. The curve where $r_1/L = 0$ represents the properties of a pinned joint lattice. It is evident from Figure 2.3 that bonding the joints of a lattice will effectively increase the net thermal expansion of the structure. To retain the same value of $\bar{\alpha} / \alpha_1$ without changing the constituents, θ must be increased. The additional skewness required to compensate for the bonded joints depends on the slenderness ratio of type 1 members. A slight increase is observed when $r_1/L = 0.02$, however it grows considerably when $r_1/L = 0.04$.

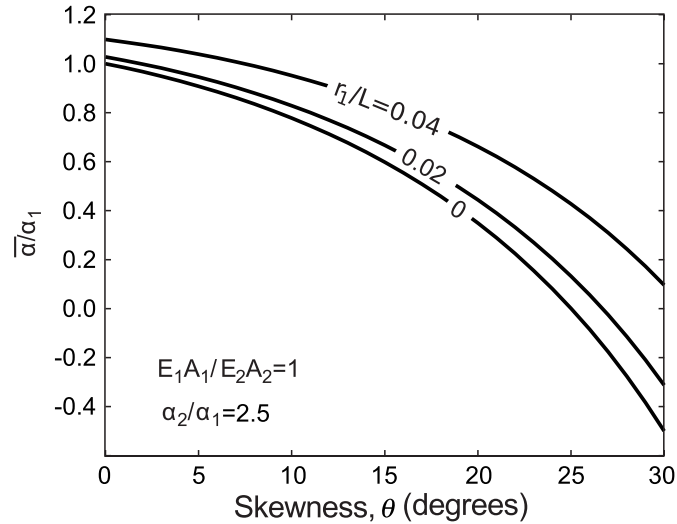


Figure 2.3: Normalized net CTE of a bonded joint lattice plotted as a function of θ for different values of r_1/L (using Equation 2.2), adapted from Steeves et al. [61]

The theoretical thermal expansion of a bonded joint lattice can also be obtained from the work by Berger et al. [5]. In their study, they derive an expression which predicts the CTE of a bonded joint lattice while considering the reduced effective lengths of the members given flanges at the nodes. By assuming the absence of flanges, the final result derived by Berger et al. [5] can be simplified to give the following:

$$\frac{\bar{\alpha}}{\alpha_1} = \frac{\sqrt{3} - \frac{\alpha_2}{\alpha_1} \sin \theta (\cos \theta + \sqrt{3} \sin \theta)}{\sqrt{3} - \sin \theta (\cos \theta + \sqrt{3} \sin \theta)} \quad (2.3)$$

$$+ \frac{12I_1 (\cos \theta + \sqrt{3} \sin \theta) \left[\sqrt{3} \cos \theta + \left(3 + \frac{2E_1 A_1 \ell_2}{E_2 A_2 \ell_1} \right) \sin \theta \right] \left(\frac{\alpha_2}{\alpha_1} - 1 \right)}{A_1 \ell_1^2 (\sqrt{3} \cos \theta - \sin \theta) \cos \theta \left\{ (\sqrt{3} \cos \theta - \sin \theta)^2 + \frac{12I_1}{A_1 \ell_1^2} \left[\frac{2E_1 A_1 \ell_2}{E_2 A_2 \ell_1} + (\cos \theta + \sqrt{3} \sin \theta)^2 \right] \right\}}$$

where E_i and A_i are the Young's modulus and cross-sectional area of constituent i , and I_1 is the second moment of inertia of type 1 members. Similar to Equation 2.2, the expression by Berger et al. [5] is dependent on the mechanical properties and sizes of the members. By plotting Equations 2.2 and 2.3, it is found that they are not equivalent, however they produce similar curves.

2.1.3 New Lattice Geometry

As an improvement to the design by Steeves et al. [61], features hereby denoted as spacers are incorporated into the unit cell geometry as proposed by Berger et al. [5]. Spacers appear at the lattice nodes and provides separation between adjacent unit cells. The new unit cell geometry and resulting lattice after the addition of spacers is illustrated in Figure 2.4. As before, the red and blue members represent constituents with high and low

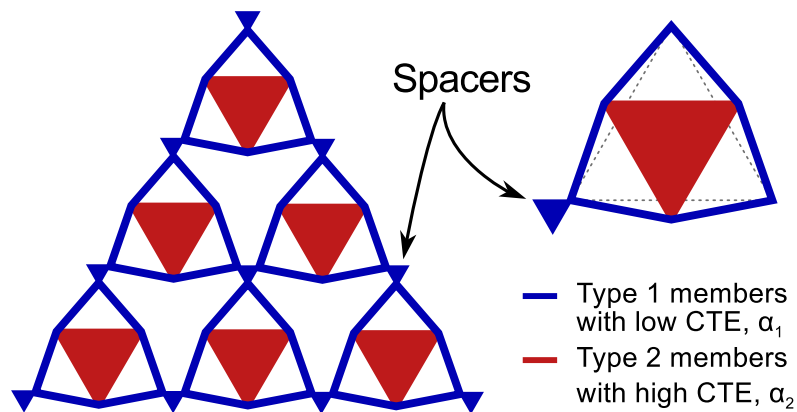
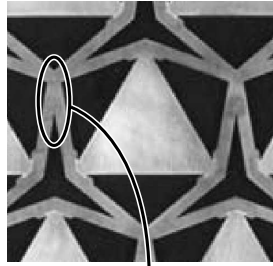


Figure 2.4: Concept of unit cell with a spacer is depicted on the right with the resulting lattice structure illustrated on the left.

CTE respectively. Spacers are depicted as triangles in Figure 2.4 for simplicity and are constructed from the same material as constituent 1 members for ease of manufacturing. As it turns out, spacers having a low CTE are desirable to minimize their impact on the overall thermal expansion of the structure. The motivation for incorporating spacers into the lattice is to circumvent the overlapping of constituent 1 members near the points where unit cells connect. Due to their non-zero thickness, type 1 members from adjacent unit cells intersect with one another to create non-ideal lattice nodes. This phenomenon is clearly illustrated in Figure 2.5 and is increasingly evident for unit cell configurations with large skewness angles. Overlapped members will augment the rotational resistance at the lattice nodes and effectively decrease the length of type 1 members, thereby increasing their slenderness ratio r_1/L . As elucidated by Steeves et al. [61] and discussed in the previous section, bonded joints will increase the net CTE of the lattice but are effectively pinned joints if r_1/L is small. Non-ideal nodes therefore increase the overall CTE of the structure and are undesirable. By introducing additional material at the lattice nodes in between unit cells, the intersection of constituent 1 members can be prevented and thus non-ideal nodes are alleviated. Another advantage of the addition of spacers is that larger skewness angles are now attainable. For the old geometry, $\theta = 30^\circ$ is an infeasible upper limit where type 1 members are completely overlapped. With the introduction of spacers, skewness angles of 30° and above are now achievable.

An analytical solution for the thermal expansion of lattices with spacers has been



Overlapped
members

Figure 2.5: Lattice by Steeves et al. [62] with a skewness angle of 20° using Ti and Al alloys for type 1 and 2 constituents respectively. An area in which Ti members are overlapped is highlighted to illustrate the consequence of a non-ideal lattice node.

derived by Berger et al. [5] to be:

$$\frac{\bar{\alpha}}{\alpha_1} = \frac{\sqrt{3} - \frac{\alpha_2}{\alpha_1} (\cos \theta + \sqrt{3} \sin \theta) \sin \theta}{\sqrt{3} - (\cos \theta + \sqrt{3} \sin \theta) \sin \theta} \frac{L}{L+H} + \frac{H}{L+H} \quad (2.4)$$

where L and H are the sizes of the original unit cell configuration and spacer respectively. Equation 2.4 is formulated under the assumption that the bending resistance of the members is negligible, and is therefore representative of a pinned joint lattice.

2.2 Analytical Study

In this section, the theoretical thermal expansion of a lattice with spacers is derived from first principles for completeness. Two solutions are obtained under the assumption of (i) pinned joints, and (ii) bonded joints. The resulting analytical solutions are then examined and discussed.

2.2.1 Thermal Expansion of New Geometry Assuming Pinned Joints

Derivation

The introduction of a new feature adds another variable in defining the configuration and geometry of the unit cell. Thus, it is desirable to derive a new analytical expression for predicting the thermal expansion of the new geometry. The new formulation will have the old geometric variables, as well as a new parameter which defines the size of the spacer. To determine the new expression, the procedure from the original derivation by Steeves et al. [61] is followed with some additional considerations made for the spacer. In this derivation, it is assumed that the joints of the lattice are pin connected.

Consider the unit cell shown in Figure 2.6 which serves as a basis for this analysis. The spacer is assumed to be an equilateral triangular for simplicity, with ℓ_3 denoting the length of its side. L denotes the size of the new unit cell, which includes the length of the old unit cell plus the spacer. Parameters ℓ_1 and ℓ_2 denote the length of type 1 and 2 members respectively as before. With the introduction of spacers, the net thermal expansion of the lattice will now also depend on ℓ_3 . From geometric relations,

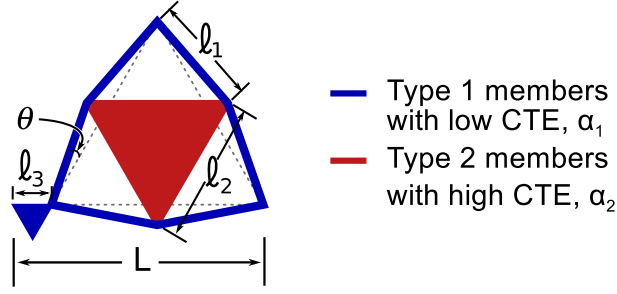


Figure 2.6: Unit cell with spacer. All parameters defining unit cell geometry are labeled.

the following expressions can be written:

$$\ell_1 = \frac{L - \ell_3}{2 \cos \theta} \quad (2.5)$$

$$\ell_2 = 2\ell_1 \sin(30^\circ + \theta) \quad (2.6)$$

The trigonometric identity $\sin(\alpha + \beta) = \sin \alpha \cos \beta + \sin \beta \cos \alpha$ is used to expand $\sin(30^\circ + \theta)$ and ℓ_1 is substituted into ℓ_2 to give:

$$\begin{aligned} \ell_2 &= \frac{L - \ell_3}{\cos \theta} (\sin 30^\circ \cos \theta + \sin \theta \cos 30^\circ) \\ &= \frac{L - \ell_3}{2} (1 + \sqrt{3} \tan \theta) \end{aligned} \quad (2.7)$$

Differentiating Equations 2.5 and 2.7 produces:

$$d\ell_1 = \frac{\ell_1}{L - \ell_3} (dL - d\ell_3) + \frac{(L - \ell_3) \sin \theta}{2 \cos^2 \theta} d\theta \quad (2.8)$$

$$d\ell_2 = \frac{\ell_2}{L - \ell_3} (dL - d\ell_3) + \frac{\sqrt{3} (L - \ell_3)}{2 \cos^2 \theta} d\theta \quad (2.9)$$

Equation 2.9 is rearranged to isolate $d\theta$:

$$d\theta = \left[d\ell_2 - \frac{\ell_2}{L - \ell_3} (dL - d\ell_3) \right] \frac{2 \cos^2 \theta}{\sqrt{3} (L - \ell_3)} \quad (2.10)$$

The expression for $d\theta$ is then substituted back into Equation 2.8 to give the following:

$$d\ell_1 = \frac{\ell_1}{L - \ell_3} (dL - d\ell_3) + \frac{\sin \theta}{\sqrt{3}} \left[d\ell_2 - \frac{\ell_2}{L - \ell_3} (dL - d\ell_3) \right] \quad (2.11)$$

For a temperature change dT , the change in member lengths in a pinned joint lattice result purely from thermal expansion effects and are given by:

$$d\ell_1 = \ell_1 \alpha_1 dT \quad (2.12)$$

$$d\ell_2 = \ell_2 \alpha_2 dT \quad (2.13)$$

$$d\ell_3 = \ell_3 \alpha_1 dT \quad (2.14)$$

The overall expansion of the unit cell is then defined as:

$$dL \equiv L\bar{\alpha}dT \quad (2.15)$$

Equations 2.12 to 2.15 are substituted back into Equation 2.11 to obtain:

$$\ell_1\alpha_1dT = \frac{\ell_1}{L-\ell_3}(L\bar{\alpha}dT - \ell_3\alpha_1dT) + \frac{\sin\theta}{\sqrt{3}} \left[\ell_2\alpha_2dT - \frac{\ell_2}{L-\ell_3}(L\bar{\alpha}dT - \ell_3\alpha_1dT) \right]$$

Each term is multiplied by dT , therefore this factor drops out. After canceling and grouping like terms, the expression above becomes:

$$\bar{\alpha} \left(\frac{\sin\theta}{\sqrt{3}} \frac{\ell_2L}{L-\ell_3} - \frac{\ell_1L}{L-\ell_3} \right) = \alpha_1 \left(\frac{\sin\theta}{\sqrt{3}} \frac{\ell_2\ell_3}{L-\ell_3} - \frac{\ell_1\ell_3}{L-\ell_3} - \ell_1 \right) + \alpha_2 \frac{\sin\theta\ell_2}{\sqrt{3}} \quad (2.16)$$

Substituting Equation 2.6 into Equation 2.16 and manipulating gives:

$$\bar{\alpha} \left(\frac{1}{1-\frac{\ell_3}{L}} \right) \left(\frac{\sin\theta\cos\theta}{\sqrt{3}} + \sin^2\theta - 1 \right) = \alpha_1 \left(\frac{1}{\frac{L}{\ell_3}-1} \right) \left(\frac{\sin\theta\cos\theta}{\sqrt{3}} + \sin^2\theta - \frac{L}{\ell_3} \right) + \alpha_2 \left(\frac{\sin\theta\cos\theta}{\sqrt{3}} + \sin^2\theta \right)$$

Solving for $\bar{\alpha}$ therefore results in:

$$\bar{\alpha} = \frac{\alpha_1 \left(\frac{\ell_3}{L} \right) \left(\frac{\sin\theta\cos\theta}{\sqrt{3}} + \sin^2\theta - \frac{L}{\ell_3} \right) + \alpha_2 \left(1 - \frac{\ell_3}{L} \right) \left(\frac{\sin\theta\cos\theta}{\sqrt{3}} + \sin^2\theta \right)}{\frac{\sin\theta\cos\theta}{\sqrt{3}} + \sin^2\theta - 1}$$

Finally, using the trigonometric identity $\sin 2\theta = 2\sin\theta\cos\theta$ and normalizing $\bar{\alpha}$ with respect to α_1 , the end result becomes:

$$\frac{\bar{\alpha}}{\alpha_1} = \frac{1 - \frac{\alpha_2}{\alpha_1} \left(\frac{1}{2} \sin(2\theta) \right) \left(\frac{1}{\sqrt{3}} + \tan\theta \right) + \left(\frac{\ell_3}{L} \right) \left(\frac{\alpha_2}{\alpha_1} - 1 \right) \left(\frac{1}{2} \sin(2\theta) \right) \left(\frac{1}{\sqrt{3}} + \tan\theta \right)}{1 - \frac{1}{2} \sin(2\theta) \left(\frac{1}{\sqrt{3}} + \tan\theta \right)} \quad (2.17)$$

Thus, Equation 2.17 gives the theoretical normalized thermal expansion of a pinned joint lattice with spacers. It can be shown that the result derived here is equivalent to Equation 2.4, the expression given by Berger et al. [5].

Thermal Properties

The final expression obtained in the derivation above can be re-written in the following form:

$$\frac{\bar{\alpha}}{\alpha_1} = \left(\frac{\bar{\alpha}}{\alpha_1} \right)_0 + \frac{\left(\frac{\ell_3}{L} \right) \left(\frac{\alpha_2}{\alpha_1} - 1 \right) \left(\frac{1}{2} \sin(2\theta) \right) \left(\frac{1}{\sqrt{3}} + \tan\theta \right)}{1 - \left(\frac{1}{2} \sin(2\theta) \right) \left(\frac{1}{\sqrt{3}} + \tan\theta \right)} \quad (2.18)$$

where

$$\left(\frac{\bar{\alpha}}{\alpha_1}\right)_0 = \frac{1 - \left(\frac{\alpha_2}{\alpha_1}\right) \left(\frac{1}{2} \sin(2\theta)\right) \left(\frac{1}{\sqrt{3}} + \tan \theta\right)}{1 - \left(\frac{1}{2} \sin(2\theta)\right) \left(\frac{1}{\sqrt{3}} + \tan \theta\right)}$$

$(\bar{\alpha}/\alpha_1)_0$ is equivalent to Equation 2.1 which gives the normalized net CTE of a pinned joint lattice without spacers as derived by Steeves et al. [61]. In Equation 2.18, the parameter ℓ_3/L is the new variable that influences the thermal expansion of the new geometry. This ratio represents the length of the spacer relative to the total length of the unit cell and is therefore between 0 and 1. When $\ell_3/L = 0$, scenario where no spacers are present, Equation 2.18 simplifies to Equation 2.1 as expected. At the other extreme, $\ell_3/L = 1$ is the case where the length of the spacer makes up the entire length of the unit cell, or when the original lattice is no longer present. It can be shown that when $\ell_3/L = 1$, $\bar{\alpha}/\alpha_1$ equals unity. In this case, the net thermal expansion of the lattice simply takes on the CTE of constituent 1, the material from which the spacers are fabricated. Note that since ℓ_3/L is dimensionless, the thermal properties of the lattice are still independent of unit cell length and is scalable to the application of microscale lattices.

The second term in Equation 2.18 is positive for skewness angles of interest since α_2/α_1 is defined to be greater than 1. It can therefore be concluded that the addition of spacers will increase the net CTE of the lattice. This result is intuitively apparent since extra material with uncontrolled thermal expansion is incorporated into the structure. The increase in thermal expansion is quantified and illustrated in Figure 2.7, which uses Equation 2.18 to plot $\bar{\alpha}/\alpha_1$ as a function of ℓ_3/L for different values of θ assuming

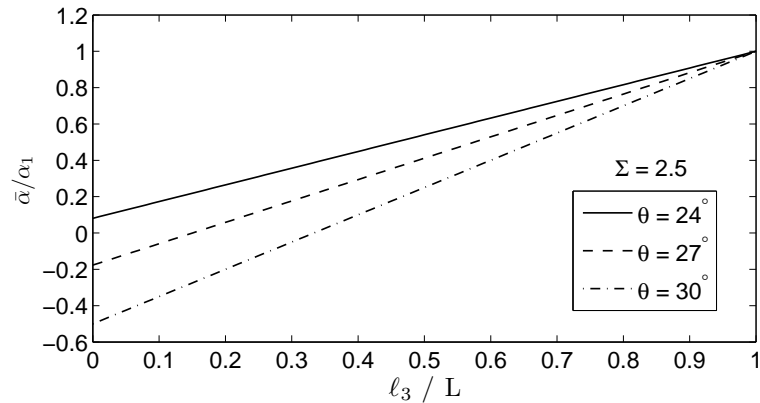


Figure 2.7: Theoretical effect of ℓ_3/L on $\bar{\alpha}/\alpha_1$ for $\theta = 24^\circ$, 27° , and 30° assuming $\alpha_2/\alpha_1 = 2.5$ (representative of an Al/Ti lattice).

$\Sigma = 2.5$. From this graph it is apparent that the change in $\bar{\alpha}/\alpha_1$ as a result of adding spacers will depend on the skewness angle of the configuration; the net CTE of lattices with large θ experience a greater increase in CTE for a given an increment in ℓ_3/L . This is because lattices with larger θ have lower net thermal expansion, but $\bar{\alpha}/\alpha_1$ approaches a value of 1 in all scenarios as $\ell_3/L \rightarrow 1$. Although spacers result in an increased net CTE, the elimination of non-ideal lattice nodes and facilitation of larger skewness angles is of greater advantage. In reality, spacers do not need to be large to serve their function. ℓ_3/L will typically be 0.1 or smaller, accounting for less than 10% of the unit cell length. For $\ell_3/L = 0.1$, the increase in $\bar{\alpha}$ due to the introduction of spacers is minimal, being roughly 10% of α_1 which for Ti equates to approximately 1 ppm/K.

Equation 2.17 can also be used to determine the appropriate geometric and material properties of a lattice to give a net thermal expansion of zero. By setting the left-hand side of the expression to be zero, the numerator of the right side is thus equated to zero to obtain:

$$\frac{\alpha_2}{\alpha_1} = \frac{1 - \frac{\ell_3}{L} \left(\frac{1}{2} \sin(2\theta) \right) \left(\frac{1}{\sqrt{3}} + \tan \theta \right)}{\left(1 - \frac{\ell_3}{L} \right) \left(\frac{1}{2} \sin(2\theta) \right) \left(\frac{1}{\sqrt{3}} + \tan \theta \right)} \quad (2.19)$$

The combinations of Σ and θ to produce a lattice with zero thermal expansion are thus plotted using Equation 2.19 in Figure 2.8 for different spacer sizes. To reiterate, the curve corresponding to $\ell_3/L = 0$ (solid line) represents a lattice without spacers and is used as a baseline for comparison. As already noted, spacers increase the net CTE of a lattice, thus θ or Σ (or a combination of both) must be enlarged to compensate for the positive change in CTE. It is typically easier to adjust the skewness angle of a lattice rather than reselect materials to give the desired Σ . Figure 2.8 shows that when $\ell_3/L = 0.1$, an

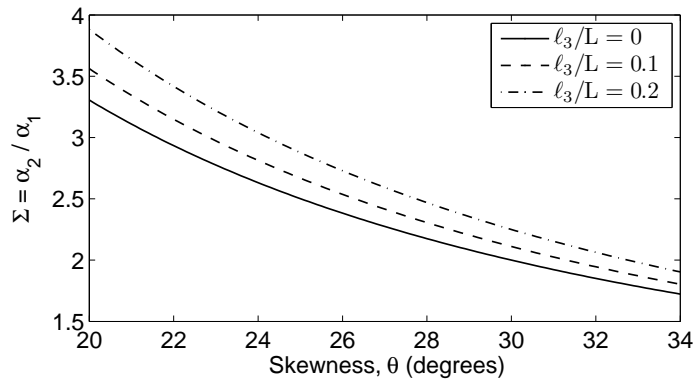


Figure 2.8: Required Σ and θ to give $\bar{\alpha} = 0$ for different values of ℓ_3/L from Equation 2.19.

additional skewness of approximately 1° is required to keep $\bar{\alpha} = 0$. The slight increment in CTE introduced by the spacers can therefore be easily accounted for through minimal adjustments of the geometry. Thus, the benefits of relieving overlapped members and allowing larger skewness outweigh the downsides of incorporating spacers into the unit cell geometry.

2.2.2 Thermal Expansion of New Geometry Assuming Bonded Joints

Derivation

In practice, the joints of the lattice will be bonded for simplicity in manufacturing. The rotational resistance at the joints and inherent stiffness of the members will thus affect the thermal properties of the unit cell. It is therefore desirable to derive an expression for the CTE of the new geometry under the assumption that the joints are bonded.

To begin the derivation, the original unit cell configuration with length L^* is first analyzed since the spacers do not affect its thermal expansion. By taking advantage of symmetry, only one sixth of the structure is considered as shown in Figure 2.9. The interaction between the two members illustrated in this figure, under the appropriate boundary conditions, is sufficient to describe the overall behaviour of the unit cell. Due to symmetry, there can be no rotations at nodes 1, 2, and 3, and the displacements of these nodes are required to move along the symmetric boundaries. From these constraints, there exists only 4 active degrees of freedom: d_{1y} , d_{2y} , d_{3x} , and d_{3y} . To determine the

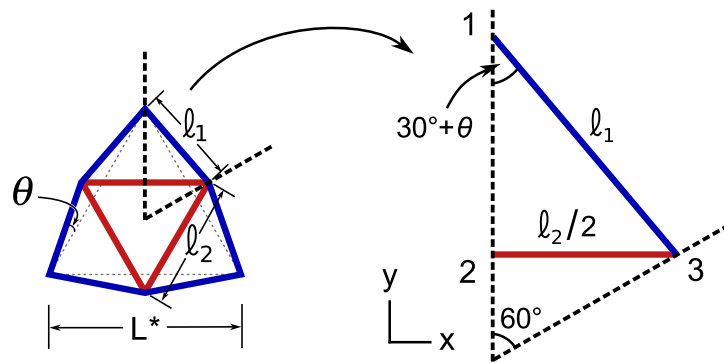


Figure 2.9: One sixth of unit cell under consideration for deriving the thermal expansion of a bonded joint lattice. Dashed lines indicate symmetric boundaries. Type 1 and 2 members are illustrated in blue and red respectively.

net thermal expansion of the unit cell, the stiffness matrix of the structure is constructed and thus an analytical solution for the vertical displacement of node 1 for a given change in temperature is obtained.

In this analysis, frame and truss elements are used to model type 1 and 2 members respectively. Figure 2.10 (a) illustrates the degrees of freedom for a frame element of length L and arbitrary rotation θ . The nodal displacements and forces for a general frame element in global coordinates are related by the following expression:

$$\begin{bmatrix} f_{1x} & f_{1y} & m_1 & f_{2x} & f_{2y} & m_2 \end{bmatrix}^T = k_{\text{frame}} \begin{bmatrix} d_{1x} & d_{1y} & \phi_1 & d_{2x} & d_{2y} & \phi_2 \end{bmatrix}^T$$

where k_{frame} is the stiffness matrix of the frame element and has the form:

$$k_{\text{frame}} = \begin{bmatrix} k_1 c^2 + 12k_2 s^2 & (k_1 - 12k_2)cs & -6k_2 Ls & -k_1 c^2 - 12k_2 s^2 & (12k_2 - k_1)cs & -6k_2 Ls \\ & k_1 s^2 + 12k_2 c^2 & 6k_2 Lc & (12k_2 - k_1)cs & -k_1 s^2 - 12k_2 c^2 & 6k_2 Lc \\ & & 4k_2 L^2 & 6k_2 Ls & -6k_2 Lc & 2k_2 L^2 \\ & & & k_1 c^2 + 12k_2 s^2 & (k_1 - 12k_2)cs & 6k_2 Ls \\ & & & & k_1 s^2 + 12k_2 c^2 & -6k_2 Lc \\ \text{symm} & & & & & 4k_2 L^2 \end{bmatrix}$$

In the stiffness matrix above, $k_1 = EA/L$, $k_2 = EI/L^3$, $c = \cos \theta$, and $s = \sin \theta$. The terms A , E , and I in k_1 and k_2 represent the cross-sectional area, Young's modulus, and second moment of area of the frame element. The nodal forces and displacements for a simple 1-D truss element as illustrated in Figure 2.10 (b) are correlated via k_{truss} , the stiffness matrix of a truss element, through the relation:

$$\begin{bmatrix} f_{1x} \\ f_{2x} \end{bmatrix} = \underbrace{\frac{EA}{L} \begin{bmatrix} 1 & -1 \\ -1 & 1 \end{bmatrix}}_{k_{\text{truss}}} \begin{bmatrix} d_{1x} \\ d_{2x} \end{bmatrix}$$

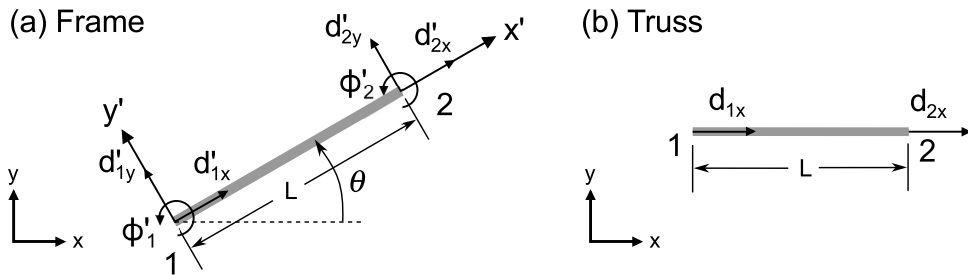


Figure 2.10: Schematic diagram of (a) a frame element of length L and arbitrary rotation θ (x' and y' represent local coordinates), and (b) a 1-D truss element.

where A and E are the cross-sectional area and Young's modulus of the truss element.

From k_{frame} and k_{truss} , the reduced stiffness matrices of members 1 and 2 are defined to be $k_{\textcircled{1}}$ and $k_{\textcircled{2}}$ respectively and are formulated as follows:

$$\begin{bmatrix} f_{1y} \\ f_{3x} \\ f_{3y} \end{bmatrix} = \underbrace{\begin{bmatrix} k_{11}c^2 + 12k_{12}s^2 & (k_{11} - 12k_{12})cs & -k_{11}c^2 - 12k_{12}s^2 \\ & k_{11}s^2 + 12k_{12}c^2 & (12k_{12} - k_{11})cs \\ \text{symm} & & k_{11}c^2 + 12k_{12}s^2 \end{bmatrix}}_{k_{\textcircled{1}}} \begin{bmatrix} d_{1y} \\ d_{3x} \\ d_{3y} \end{bmatrix} \quad (2.20)$$

$$f_{3x} = \underbrace{k_{21}}_{k_{\textcircled{2}}} d_{3x} \quad (2.21)$$

where $k_{11} = E_1 A_1 / \ell_1$, $k_{12} = E_1 I_1 / \ell_1^3$, $k_{21} = 2E_2 A_2 / \ell_2$, $c = \cos(30^\circ + \theta)$, and $s = \sin(30^\circ + \theta)$. The subscripts on E , A , and I indicate the constituent to which the mechanical property belongs. Taking $k_{\textcircled{1}}$ and $k_{\textcircled{2}}$ from Equations 2.20 and 2.21, the global stiffness matrix of the unit cell, κ , is constructed:

$$\begin{bmatrix} f_{1y} \\ f_{3x} \\ f_{3y} \end{bmatrix} = \underbrace{\begin{bmatrix} k_{11}c^2 + 12k_{12}s^2 & (k_{11} - 12k_{12})cs & -k_{11}c^2 - 12k_{12}s^2 \\ & k_{21} + k_{11}s^2 + 12k_{12}c^2 & (12k_{12} - k_{11})cs \\ \text{symm} & & k_{11}c^2 + 12k_{12}s^2 \end{bmatrix}}_{\kappa} \begin{bmatrix} d_{1y} \\ d_{3x} \\ d_{3y} \end{bmatrix} \quad (2.22)$$

To find the displacement of the nodes as a result of thermal expansion, forces are applied to the members to emulate changes in ℓ_1 and ℓ_2 that arise from an increment in temperature. Using the global stiffness matrix of the structure, an analytic solution for d_{1y} is formulated and subsequently used to give an expression for the net CTE of the unit cell. To determine the forces equivalent to the effect of thermal expansion, mechanical strain (ϵ) and thermal strain (ϵ^T) definitions are equated to one another to give:

$$\begin{aligned} \epsilon &= \epsilon^T \\ \frac{\sigma}{E} &= \alpha dT \\ F &= EA\alpha dT \end{aligned}$$

Summing and resolving the forces at the nodes give:

$$f_{1y} = E_1 A_1 \alpha_1 dT \cos(30^\circ + \theta) \quad (2.23)$$

$$f_{3x} = E_1 A_1 \alpha_1 dT \sin(30^\circ + \theta) + E_2 A_2 \alpha_2 dT \quad (2.24)$$

$$f_{3y} = -E_1 A_1 \alpha_1 dT \cos(30^\circ + \theta) \quad (2.25)$$

Substituting Equations 2.23–2.2.2 into Equation 2.22 results in the following:

$$\begin{bmatrix} E_1 A_1 \alpha_1 dTc \\ E_1 A_1 \alpha_1 dTs + E_2 A_2 \alpha_2 dT \\ -E_1 A_1 \alpha_1 dTc \end{bmatrix} = \begin{bmatrix} k_{11}c^2 + 12k_{12}s^2 & (k_{11} - 12k_{12})cs & -k_{11}c^2 - 12k_{12}s^2 \\ & k_{21} + k_{11}s^2 + 12k_{12}c^2 & (12k_{12} - k_{11})cs \\ \text{symm} & & k_{11}c^2 + 12k_{12}s^2 \end{bmatrix} \begin{bmatrix} d_{1y} \\ d_{3x} \\ d_{3y} \end{bmatrix}$$

The above system can be reduced to 2 equations by noting that $d_{3x} = \sqrt{3}d_{3y}$, and that the third row is equivalent to the first:

$$\begin{bmatrix} E_1 A_1 \alpha_1 dTc \\ E_1 A_1 \alpha_1 dTs + E_2 A_2 \alpha_2 dT \end{bmatrix} = \begin{bmatrix} k_{11}c^2 + 12k_{12}s^2 & \sqrt{3}(k_{11} - 12k_{12})cs - k_{11}c^2 - 12k_{12}s^2 \\ (k_{11} - 12k_{12})cs & \sqrt{3}(k_{21} + k_{11}s^2 + 12k_{12}c^2) + (12k_{12} - k_{11})cs \end{bmatrix} \begin{bmatrix} d_{1y} \\ d_{3y} \end{bmatrix} \quad (2.26)$$

Solving Equation 2.26 for d_{1y} gives the following expression after some manipulation:

$$d_{1y} = \frac{E_1 A_1 \alpha_1 [\sqrt{3}ck_{21} + 12k_{12}(\sqrt{3}c + s)] - E_2 A_2 \alpha_2 [k_{11}c(\sqrt{3}s - c) - 12k_{12}s(\sqrt{3}c + s)]}{\sqrt{3}(k_{11}k_{21}c^2 + 12k_{12}k_{21}s^2 + 12k_{11}k_{12})} dT \quad (2.27)$$

From the geometry of the unit cell, the lengths of the members can be written as:

$$\ell_1 = \frac{L^*}{2 \cos \theta} \quad , \quad \ell_2 = \frac{L^*}{\cos \theta} \sin(30^\circ + \theta)$$

Thus, k_{11} , k_{12} , and k_{21} can be expressed in the following form:

$$k_{11} = \frac{2 \cos \theta E_1 A_1}{L^*} \quad (2.28)$$

$$k_{12} = \frac{2 \cos \theta E_1 A_1}{L^* C_1} \quad (2.29)$$

$$k_{21} = \frac{2 \cos \theta E_2 A_2}{L^* s} \quad (2.30)$$

where $C_1 = A_1 \ell_1^2 / I_1$. Equations 2.28–2.30 are substituted back into Equation 2.27 to obtain the following expression:

$$d_{1y} = \frac{\alpha_1 \left[\sqrt{3}C_1c + 12 \frac{E_1 A_1}{E_2 A_2} s(\sqrt{3}c + s) \right] - \alpha_2 \left[C_1s(\sqrt{3}s - c) - 12s^2(\sqrt{3}c + s) \right] \frac{L^* dT}{2 \cos \theta}}{\sqrt{3} \left(C_1c^2 + 12s^2 + 12s \frac{E_1 A_1}{E_2 A_2} \right)} \quad (2.31)$$

From the geometry of the unit cell the net CTE, $\bar{\alpha}^*$, is given by:

$$\begin{aligned} \bar{\alpha}^* &= \frac{1}{L^*} \frac{dL^*}{dT} \\ &= \frac{1}{L^*} \frac{\sqrt{3}d_{1y}}{dT} \end{aligned} \quad (2.32)$$

Thus, combining Equations 2.31 and 2.32 and normalizing $\bar{\alpha}^*$ with respect to α_1 gives:

$$\frac{\bar{\alpha}^*}{\alpha_1} = \frac{\left[\sqrt{3}C_1c + 12 \frac{E_1 A_1}{E_2 A_2} s(\sqrt{3}c + s) \right] - \frac{\alpha_2}{\alpha_1} \left[C_1s(\sqrt{3}s - c) - 12s^2(\sqrt{3}c + s) \right] \frac{1}{2 \cos \theta}}{C_1c^2 + 12s^2 + 12s \frac{E_1 A_1}{E_2 A_2}} \quad (2.33)$$

Using the following trigonometric identities:

$$\cos(30^\circ + \theta) = \frac{\sqrt{3} \cos \theta}{2} - \frac{\sin \theta}{2}, \quad \sin(30^\circ + \theta) = \frac{\cos \theta}{2} + \frac{\sqrt{3} \sin \theta}{2}$$

the terms c and s in Equation 2.33 are expanded. After some manipulation, the following simplified formula is obtained:

$$\frac{\bar{\alpha}^*}{\alpha_1} = 1 - \frac{\left[C_1 \tan \theta (\sin(2\theta) + \sqrt{3} \cos(2\theta)) - 12 (\cos \theta + \sqrt{3} \sin \theta)^2 \right] \left(\frac{\alpha_2}{\alpha_1} - 1 \right)}{C_1 (\sqrt{3} \cos \theta - \sin \theta)^2 + 12 (\cos \theta + \sqrt{3} \sin \theta) \left(\cos \theta + \sqrt{3} \sin \theta + 2 \frac{E_1 A_1}{E_2 A_2} \right)} \quad (2.34)$$

The expression in Equation 2.34 describes the thermal expansion of the original unit cell configuration with bonded joints. When plotted and compared to Equation 2.3, the bonded joint solution obtained from the result by Berger et al. [5], it is found that they are identical.

To determine the net CTE of the new geometry, the thermal expansion contribution from the spacers is now considered. Since the spacers do not influence the CTE or stiffness of the original lattice geometry, the thermal expansion of the new configuration is simply a sum of the two components. Consider the new lattice geometry as shown in Figure 2.11. It is clear from this figure that the new unit cell length is $L = L^* + \ell_3$, where L^* and ℓ_3 are the lengths of the original unit cell and spacer respectively. The subsequent relation is thus derived:

$$dL = dL^* + d\ell_3 \quad (2.35)$$

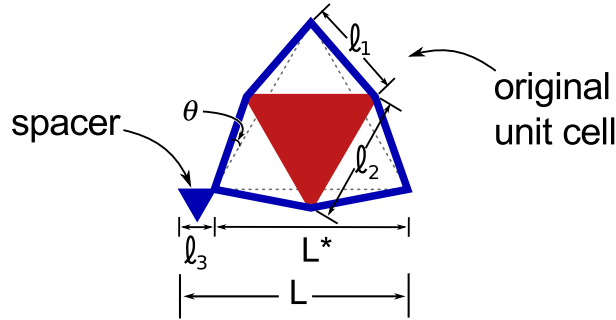


Figure 2.11: Illustration of new geometry consisting of original unit cell plus a spacer.

From the definition of thermal expansion, the following expressions are obtained:

$$\bar{\alpha} = \frac{1}{L} \frac{dL}{dT} \quad (2.36)$$

$$\bar{\alpha}^* = \frac{1}{L^*} \frac{dL^*}{dT} \quad (2.37)$$

$$\alpha_1 = \frac{1}{\ell_3} \frac{d\ell_3}{dT} \quad (2.38)$$

Combining Equations 2.35–2.38 gives:

$$\begin{aligned} \bar{\alpha} &= \frac{1}{L^* + \ell_3} \frac{dL^* + d\ell_3}{dT} \\ &= \bar{\alpha}^* \left(1 - \frac{\ell_3}{L}\right) + \alpha_1 \frac{\ell_3}{L} \end{aligned}$$

Normalizing $\bar{\alpha}$ with respect to α_1 therefore results in:

$$\frac{\bar{\alpha}}{\alpha_1} = \frac{\bar{\alpha}^*}{\alpha_1} \left(1 - \frac{\ell_3}{L}\right) + \frac{\ell_3}{L} \quad (2.39)$$

Finally, substituting $\bar{\alpha}^*/\alpha_1$ from Equation 2.34 into Equation 2.39 gives:

$$\frac{\bar{\alpha}}{\alpha_1} = 1 - \frac{\left[C_1 \tan \theta (\sin(2\theta) + \sqrt{3} \cos(2\theta)) - 12 (\cos \theta + \sqrt{3} \sin \theta)^2 \right] \left(\frac{\alpha_2}{\alpha_1} - 1 \right) \left(1 - \frac{\ell_3}{L} \right)}{C_1 (\sqrt{3} \cos \theta - \sin \theta)^2 + 12 (\cos \theta + \sqrt{3} \sin \theta) \left(\cos \theta + \sqrt{3} \sin \theta + 2 \frac{E_1 A_1}{E_2 A_2} \right)} \quad (2.40)$$

The thermal expansion of a bonded joint lattice with spacers is therefore predicted by Equation 2.40.

Thermal Properties

The analytical solution for the normalized CTE of a bonded joint lattice with spacers is given by Equation 2.40 as derived above. Examining this expression reveals that the addition of spacers increases $\bar{\alpha}/\alpha_1$ as expected and observed with the assumption of pinned joints. The spacers' influence on $\bar{\alpha}$ is similar to the case where the joints of the lattice are pinned. In the limit that ℓ_3/L equals 1, $\bar{\alpha}$ becomes α_1 . On the other extreme where $\ell_3/L = 0$, Equation 2.34 which describes the thermal expansion of the original unit cell with bonded joints is recovered. Since the thermal expansion of the spacer and original configuration are independent of one another, the total CTE of the lattice is simply a linear combination of both components. As ℓ_3 increases, so does the thermal expansion of the system. By designing the original unit cell to have a negative thermal expansion, the net CTE of the overall structure can be averaged to equal zero [5]. To offset the increment in CTE due to the spacers, either θ or $\Sigma = \alpha_2/\alpha_1$ can be increased.

From Equation 2.40, it is evident that $\bar{\alpha}/\alpha_1$ is dependent on the mechanical properties and sizes of the members. With bonded joints, the members cannot rotate freely, thus the rigidity of the members will restrict the movement of the nodes. As a result, the bonded joints increase the net CTE of the lattice because the thermal expansion of the members are not ideally accommodated. The dimensionless parameter E_1A_1/E_2A_2 which appears in the denominator represents the ratio between the stiffness and cross-sectional areas of type 1 and 2 constituents. This value is typically close to 1 and has little influence on the overall expression. The term C_1 , however, is many orders of magnitude larger and is a dominant factor. C_1 is defined as $A_1\ell_1^2/I_1$, where $I_1 = A_1r_1^2$ and r_1 is the radius of gyration of type 1 members. For a lattice with spacers, the slenderness ratio of type 1 members is more conveniently defined to be r_1/ℓ_1 instead of r_1/L , since L now includes the length of the spacer. As elucidated by Steeves et al. [61] and discussed in Section 2.1.2, when constituent 1 members become infinitely slender, the joints in a bonded lattice are effectively pinned. This is a consequence of the stiffness going to zero as the members become thinner. Combining the definition of C_1 with the second moment of area gives $C_1 = (\ell_1/r_1)^2$. Thus as $r_1/\ell_1 \rightarrow 0$, $C_1 \rightarrow \infty$, and Equation 2.40 is found to reduce to Equation 2.17, the expression for a pinned joint lattice with spacers.

Figure 2.12 plots $\bar{\alpha}/\alpha_1$ as a function of θ using Equation 2.40 for different combinations of r_1/ℓ_1 and ℓ_3/L to illustrate the influence of spacers and bonded joints. The resulting curves are also compared to a baseline configuration (blue dashed line) in which there

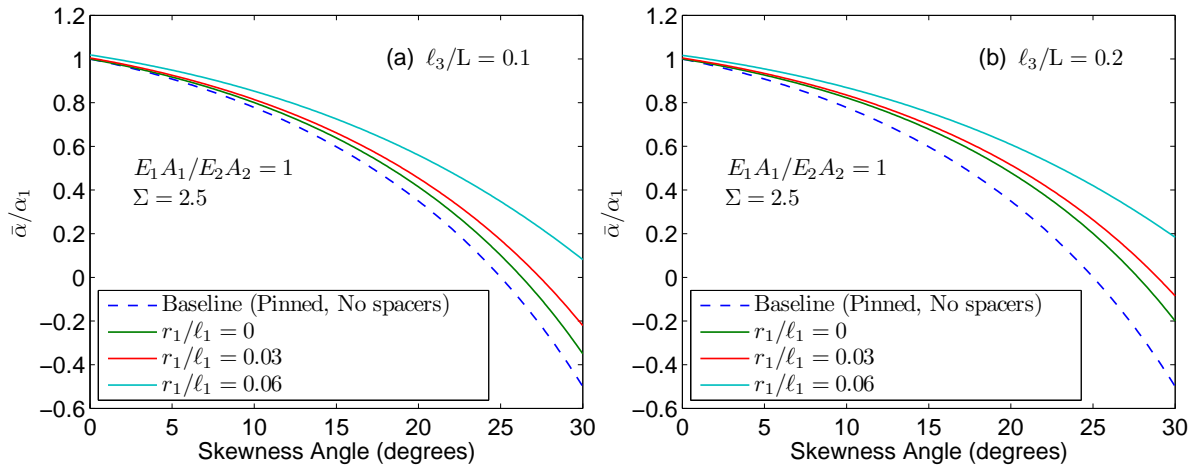


Figure 2.12: $\bar{\alpha}/\alpha_1$ plotted as a function of θ for (a) $\ell_3/L = 0.1$ and (b) $\ell_3/L = 0.2$ and different values of r_1/ℓ_1 .

are no spacers and the joints are pin connected (Equation 2.1). In Figure 2.12 (a), the curves for a lattice with $\ell_3/L = 0.1$ are contrasted with the reference configuration. When $r_1/\ell_1 = 0$, the unit cell is effectively pin-jointed, thus the thermal expansion behaviour is close to that of the baseline. The deviation between the two results is due to the thermal expansion contribution from the spacers. As the slenderness ratio of the type 1 member increases, the CTE increases and the curves begin to diverge quickly from the baseline properties. Only slight differences are noted when r_1/ℓ_1 goes from 0 to 0.03, but a significant increase is observed between $r_1/\ell_1 = 0.03$ and 0.06. Similar trends and behaviour are noted in Figure 2.12 which plots the normalized CTEs of a lattice with $\ell_3/L = 0.2$. The curves in this scenario show greater differences when compared to the baseline since the spacers are larger and cause a greater increase to the overall CTE of the structure.

2.3 Numerical Investigation

To validate the analytical solutions derived in Section 2.2, a FE study is performed to simulate the thermal expansion of a bi-material lattice. Models are created using ABAQUS [15], a FE software package developed by Dassault Systèmes. Following the design by Steeves et al. [61], the simulated lattice is constructed from Al and Ti constituents. The aspect ratio of the Ti members is defined to be $AR = \ell_1/h_1$, where h_1 is the width of the struts. Six families of unit cells with different combinations of configurations are studied in this investigation with $\ell_3/L = 0.1$ and 0.2, and $AR = 25, 12.5,$ and 6.25. For each family of unit cells, the skewness angle is varied between 17–31° in 2° increments to determine the variation in $\bar{\alpha}$ as a function of θ . The numerical results obtained from simulation are then compared to those predicted by Equations 2.17 and 2.40.

2.3.1 Finite Element Model

Two dimensional models are used to replicate the unit cell since the lattice structures are planar in nature. An exemplary FE model is illustrated in Figure 2.13 for a unit cell having $\ell_3/L = 0.1$, $AR = 12.5$, and $\theta = 25^\circ$. The red and blue meshes represent the Al and Ti constituents respectively. Both constituents are assumed to behave elastically with isotropic mechanical and thermal behaviour. Table 2.1 summarizes the material properties of Al and Ti used in the FE simulations. By taking advantage of symmetry,

Table 2.1: Mechanical and thermal properties of materials used in FE simulations.

Material	Young's modulus, E (GPa)	Poisson's ratio, ν	CTE, α (ppm/K)
Al	70	0.35	24.0
Ti	116	0.32	9.4

only one sixth of the unit cell is considered while applying the appropriate boundary conditions [61]. Nodes that lie on the lines of symmetry AB and BC are constrained to displace along those lines. The intersection of the two lines of symmetry, point B, represents the centre of the unit cell, therefore this point is fixed. A periodic boundary exists along the centroid of the spacer as depicted by the dashed line AD in Figure 2.13. Nodes on the periodic boundary are allowed to displace in both the x and y directions, subject to the constraint that the slope of AD be fixed. A total of 1,620 linear quadrilateral plane stress elements (500 for Al part and 1120 for Ti part) are used in the analysis. To simulate a bonded joint configuration, the degrees of freedom of the nodes at the material interface are tied together. The non-linear geometry setting is activated to account for non-linearities arising from large displacement and contact problems.

To determine the thermal expansion of a given unit cell, the modeled structure undergoes a temperature change of +180 K. After the Al and Ti members have expanded, the vertical displacement of point A is used to calculate the net CTE of the structure.

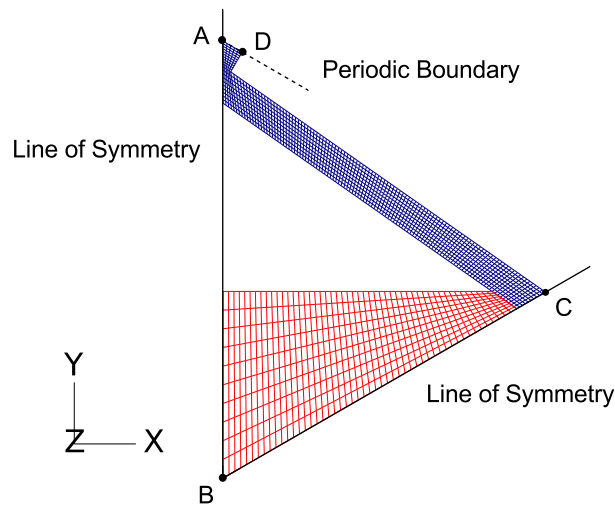


Figure 2.13: ABAQUS model and boundary conditions used to simulate one sixth of a unit cell where $\ell_3/L = 0.1$, $AR = 12.5$, and $\theta = 25^\circ$. Red and blue meshes represent Al and Ti members respectively.

The distance from A to B, ℓ_{AB} , is related to the total length of the unit cell through the geometric relation $\ell_{AB} = L/\sqrt{3}$. Thus, the net coefficient of thermal expansion is given by:

$$\bar{\alpha} = \frac{1}{\ell_{AB}} \frac{d\ell_{AB}}{dT}$$

In this study, the material properties are not a function of temperature, thus the net CTE is also assumed to be independent of temperature. Thus, given the displacement of point A Δ_{AB} , due to a temperature change ΔT , the net CTE is approximated by:

$$\bar{\alpha} = \frac{1}{\ell_{AB}} \frac{\Delta\ell_{AB}}{\Delta T} \quad (2.41)$$

2.3.2 Results and Comparison

The resulting configuration of a unit cell with $\ell_3/L = 0.1$, $AR = 12.5$, and $\theta = 25^\circ$ after thermal expansion has occurred is depicted in Figure 2.14. As before, the red and blue meshes represent the Al and Ti constituents respectively. The displacements in this figure are exaggerated by a factor of 40 to clearly illustrate the expansion and bending of the members. Due to the bonded joint configuration, the rotation of the Ti strut is restricted, thus it is forced to bend due to the change in member lengths which result from thermal expansion effects. Using the displacement of point A, the overall CTE of the unit cell is obtained via Equation 2.41. This calculation is repeated for different

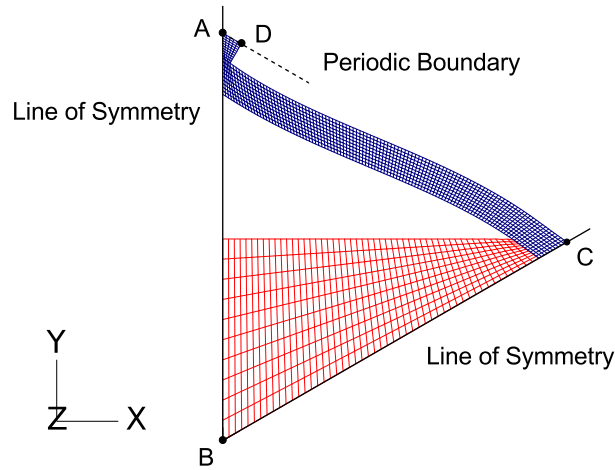


Figure 2.14: Unit cell with $\ell_3/L = 0.1$, $AR = 12.5$, and $\theta = 25^\circ$ after thermal expansion. Red and blue meshes represent Al and Ti constituents respectively and displacements are scaled by a factor of 40 for clarity.

skewness angles between $17\text{--}31^\circ$, thus the CTE of each unit cell family is determined as a function of skewness angle.

Results from the FE analyses are first compared to the CTEs predicted by the analytical expression for a pinned joint lattice as given by Equation 2.17. The six curves obtained from simulation are plotted under two categories where $\ell_3/L = 0.1$ and 0.2 in Figures 2.15 (a) and (b) respectively as shown by the dashed lines. Actual data points obtained from simulation are indicated by the 'x' markers and the theoretical CTEs given by Equation 2.17 are illustrated by the solid black line. Excellent agreement is found between the pinned joint expression and FE simulations when $AR = 25$. The difference between the predicted CTEs is roughly 0.2 ppm/K when $\theta = 17^\circ$ and grows to approximately 0.6 ppm/K when $\theta = 31^\circ$. The CTEs given by Equation 2.17 are consistently less than those obtained from FE simulation because the expression was derived under the assumption of a pinned joint lattice. As elucidated in Section 2.1.2, bonded joints impede the rotation of the lattice members and has the effect of increasing the overall CTE of the structure. When $AR = 25$, the slenderness ratio of the type 1 members is approximately 0.01 , thus the effect of having bonded joints in the FE model is small, and minimal deviations are observed between theory and simulation. However, as the Ti members become stubbier and the aspect ratio decreases to 12.5 and 6.25 , these differences grow larger and the CTEs from numerical simulation become significantly greater than those

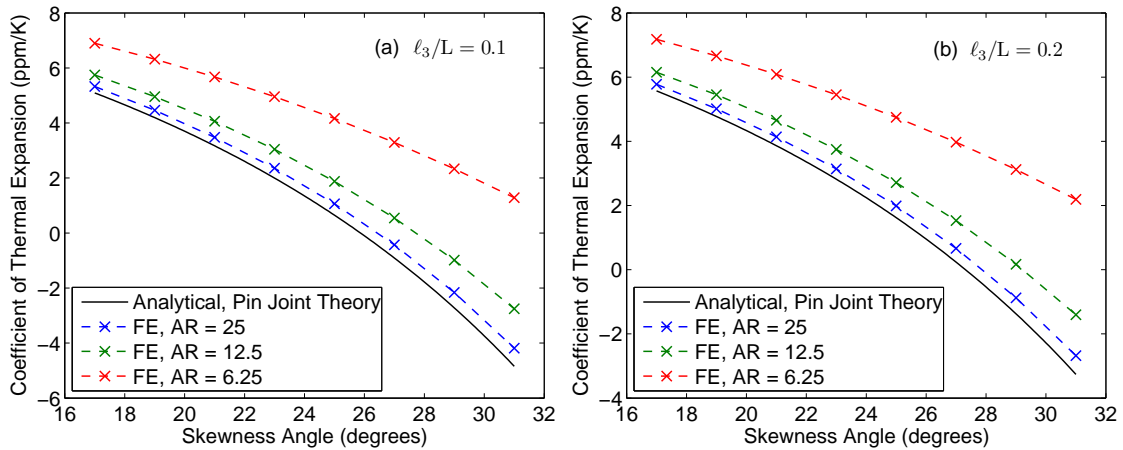


Figure 2.15: Predicted CTE of Al/Ti lattices from FE simulations and pinned joint theory (Equation 2.17). Results for unit cells with $\ell_3/L = 0.1$ and 0.2 are illustrated in parts (a) and (b) respectively.

calculated from Equation 2.17. Thus, the analytical expression for a pinned joint lattice can be successfully applied to predict the thermal expansion of lattices where the aspect ratio of type 1 members is high, but fails to give accurate results as AR becomes small.

To obtain more realistic estimates as the Ti members become thicker, its bending resistance must be taken into account as considered by Equation 2.40. Recall that the normalized CTE of a bonded-joint lattice with spacers has the form:

$$\frac{\bar{\alpha}}{\alpha_1} = 1 - \frac{\left[C_1 \tan \theta (\sin(2\theta) + \sqrt{3} \cos(2\theta)) - 12 (\cos \theta + \sqrt{3} \sin \theta)^2 \right] \left(\frac{\alpha_2}{\alpha_1} - 1 \right) \left(1 - \frac{\ell_3}{L} \right)}{C_1 (\sqrt{3} \cos \theta - \sin \theta)^2 + 12 (\cos \theta + \sqrt{3} \sin \theta) \left(\cos \theta + \sqrt{3} \sin \theta + 2 \frac{E_1 A_1}{E_2 A_2} \right)}$$

Additional terms in conjunction to ℓ_3/L are now required to plot $\bar{\alpha}$ as a function of θ . Assuming a unit depth in the 2D model and given that $I = bh^3/12$ for a rectangular beam, it can be shown that $C_1 = 12AR^2$. The ratio A_1/A_2 is determined by dividing the width of the Ti strut, h_1 , by the width of the Al member, h_2 , measured at roughly its midpoint as illustrated in Figure 2.16. The value of A_1/A_2 changes primarily as a function of AR , but is also dependent on the skewness angle. E_1/E_2 is a constant and is calculated using the elastic moduli of the lattice constituents. Thus, using Equation 2.40 to predict the thermal expansion of the lattices simulated in ABAQUS yields the results shown in Figures 2.17 (a) and (b). Comparing the analytical and FE solutions reveals excellent agreement for both $\ell_3/L = 0.1$ and 0.2 when $AR = 25$. In this instance, the CTEs calculated from simulation and Equation 2.40 are within 0.5 ppm/K of each other. When AR decreases to 12.5 or 6.25 however, large discrepancies are still observed between the theoretical and simulated CTE curves. Although the bonded joint expression correctly gives an increase in CTE with lower AR , the difference is inadequate to match the results

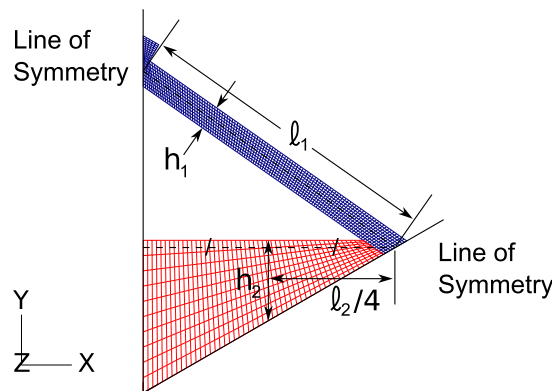


Figure 2.16: Schematic diagram of unit cell illustrating the widths of Ti and Al members, h_1 and h_2 respectively, used to calculate the ratio A_1/A_2 .

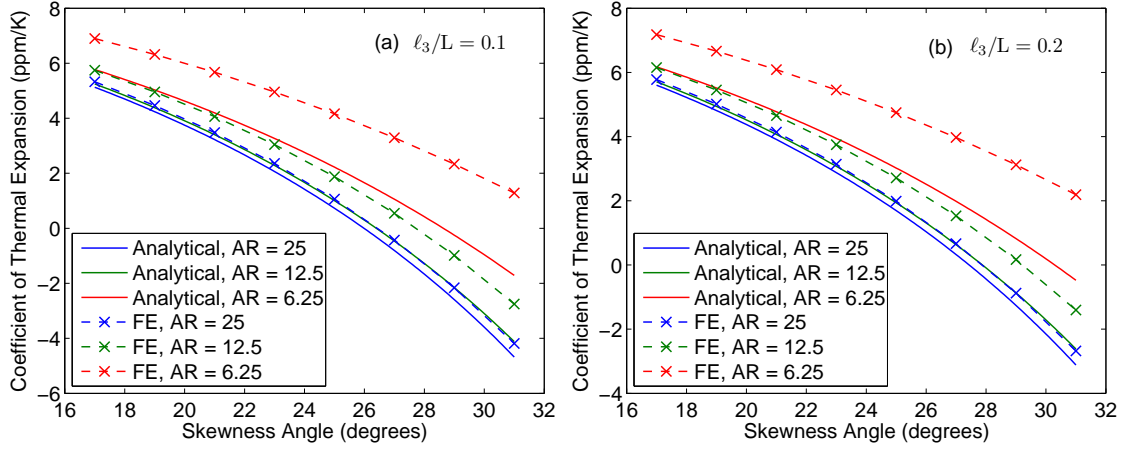


Figure 2.17: Predicted CTE of Al/Ti lattices from FE simulations and bonded joint theory (Equation 2.40). Results for unit cells with $\ell_3/L = 0.1$ and 0.2 are illustrated in parts (a) and (b) respectively.

from the FE study. When the skewness angle is 31° , the disparity between the solutions is approximately 1.3 and 3.0 ppm/K when AR is 12.5 and 6.25 respectively. Thus when the aspect ratio of the Ti struts is high, the analytical expression accurately reproduces the thermal expansion behaviour observed from simulation, as with Equation 2.17. As the type 1 members become thicker however, Equation 2.40 fails to give accurate results.

The incongruence among the simulated and theoretical results is attributed to the difference between the defined length of ℓ_2 and its true value in the unit cell model. The Al members must accommodate the finite thickness of the Ti struts, thus they are shorter than ideal. As the Ti members become thicker, this discrepancy becomes increasingly profound. To examine the consequence of this effect, the derivation of $\bar{\alpha}/\alpha_1$ for a bonded joint lattice is reconsidered. Upon substituting ℓ_1 and ℓ_2 into Equation 2.27, a scaling factor f is introduced such that:

$$f \equiv \ell'_2/\ell_2 \quad (2.42)$$

where ℓ'_2 is the true length of the Al members. To derive an expression which takes into account the actual size of type 2 constituents, all instances of ℓ_2 are replaced by $f\ell_2$ and thus Equation 2.27 becomes:

$$d_{1y} = \frac{\alpha_1 \left[\sqrt{3}C_1c + 12f \frac{E_1A_1}{E_2A_2} s (\sqrt{3}c + s) \right] - f\alpha_2 \left[C_1s (\sqrt{3}s - c) - 12s^2 (\sqrt{3}c + s) \right] \frac{L^* dT}{2 \cos \theta}}{\sqrt{3} \left(C_1c^2 + 12s^2 + 12sf \frac{E_1A_1}{E_2A_2} \right)} \quad (2.43)$$

Following through with the original derivation produces the following result:

$$\frac{\bar{\alpha}}{\alpha_1} = 1 - \frac{\left[C_1 \tan \theta (\sin (2\theta) + \sqrt{3} \cos (2\theta)) - 12 (\cos \theta + \sqrt{3} \sin \theta)^2 \right] \left(f \frac{\alpha_2}{\alpha_1} - 1 \right) \left(1 - \frac{\ell_3}{L} \right)}{C_1 (\sqrt{3} \cos \theta - \sin \theta)^2 + 12 (\cos \theta + \sqrt{3} \sin \theta) \left(\cos \theta + \sqrt{3} \sin \theta + 2f \frac{E_1 A_1}{E_2 A_2} \right)} \quad (2.44)$$

The terms α_2/α_1 and $E_1 A_1/E_2 A_2$ in Equation 2.44 are now multiplied by the scaling factor f . This is equivalent to replacing α_2 and E_2 in the original expression by $f\alpha_2$ and E_2/f respectively. Physically, this is explained by having to scale the thermal expansion coefficient and Young's modulus of the type 2 constituents to account for their true length. Since the Al members are shorter, the effective thermal expansion is lower than in the ideal scenario. A decrease in ℓ_2 also makes the type 2 members stiffer, which is reflected by an increase in E_2 .

The scaled theoretical expression for the normalized CTE of a bonded joint lattice with spacers as given by Equation 2.44 is thus compared to the FE simulations performed in ABAQUS. To determine ℓ'_2 , the length of the Al member is measured from the midpoint of contact as illustrated in Figure 2.18. The horizontal distance from point F, the midpoint of line segment EG, to the vertical line of symmetry is thus equal to half of ℓ'_2 . f is therefore a function of the thickness of type 1 members, and the skewness angle of the unit cell. The predicted CTE of the different families of lattices given by the scaled expression in Equation 2.44 are plotted in comparison to the FE results in Figures 2.19 (a) and (b). Excellent agreement is now observed between the analytical and simulated CTEs for all combinations of θ , ℓ_3/L , and AR . Differences of less than 0.6 ppm/K are found between the two sets of data. The scaled analytical solution gives more accurate results for lower values of AR when compared to Equation 2.40 because the scaling factor

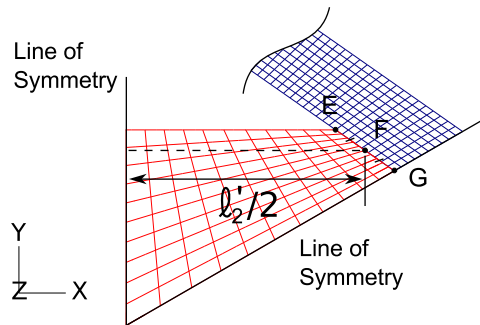


Figure 2.18: Method for determining the actual length of the Al members, ℓ'_2 , is identified in this schematic diagram of the material interface in a unit cell.

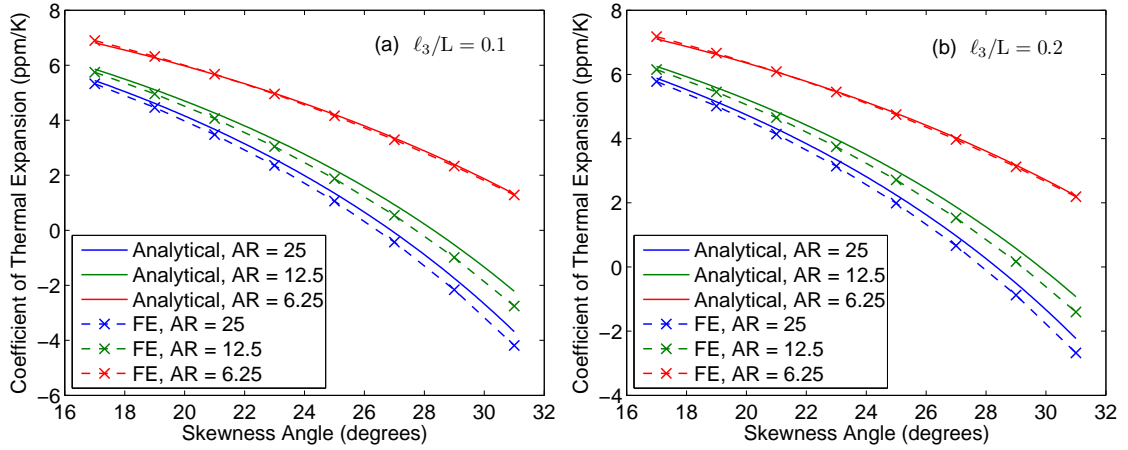


Figure 2.19: Predicted CTE of Al/Ti lattices from FE simulations and the scaled bonded joint theory (Equation 2.44). Results for unit cells with $\ell_3/L = 0.1$ and 0.2 are illustrated in parts (a) and (b) respectively.

becomes increasingly relevant as the Ti struts become thicker. By adjusting α_2 and E_2 accordingly, more representative CTEs are obtained. Thus for unit cells where the aspect ratio of the type 1 members is relatively low, it is important to consider the effective length of ℓ_2 when estimating the theoretical thermal expansion behaviour.

Chapter 3

Molecular Dynamics Study of Amorphous Materials

Molecular dynamics simulations are used to study the properties of amorphous materials in this chapter. To begin, a brief introduction to MD is given in Section 3.1 which summarizes some applications and basic theory. Inherent limitations and weaknesses of MD are also discussed in addition to parallel algorithms and codes. Section 3.2 discusses how molecular dynamics simulations are used to determine the thermal expansion and recrystallization behaviour of amorphous Al and Ti. The procedures used to quantify their CTE, recrystallization temperature, and change in volume due to devitrification are described here in detail.

3.1 Overview of Molecular Dynamics

3.1.1 Background Information and Applications

Molecular dynamics is an atomistic modeling technique in which individual atoms are simulated and the temporal evolution of a system is tracked by computing the trajectory of each atom. In contrast, continuum mechanics assumes materials are continuous with constitutive equations describing their behaviour. This simplified description of materials is generally applicable to length scales on the order of microns and larger [69]. With a continuum approach, local atomic structures and variations are smeared out, thus the model breaks down in situations where discrete atomic structure is important. Continuum mechanics is unsuitable for studying microstructure effects such as dislocations, and

crack nucleation [26]. MD, on the other hand, is a powerful tool that can be used to study microscopic systems such as defects in crystals, fracture mechanisms, and biomolecules [21]. Since the trajectory of individual atoms are followed, MD simulations can easily provide snapshots of a system with atomic resolution and detail. Such images would be infeasible to obtain in a laboratory setting. Extreme conditions, such as high temperatures and pressures, can also be easily simulated on a computer that would otherwise be expensive or extremely difficult to perform experimentally.

The first reported MD simulation was performed in 1957 by Alder and Wainwright [2] who studied phase transitions in a hard sphere system where particles interact through instantaneous collisions. One of the first simulations to use a continuous potential was by Gibson et al. [28] in 1960 for investigating radiation damage. Over the past 5 decades, MD simulations have advanced considerably and have become increasingly feasible as computing power has grown. Early simulations in the 1960s contained only a few hundred atoms, where with current technology, simulations can contain millions to billions of atoms [69]. MD simulations are widely used today in a variety of research fields including biochemistry, physics, and nanomaterials. Some specific applications include studying a self-assembling surfactant-water solution [36], simulation of an atomic force microscopy (AFM) probe [11], and examining mechanical properties of fivefold twinned copper nanowires [9].

3.1.2 Governing Equations

In MD simulations, the path traveled by an atom is determined by repeatedly solving its equation of motion. The dynamics of each particle are governed by classical mechanics, such as Newton's second law:

$$\mathbf{F}_i = m_i \mathbf{a}_i \quad (3.1)$$

Boldface terms indicate vector quantities and the subscript i denotes the property belonging to the i^{th} atom. In a simulation with N atoms, $3N$ equations of motion must therefore be solved to determine the trajectory of the system, one for each atom and coordinate direction. From Equation 3.1, it is apparent that the acceleration of the i^{th} atom is given by the forces acting on the atom, divided by its mass. To determine the acceleration, and hence trajectory, the atomic forces must be known. The driving mechanism and engine behind MD lies in how the particles interact with one another. The interaction between atoms is defined via a potential function, which describes the potential energy

of the system given the coordinates of the atoms: $U(\mathbf{r}_1, \dots, \mathbf{r}_N)$. Thus the atomic forces are given by the negative gradient of the potential with respect to the atom coordinates as follows:

$$\mathbf{F}_i = -\nabla_{\mathbf{r}_i} U(\mathbf{r}_1, \dots, \mathbf{r}_N) \quad (3.2)$$

With the atomic forces and hence accelerations known, the 3N equations of motion given in Equation 3.1 are integrated with respect to time to determine the movement of all particles in the system. An MD code therefore requires an integration scheme to compute the temporal evolution of a system.

Time integration algorithms are often based on finite difference methods. Predictor-corrector algorithms by Gear [25] are also used but are not discussed in this overview. The idea behind finite difference methods is to use discretized timesteps Δt , and information at the current time t , to compute quantities at a later time $t + \Delta t$. The most commonly used integration scheme in MD simulations is the Verlet algorithm [68], which is derived from a Taylor series expansion about the atomic coordinates at time t :

$$\mathbf{r}(t + \Delta t) = \mathbf{r}(t) + \mathbf{v}(t)\Delta t + (1/2)\mathbf{a}(t)\Delta t^2 + (1/6)\mathbf{b}(t)\Delta t^3 + O(\Delta t^4) \quad (3.3a)$$

$$\mathbf{r}(t - \Delta t) = \mathbf{r}(t) - \mathbf{v}(t)\Delta t + (1/2)\mathbf{a}(t)\Delta t^2 - (1/6)\mathbf{b}(t)\Delta t^3 + O(\Delta t^4) \quad (3.3b)$$

The quantity $\mathbf{b}(t)$ represents the third time derivative of the atomic positions. Adding the above equations together cancels out the third derivative terms and gives:

$$\mathbf{r}(t + \Delta t) = 2\mathbf{r}(t) - \mathbf{r}(t - \Delta t) + \mathbf{a}(t)\Delta t^2 + O(\Delta t^4) \quad (3.3c)$$

The error associated with future atomic coordinates in Equation 3.3c is $O(\Delta t^4)$, thus small timesteps are chosen to give accurate results. Note that $\mathbf{r}(t + \Delta t)$ depends on $\mathbf{r}(t - \Delta t)$ and therefore cannot be evaluated at $t = 0$. In this situation, the forward Taylor series expansion (Equation 3.3a) can be used to evaluate the first timestep to $O(\Delta t^3)$ accuracy. Although velocities are not needed to determine the trajectory, they are required to compute the kinetic energy and temperature of the system which are often of interest. Velocities are not computed explicitly using the Verlet scheme but can be determined from the atomic positions using the following equation:

$$\mathbf{v}(t) = \frac{\mathbf{r}(t + \Delta t) - \mathbf{r}(t - \Delta t)}{2\Delta t} \quad (3.4)$$

Note that Equation 3.4 is only $O(\Delta t^2)$ accurate, and is computed for the current time rather than $t + \Delta t$.

The velocity Verlet algorithm [21] is a variation of the original Verlet scheme in which $\mathbf{r}(t + \Delta t)$ and $\mathbf{v}(t + \Delta t)$ are computed using the following equations:

$$\mathbf{r}(t + \Delta t) = \mathbf{r}(t) + \mathbf{v}(t)\Delta t + (1/2)\mathbf{a}(t)\Delta t^2 \quad (3.5a)$$

$$\mathbf{v}(t + \Delta t) = \mathbf{v}(t) + (1/2)\mathbf{a}(t)\Delta t + (1/2)\mathbf{a}(t + \Delta t)\Delta t \quad (3.5b)$$

Using the velocity Verlet scheme, no information from time $t - \Delta t$ is required, and velocities are computed explicitly in this scheme for time $t + \Delta t$. With Equation 3.5, Newton's equations of motion can be repeatedly integrated for all atoms in the system to compute its trajectory. The evolution of a simulation is therefore exactly determined given an initial configuration since the governing dynamics are deterministic.

3.1.3 Interatomic Potentials

As stated in the previous section, the motion of atoms in an MD simulation are governed by classical mechanics, and the atomic forces are derived from a potential function. The potential function plays a critical role because it defines the properties and behaviour of the atomic interaction. It is therefore important to use an interatomic potential that accurately describes the system of interest. Many classes of potentials are available to choose from depending on the application. Simplistic potentials are typically only adequate for describing basic systems. More complicated potentials are more accurate in reflecting certain physical systems, however there are computational trade-offs. Potential functions are typically dependent only on the relative positions of the interacting atoms [21], although some are a function of the bond order or bond angles between atoms [63]. For brevity, only the following potentials will be introduced: (i) pair potentials, and (ii) empirical many-body potentials.

Pair Potentials

As the name suggests, pair potentials describe the potential energy between two particles. The total potential of a given particle is thus obtained by summing the pairwise interaction between all pairs in the system. In practice, a cutoff radius is used to consider only nearby particles and neglect long range interaction forces [63]. Examples of pair potentials include the Morse potential [47], and Lennard Jones (LJ) potential [34]. The LJ potential is perhaps the most widely used pair potential function and has the

form:

$$U(r_{ij}) = 4\epsilon \left[\left(\frac{\sigma}{r_{ij}} \right)^{12} - \left(\frac{\sigma}{r_{ij}} \right)^6 \right] \quad (3.6)$$

where ϵ is the binding energy and σ is the finite distance where the potential is zero. The term proportional to r^{-12} describes the repulsion between two atoms due to the Pauli principle, while the term proportional to r^{-6} models the attraction originating from van der Waals interaction [21]. Due to the simple nature of the LJ potential, it is only suitable for modeling rare gases and fails when trying to simulate covalent or metallic systems. Although the LJ potential is unable to simulate certain materials, it is widely used to study fundamental issues in condensed matter physics [21]. In general, pair potentials are computationally inexpensive and straightforward to implement because of their simplistic description of atomic interactions. As a consequence, they are unable to accurately describe certain physical systems and have limited application to the study of real materials.

Empirical Many-Body Potentials

A many-body potential describes the interaction between three or more particles. These functions are more complicated than pair potentials, and therefore more expensive to compute. Empirical many-body potentials are optimized to reproduce values such as lattice constants, elastic constants, binding energies, and vacancy formation energies obtained through experiments or quantum mechanical calculations [69]. Examples of many-body potentials include the embedded-atom method (EAM) potential [16], Finnis-Sinclair potential [23], and the Tersoff potential [64].

Both the EAM and Finnis-Sinclair potentials are similar in construction and are commonly used to simulate metallic systems [26]. Under the EAM formulation, the total energy of the i^{th} atom, E_i , has the form:

$$E_i = F_\alpha \left(\sum_{j \neq i} \rho_\beta(r_{ij}) \right) + \frac{1}{2} \sum_{j \neq i} \phi_{\alpha\beta}(r_{ij}) \quad (3.7)$$

where F_α is the embedding energy of atom i , ρ_β is the electron density function, $\phi_{\alpha\beta}$ is a pair-wise potential, and r_{ij} is the distance between atoms i and j . The subscripts α and β represent the elements of atoms i and j respectively. The first term in Equation 3.7 describes the multi-body interaction of the particles and represents the energy required to embed atom i of type α into the system, given the electron density contribution from

all other atoms in the system (not including itself). The functions F_α , ρ_β , and $\phi_{\alpha\beta}$ are determined through fitting to material properties. The Finnis-Sinclair potential has the exact same form as the EAM potential, except the electron density becomes a function of both element types, thus ρ_β becomes $\rho_{\alpha\beta}$ in Equation 3.7. Many-body potentials are more difficult to implement and require extra computational resources because they consider the interactions between three or more particles. As a result, they are suitable for simulating a variety of materials where pair-wise potentials would otherwise fail.

3.1.4 Limitations

Although MD simulations are powerful tools, they are subject to some limitations. As noted in Section 3.1.2, each atom in the system is modeled individually and 3N equations of motion are integrated to determine the trajectory. As the number of atoms in the system increases, the computational cost and simulation time will grow. MD simulations are therefore often limited by the available computational resources. Using empirical many-body potentials, the upper limit on the number of atoms in a simulation ranges from 10^6 – 10^9 [69]. Due to the limited number of atoms that can be modeled, system sizes are generally on the order of nanometers in length. Simulations of large scale systems are not feasible with the computing power today.

The inherently short time scales accessible by MD simulations is another weakness of the modeling scheme. It is required that the timestep used in the finite difference integration scheme be small enough to resolve the vibrational modes of the atoms [69]. Since atoms vibrate at such high frequencies about their lattice positions, timesteps on the order of femtoseconds (10^{-15} s) must be used. Thus, the temporal evolution of the system is slow and the total simulated time is limited to nanoseconds or microseconds [69]. Due to the short timescales achievable by MD simulations, it can be difficult to study physical processes that occur over longer periods of time. For example, diffusional processes can occur over a period of minutes or hours, time scales currently inaccessible by MD.

The temporal and spatial regime accessible by MD simulations is illustrated in Figure 3.1 along with other modeling schemes [26]. On one end of the spectrum, quantum mechanics uses a first principles approach, thus it is limited to extremely short time and length scales because of the massive computational costs. As generalizations and assumptions are made, longer simulation times and sizes can be achieved, however there is

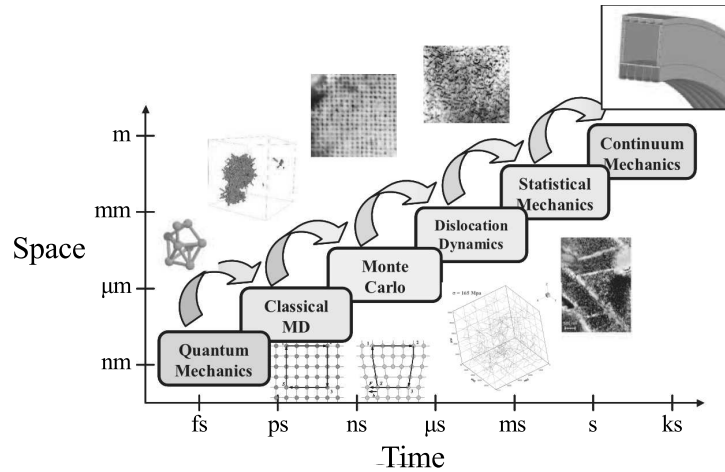


Figure 3.1: Typical length and time scales accessible by modeling methods, adapted from Ghoniem et al. [26].

a trade-off in the ability to model certain systems. One of the longest (roughly $1 \mu\text{s}$) and largest (5×10^9 particles, $0.4 \mu\text{m}$) MD simulations were performed by Duan and Kollman [19] in 1998 and Roth et al. [55] in 2000 respectively. Duan and Kollman [19] studied the folding of proteins, a phenomenon that occurs over a period of microseconds, while Roth et al. [55] demonstrated the ability of parallel MD codes and their scalability.

3.1.5 Parallel MD Codes and Scalability

To reduce computing time and facilitate the study of larger systems, parallel MD codes have been developed so that multiple processors can perform a single simulation. As noted before, the bulk of the computational work is due to force calculation and time integration. Since these tasks can be done independently, the work can be distributed over many computers. A variety of algorithms exist for parallelization which are listed here in increasing performance, but also difficulty in implementation [54]: (i) atomic decomposition (AD), (ii) force decomposition (FD), and (iii) spatial decomposition (SD). The AD algorithm distributes the atoms between the processors, which are responsible for their atoms throughout the entire simulation no matter where the atoms move. In the FD algorithm, the force matrix is divided among the computers, and the forces in each submatrix are computed by their respective processor. Lastly, SD splits the physical simulation space into P domains for P processors. Computations for all atoms within each partition are handled by their assigned processor. Out of the three algorithms it

can be shown that SD is the most effective — for large systems and a balanced workload, the computational time scales optimally as $O(N/P)$ for N atoms and P processors [54].

In this research, all MD simulations are performed using LAMMPS (Large-scale Atomic/Molecular Massively Parallel Simulator) [54], an open source classical MD code developed and maintained by Sandia National Laboratories under the United States Department of Energy. LAMMPS is an efficient parallel code which implements the SD algorithm, thus giving $O(N/P)$ scaling for large and balanced systems. Simulations are conducted using the General Purpose Cluster (GPC) on the University of Toronto’s SciNet Consortium [42] to take advantage of the scalability of LAMMPS and the available computational resources. Scaling tests are conducted on the GPC to determine the parallel performance of LAMMPS. Strong and weak scaling tests are carried out using a standard benchmarking input script from LAMMPS. The benchmark problem simulates a metallic (copper) system using an EAM potential and is therefore representative of the intended studies. The strong scaling test simulates a total of 4,000,000 atoms for 500 timesteps. In the case of the weak scaling test, 32,000 atoms per core are simulated for 500 timesteps. Figure 3.2 illustrates the results of the benchmark tests performed using different combinations of connection types and message passing interfaces (MPIs). With an Ethernet connection, both strong and weak tests show good scaling up until 16 cores (2 nodes), after which the performance begins to degrade. This is due to the latency in communication between the nodes and cores over the Ethernet connection. When the tests are repeated using an InfiniBand connection, excellent scaling is maintained to 512

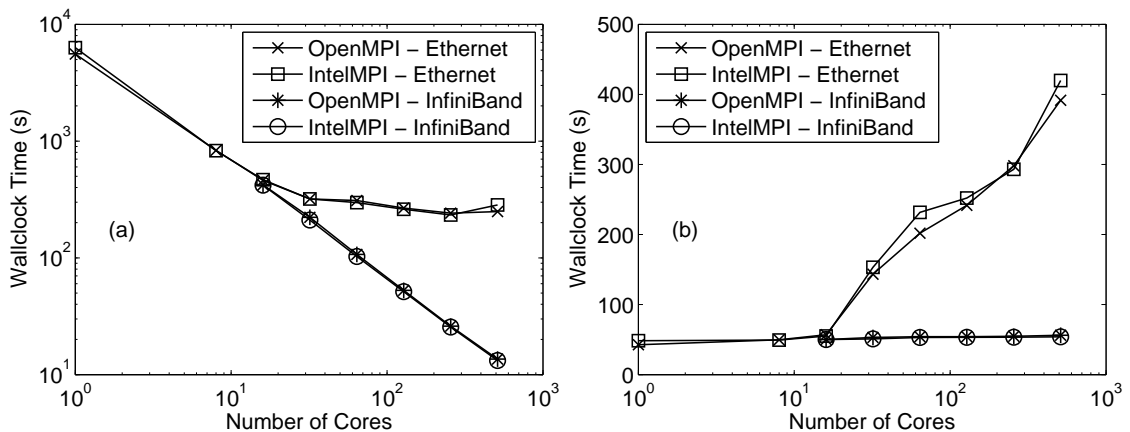


Figure 3.2: Results of strong and weak scaling tests plotted in parts (a) and (b) respectively for LAMMPS on SciNet’s GPC.

cores (64 nodes) and was not tested further. It can therefore be concluded that when using an Ethernet connection, no more than 16 cores should be used; InfiniBand must be used with more than 16 cores to maintain scalability. Furthermore, the tests reveal that IntelMPI has a slight advantage over OpenMPI. Results from these benchmarks are useful in planning MD simulations by determining the approximate computation time required for a simulation given the number of processors available.

3.2 Thermal Expansion and Recrystallization of Amorphous Al and Ti

3.2.1 Literature Review

Thermal Expansion

The application of low CTE lattices at the microscale requires special fabrication techniques. E-beam deposition is used to create thin films of Al and Ti, which are then etched to form a lattice structure. As a result of the deposition process, it has been determined by EBSD and XRD experiments that the thin films are amorphous. Consequently, knowledge of the thermal properties of amorphous Al and Ti are needed to successfully design a micro lattice with zero thermal expansion. The CTEs of polycrystalline Al and Ti have been thoroughly researched and documented in the literature [70, 59, 30]. There are however no studies, experimental or simulated, on the thermal properties of amorphous Al and Ti, thus their CTEs are investigated in this research via MD simulations.

Numerous studies have utilized MD simulations to determine the CTE of various materials. For example, Timon et al. [65] looked at the thermal expansion of Si and Ge, and Gan and Chen [24] investigated the CTE of Cu. From their studies, they found the CTE of Si, Ge, and Cu to be in good agreement with their well known experimental values, thus proving the predictive capability of MD simulations. From literature review, it is found that a common procedure is used to simulate the CTE of an element or compound. In general, the desired atoms and atomic arrangement are created in a system with periodic boundary conditions in all directions. Images of the simulation cell are replicated in the x , y , and z directions such that there are no free surfaces. Furthermore, an atom that passes through one face of the simulation cell will reappear on the opposite side with the same velocity. Periodic boundary conditions therefore emulate

an infinite system representing a material in bulk form. To study thermal expansion, MD simulations are conducted under an isothermal-isobaric (NPT) ensemble where the number of moles (N), pressure (P), and temperature (T) are conserved. Under these conditions, the system is allowed to expand and contract as the temperature is controlled. The material length is thus measured as a function of temperature and the instantaneous CTE is given by:

$$\alpha = \frac{1}{\ell} \frac{d\ell}{dT} \quad (3.8)$$

where ℓ is the temperature dependent length of the material. Although there have been numerous investigations on the thermal expansion of materials using molecular dynamics, there have been no reported studies on amorphous Al and Ti. MD simulations are therefore performed following a procedure similar to that found in the literature to determine the CTEs of amorphous Al and Ti.

Recrystallization

The phenomenon of an amorphous to crystalline transition is well known and can be initiated by a number of methods such as thermal annealing [45], and mechanical strain [12]. At sufficiently high temperatures, it is possible that the metastable amorphous states of Al and Ti will recrystallize due to thermally activated devitrification. It is therefore important to determine the temperature at which recrystallization occurs to accurately study and predict the behaviour of the bi-material lattice. Furthermore, it is known that amorphous structures tend to be less dense than crystalline states [39]. Therefore as a result of devitrification, a material will contract in volume and exhibit a negative change in length. The amount of shrinkage due to recrystallization must also be quantified to properly model and predict the lattice behaviour.

MD simulations have been utilized by a number of researchers to investigate the recrystallization temperature of various metallic glasses [44, 57, 52]. Amorphous states can be easily obtained and studied via computer simulations which makes MD an attractive tool. To create amorphous metals, it is typical to begin with a liquid state of the material at a temperature well above the melting point. Periodic boundary conditions are employed in all directions to simulate bulk material under the NPT ensemble. The metallic liquid is then rapidly quenched to below the glass forming temperature. To obtain metallic glasses for Ti/Al systems, quenching rates on the order of 0.1–1000 K/ps are used [57]. The rapid cooling process prevents the nucleation and growth of crystal structures, thus

an energetically unfavourable amorphous state can be obtained. Once a glassy metallic structure has been produced, the temperature of the system is increased at a typical rate of 1 K/ps [51]. During this process, the total volume and potential energy of the system is recorded as a function of temperature. When recrystallization occurs, the system will exhibit a sudden drop in both quantities as the atoms rearrange themselves into a more orderly and lower energy state [44]. The temperature at which this occurs is therefore denoted the recrystallization temperature, T_x .

A search of the literature reveals no experimental investigations on the devitrification of amorphous Al and Ti. Only MD studies exist, although scarce, that analyze the recrystallization temperature and volume change due to recrystallization. A couple of reports give T_x for amorphous Al, but their results are conflicting. Utilizing non-local pseudopotential theory, Lu and Szpunar [44] gives T_x of Al to be in the range of 550–630 K. In contrast, Shimono and Onodera [57] finds T_x to be approximately 230 K using the interatomic potential by Oh and Johnson [48]. Given the discrepancy between reported values, further investigation on the recrystallization of amorphous Al is warranted. Shimono and Onodera [57] also examined the devitrification of amorphous Ti and gives T_x to be roughly 280 K. The recrystallization temperatures for amorphous Al and Ti given by Shimono and Onodera [57] are both below room temperature (293 K). However, the amorphous thin films manufactured through e-beam deposition are known to be stable at room temperature, thus the values given by Shimono and Onodera [57] are inconsistent with current observations. Studies on the volume differences between amorphous and crystalline states for Al and Ti are scant. For Al, one report by Becquart et al. [4] gives $\Delta V/V = 10\%$ for a crystalline to amorphous transition at 300 K (or roughly -9% for devitrification), although the system studied was under an applied stress. No studies have been found that analyze and report the volume difference between amorphous and crystalline Ti. The MD studies in this section shall therefore fill this void and investigate the resulting volume changes of amorphous Al and Ti due to recrystallization.

3.2.2 Simulation Method

Selecting Interatomic Potentials

Appropriate potential functions must first be chosen to ensure good results from the MD simulations. Many-body interatomic potentials based on the EAM and Finnis-Sinclair approach are adopted because they are well suited to modeling metallic systems

as explained in Section 3.1.3. For both Al and Ti, there are a number of good interatomic potentials in the literature to choose from. A simple study is therefore conducted to select the most suitable potential for each material. To model Al, three potential functions are considered — those by Liu et al. [40] (improved version of original potential by Ercolessi and Adams [22]), Mendeleev et al. [46], and Zope and Mishin [74]. For Ti, the interatomic potentials by Ackland [1] and Zope and Mishin [74] are evaluated.

The objective of this study is to investigate the thermal expansion and devitrification of amorphous Al and Ti. The best potential is therefore one that most accurately predicts these physical properties and phenomena. Since experimental thermal expansion data is readily available for crystalline Al and Ti, the interatomic potentials that best reproduce their behaviour are selected as the most suitable candidates. Using each interatomic potential, the CTE of either Al or Ti is determined via MD simulations and compared against their experimental values. To simulate the thermal expansion of crystalline Al, a $20 \times 20 \times 20$ block of face-centred cubic cells corresponding to 32,000 atoms is created in LAMMPS. Similarly for Ti, a $20 \times 20 \times 20$ array of hexagonal close-packed unit cells (also 32,000 atoms) is constructed. Lattice constants of 4.05 \AA and 2.95 \AA are used for Al and Ti respectively [74]. The initial crystalline atomic structures of Al and Ti are visualized using Visual Molecular Dynamics (VMD) [31], a molecular visualization program, and shown in Figures 3.3 (a) and (b) respectively. The neat and ordered crystalline atomic arrangements of the two metals are clearly observed in these images. MD simulations are performed using a velocity-Verlet integration scheme and a timestep of 1 femtosecond (fs). Periodic boundaries are enforced in all directions to eliminate

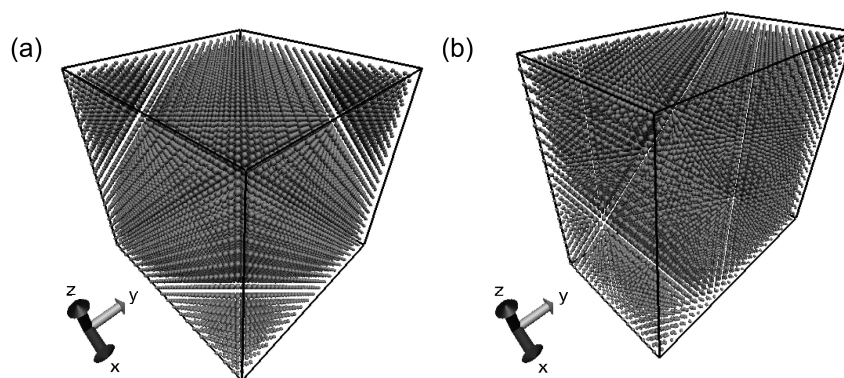


Figure 3.3: Initial atomic configurations of crystalline Al and Ti in figures (a) and (b) respectively. Black lines indicate the edges of the periodic simulation cell.

surface effects and thus emulate bulk material. At the beginning of the simulations, the system is equilibrated at 50 K for 100 picoseconds (ps). The isobaric-isothermal ensemble is employed with zero external pressure acting on the system and the simulation box is allowed to expand anisotropically. After the system is in an equilibrium state, the temperature of the system is increased from 50 K to 1000 K at a rate of 1 K/ps. During heating, the size of the simulation box in the x , y , and z directions (ℓ_x , ℓ_y , and ℓ_z) are recorded and subsequently used to calculate the thermal expansion of the material. The CTE is calculated as the mean thermal expansion in each direction and is given by:

$$\begin{aligned}\alpha(T) &= \frac{1}{3} [\alpha_x(T) + \alpha_y(T) + \alpha_z(T)] \\ &= \frac{1}{3} \left[\frac{1}{\ell_x(T)} \frac{d\ell_x(T)}{dT} + \frac{1}{\ell_y(T)} \frac{d\ell_y(T)}{dT} + \frac{1}{\ell_z(T)} \frac{d\ell_z(T)}{dT} \right]\end{aligned}\quad (3.9)$$

In Equation 3.9, the derivatives of the box lengths with respect to temperature are required to compute the CTE. To obtain this information, cubic polynomials are used to approximate the simulation data. Given a polynomial interpolant, it is straightforward to evaluate $\ell_i(T)$ and $d\ell_i(T)/dT$ at any temperature, where i is x , y , or z .

As an example, the simulation box lengths for Al using the potential by Mendeleev et al. [46] are plotted in Figure 3.4 as a function of temperature. Cubic polynomials used to fit the raw data are also illustrated as dashed lines for comparison. Thermal expansion in the x , y , and z directions are practically identical due to its symmetrical face-centred cubic crystalline structure. ℓ_x , ℓ_y , and ℓ_z are observed to vary and expand smoothly as the temperature of the system is increased. The fitted polynomials are also shown to

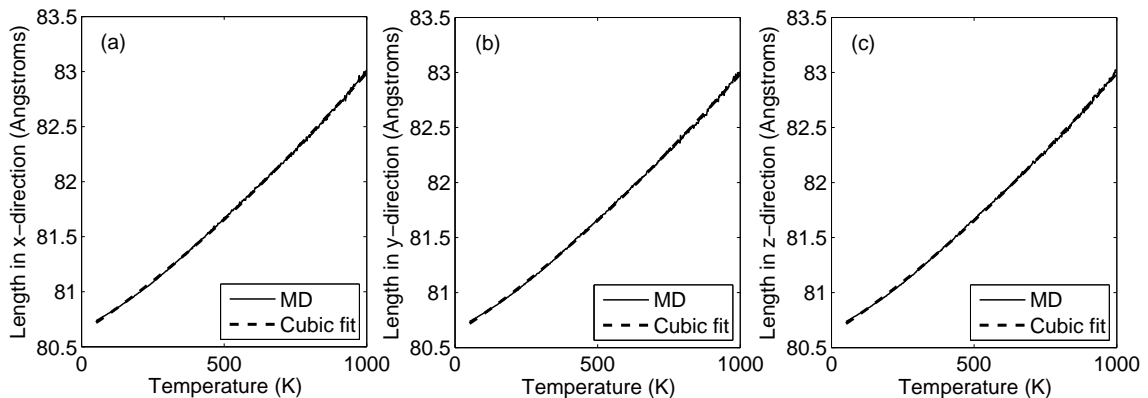


Figure 3.4: ℓ_x , ℓ_y , and ℓ_z plotted as a function of temperature in figures (a), (b), and (c) respectively using the potential by Mendeleev et al. [46] to simulate the thermal expansion of Al. Raw and fitted data are shown as solid and dashed lines respectively.

accurately represent the data obtained from simulation. Similar observations are noted when using the potentials by Liu et al. [40] and Zope and Mishin [74] to simulate the thermal expansion of crystalline Al. When modeling and simulating crystalline Ti, the thermal expansion in the x , y , and z directions differ from one another because of its anisotropic hexagonal crystal structure. The changes in length are however still found to be smooth functions of temperature and are well represented by cubic polynomials.

Equation 3.9 is applied to the simulation data acquired from each interatomic potential to calculate the CTE of crystalline Al and Ti as a function of temperature. Results determined via MD simulation are then plotted and compared to one another as shown in Figure 3.5. Experimental CTEs of crystalline Al [70, 30] and Ti [59, 30] are also plotted as dashed lines to serve as references in determining which potential best predicts their thermal expansion. Figure 3.5 (a) plots the thermal expansion of Al predicted from MD simulations and compares the results to the two experimental sources. The simulated CTEs using the potentials by Liu et al. [40] and Zope and Mishin [74] both underestimate those given by experimental data, the former more so than the latter. On the other hand, the results obtained with the potential due to Mendeleev et al. [46] slightly overestimate the CTE of Al, but by a smaller margin. It is therefore determined that the interatomic potential by Mendeleev et al. [46] best replicates the thermal expansion of Al, and is selected as the potential of choice in the subsequent simulations. In Figure 3.5 (b), the CTEs of Ti obtained via MD simulations are compared to those from experiments.

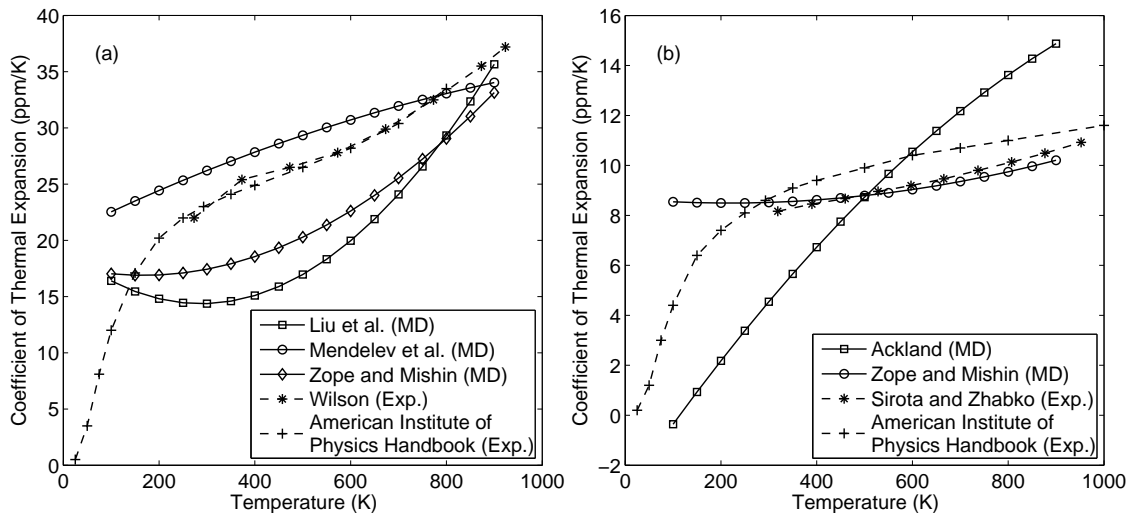


Figure 3.5: Simulated (solid lines) and experimental (dashed lines) CTEs plotted as a function of temperature for Al and Ti in figures (a) and (b) respectively.

From this plot it is seen that the potential by Zope and Mishin [74] produces results that closely match the experimental results by Sirota and Zhabko [59]. CTEs determined by Ackland [1] have the correct overall trend, however the differences between the empirical data are in general larger. The outcome from this simple study reveals that the interatomic potential by Zope and Mishin [74] gives the best correlation to experimental data, and is thus used to model Ti in the following simulations.

Thermal Expansion

Using the potentials by Mendeleev et al. [46] and Zope and Mishin [74] to define the atomic interactions for Al and Ti respectively, amorphous structures are created by rapidly quenching each material from its liquid state as other MD studies have done [52, 44]. Like before, 32,000 atoms in a $20 \times 20 \times 20$ unit cell array are simulated with periodic boundary conditions in all directions and a timestep of 1 fs is used. Under NPT dynamics, liquid Al and Ti are equilibrated at 1500 K and 2500 K respectively (well above their melting points) for 100 ps. After equilibration, the metallic liquids are cooled at a rate of 100 K/ps to a final temperature of 50 K. Rapid cooling of the liquid prevents the nucleation and formation of crystal structures, thus amorphous states are obtained. Immediately after cooling, the system is equilibrated further for 50 ps. Following equilibration of the quenched state, the potential energy of the system is minimized to remove any internal stress in the material created from the rapid cooling process [67]. Minimization is performed using a built-in function in LAMMPS that iteratively adjusts the atomic coordinates to minimize the potential energy using a conjugate gradient optimization algorithm. Since the atomic arrangements are sufficiently disordered, minimization does not create crystal structures and thus the energy of the system is driven to a local minimum. The resulting amorphous structure is verified by visualizing the atomic coordinates and examining the radial distribution function (RDF) of the system. After minimization, the amorphous states of Al and Ti are heated at a rate of 1 K/ps and ℓ_x , ℓ_y , and ℓ_z are recorded at regular intervals. During the entire process, the size of the simulation box is allowed to expand and contract anisotropically under zero external pressure. Using the same method as described previously, the CTEs of amorphous Al and Ti are calculated according to Equation 3.9. Due to the instability of amorphous structures and variability in phase space sampling, the results from 10 simulations are used to determine mean CTE values. The inputs into the 10 simulations are identical

except for the random number seed which is used to generate the initial velocities of the atoms under a Boltzmann distribution. For each of the 10 simulations, a random number seed is chosen between 1,000 and 100,000 using a random number generator.

Recrystallization

In examining the recrystallization behaviour of amorphous Al and Ti, the same inter-atomic potentials used in the study of thermal expansion are employed — the potentials by Mendeleev et al. [46] and Zope and Mishin [74] are used to model Al and Ti respectively. To obtain amorphous phases of Al and Ti, the same procedure as described before is used. Liquid Al and Ti is rapidly quenched at a rate of 100 K/ps to 50 K and subsequently equilibrated. Following equilibration, the potential energy of the system is minimized to remove unnatural atomic configurations. The temperature of the system is then increased at a rate of 1 K/ps under an isobaric-isothermal ensemble. During heating, the total potential energy and volume of the system is recorded as a function of temperature. When devitrification occurs, a sudden drop in potential energy will be noted at a particular temperature when the metastable amorphous phase transforms into a more energetically favourable crystalline state [44, 51]. The temperature at which an abrupt decrease in potential energy is observed is thus denoted as T_x . Similar trends will be noted with the volume versus temperature profiles of amorphous Al and Ti. During initial heating, the volume of the material will expand until T_x is reached. When devitrification occurs, a decrease in volume will be observed as the amorphous states transform into a more compact crystalline state. The amount of shrinkage due to recrystallization is therefore quantified by comparing the volume of the amorphous material at T_x to the volume of its crystalline counterpart at a higher temperature T_{x2} . The volume of crystalline material at T_{x2} is selected in order to emulate complete recrystallization over a long period of time. A volumetric expansion coefficient due to devitrification, β_r , is thus defined to describe the contraction in volume over the course of the phase transition:

$$\beta_r = \frac{1}{V_{a,x}} \frac{V_{c,x2} - V_{a,x}}{T_{x2} - T_x} \quad (3.10)$$

where $V_{a,x}$ is the volume of the amorphous material at T_x , and $V_{c,x2}$ is the volume of the crystalline material at T_{x2} . Equation 3.10 therefore gives a linear approximation of the change in volume between T_x and T_{x2} . A linear expansion coefficient due to recrystallization, α_r , can be related to β_r assuming the material has isotropic thermal

expansion. Considering a cube of material with volume V and side length ℓ , the volume after an increase in temperature, ΔT , is:

$$\begin{aligned} V + \Delta V &= (\ell + \Delta\ell)^3 \\ &= \ell^3 + 3\ell^2\Delta\ell + 3\ell\Delta\ell^2 + \Delta\ell^3 \end{aligned} \quad (3.11)$$

Substituting $\ell^3 = V$ and $\Delta\ell = \alpha_r\ell\Delta T$ into Equation 3.11 and rearranging gives:

$$0 = (3\alpha_r - \beta_r) + 3\alpha_r^2\Delta T + \alpha_r^3\Delta T^2 \quad (3.12)$$

Thus, given β_r and ΔT , α_r can be calculated by solving Equation 3.12. As before, the results from 10 simulations are averaged to obtain sufficient statistical sampling. Thus, mean values are obtained for T_x and $V_{a,x}$ for determining β_r and α_r .

Since the initial conditions and heating rates are identical for the exploration of thermal expansion and recrystallization, the same set of simulations are used for both analyses. In fact, the two investigations are related since the CTEs of amorphous Al and Ti are only determined up to T_x . Thus, T_x of amorphous Al and Ti determined from the study of recrystallization is required in the investigation of thermal expansion.

3.2.3 Results and Discussion

Amorphous States

The atomic structures of liquid Al and Ti cooled at a rate of 100 K/ps are visualized using VMD to confirm that amorphous materials have been obtained. Figure 3.6 illustrates the atomic configurations of Al and Ti in parts (a) and (b) respectively after quenching and

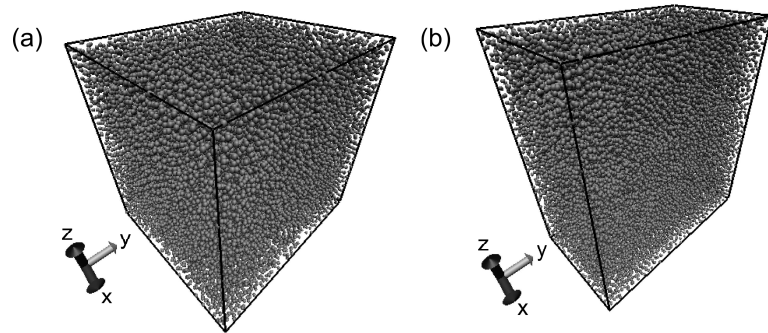


Figure 3.6: Atomic configurations of Al and Ti shown in figures (a) and (b) respectively. Edges of the periodic simulation cell are illustrated by the black lines.

minimization. For both elements, the atoms are in a disorder state with no crystalline structures visible. This is in contrast to Figure 3.3 where atoms are neatly arranged and crystal lattices are clearly observed. From these images it is clear that the quenched states of Al and Ti are non-crystalline. In addition to visualization, the RDFs of the amorphous materials are analyzed. The RDF, also known as $g(r)$, is commonly used to characterize atomic structures [51]. It measures from any given atom, the number of other atoms found at a distance r , normalized by the number of atoms that would be found in a uniformly distributed system. By this definition, $g(r)$ approaches 1 as r becomes large. Typical RDFs of amorphous Al and Ti at 300 K are shown in Figures 3.7 (a) and (b) respectively and compared to the RDFs of their crystalline states (shown in dashed lines). For a crystalline material, numerous sharp and well defined peaks are observed because the atoms sit and oscillate about their lattice positions. The locations of these peaks in the RDF represent the distances of the neighbouring atoms. With amorphous states, the peaks are broader and located at different values of r . The first peak of the RDF, which illustrates the distance of the nearest neighbour, is shifted to the left when compared to the crystalline phase. This phenomenon has been observed by Celik et al. [10] in their study of local structures in amorphous Al. Another characteristic of $g(r)$ for amorphous materials is the split second peak as seen in Figure 3.7. The second peak is much broader than the first, with two apexes observed. This double peak is a common characteristic and feature of amorphous materials and has been noted by other researchers [43]. Thus it is confirmed that amorphous Al and Ti have been successfully created by the quenching process.

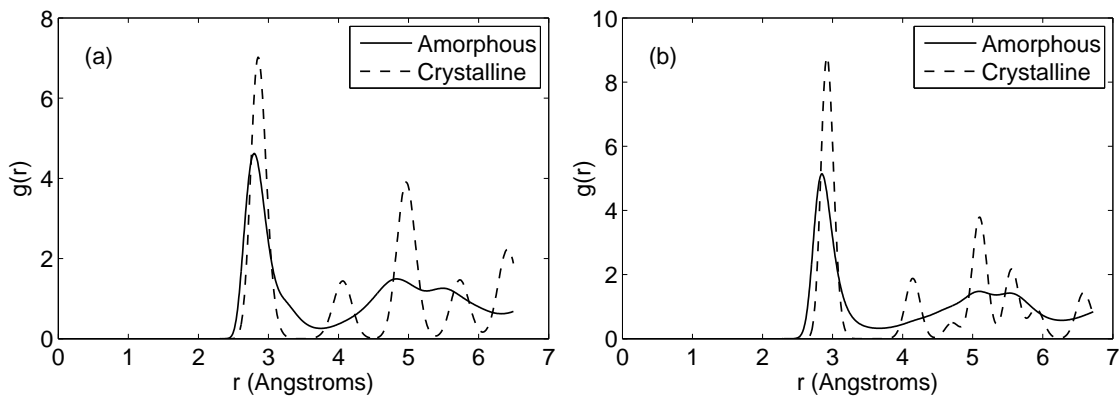


Figure 3.7: RDFs of amorphous and crystalline states of Al and Ti at 300 K are shown in figures (a) and (b) respectively.

Thermal Expansion

Following the methodology described in Section 3.2.2, the CTEs of amorphous Al and Ti are calculated from the change in ℓ_x , ℓ_y , and ℓ_z as the system is heated. The variation in ℓ_i as a function of T in a typical simulation of amorphous Al is illustrated in Figure 3.8. Raw data from simulation are represented by the thin lines, while the cubic polynomial interpolants are plotted by bold lines. Information up until the temperature of recrystallization is used for fitting since only the CTE of the amorphous states are of interest. Using the entire set of data would also result in a poor fit due to the abrupt changes in size caused by the transition in phase. Prior to recrystallization, it is observed from Figure 3.8 that ℓ_i does not vary smoothly as the temperature increases. This is in contrast to the results in Figure 3.4 which show smooth changes for crystalline Al. Pressure fluctuations are inherent to MD simulations due to the use of statistical ensembles to control macroscopic quantities. The variation in simulation size is thus a manifestation of the fluctuations in pressure, compounded by the fact that amorphous materials are metastable. When amorphous Al is heated from 50 K, the system is in general found to increase in the x , y , and z directions. Above a certain temperature however, a sudden overall decrease in the simulation size is observed. This phenomenon is a consequence of amorphous Al transitioning into a denser crystalline state. Once the amorphous phase has completely crystallized, the thermal expansion resumes that of a crystalline material. It can be seen in Figure 3.8 that past 600 K, the lengths of the simulation box grow steadily with increasing temperature. Although not shown here, the simulation of amorphous Ti reveals similar characteristics and patterns in the data as described here

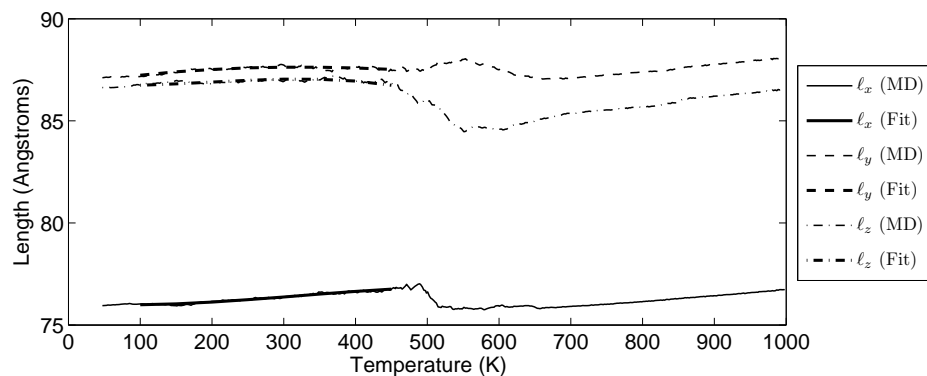


Figure 3.8: Variation in simulation cell size as amorphous Al is heated from an initial temperature of 50 K at a rate of 1 K/ps.

for Al.

In this study, the CTEs of amorphous Al and Ti are calculated between 100 K and T_x at 50 K intervals. For Al and Ti, T_x has been established to be roughly 450 K and 550 K respectively — details in determining their recrystallization temperatures are given later in this section. Using Equation 3.9, the CTE at a given temperature is calculated and then averaged over the 10 simulations to obtain the results plotted in Figures 3.9 and 3.10 for Al and Ti respectively. The variation in CTEs obtained from MD simulation is shown by error bars about the mean values, illustrating plus and minus one standard deviation. CTEs of crystalline Al and Ti from literature and MD simulations in this work are also plotted for reference and comparison.

Figure 3.9 illustrates the CTEs of amorphous and crystalline Al. Experimental data for the thermal expansion of crystalline Al are taken from the study by Wilson [70] and the American Institute of Physics Handbook [30]. The two experimental sources give results that are in very close agreement with each other. No studies have been found that give the CTE of amorphous Al. From this work, the computer simulated thermal expansion of crystalline Al produces results that are in accordance with experimental data. The trend of increasing thermal expansion with temperature is correctly reproduced by the interatomic potential, and the predicted CTEs are slightly higher than those reported from experiment. A difference of approximately 3 ppm/K at room temperature is observed, which decreases with higher temperature. This deviation is minimal in comparison to a previous MD study by Alper and Politzer [3] which overestimates the

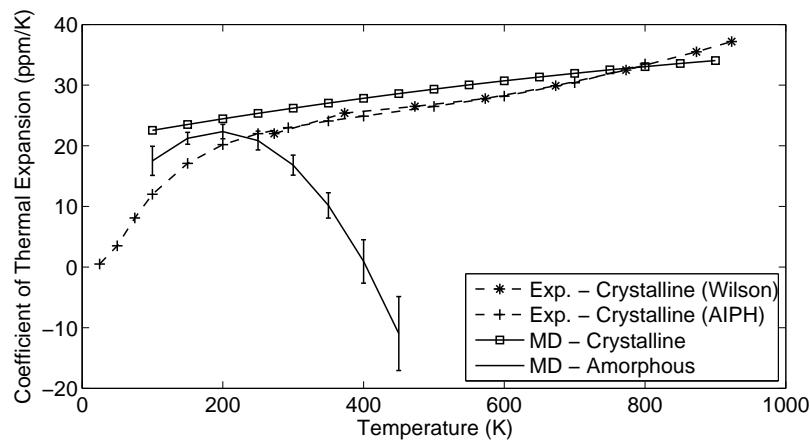


Figure 3.9: CTE of amorphous Al plotted as a function of temperature. Crystalline CTEs from simulation and literature are also shown for comparison.

thermal expansion of crystalline Al by factors of 1.5–2.0. The disparity between MD and experimental results is explained by the limited description provided by empirical interatomic potentials. A comparison between the thermal expansion of amorphous and crystalline Al derived from MD simulations reveals a number of different features. From Figure 3.9, it is apparent that for both phases of Al, the CTEs are similar at temperatures below 250 K — the CTE of amorphous Al is however a few ppm/K lower. At temperatures above 250 K, the predicted thermal behaviour between amorphous and crystalline Al are very different. For crystalline Al, the CTE shows an increasing trend with higher temperatures, while in the case of amorphous Al, the CTE drops off rapidly. At 300 K, the CTE of amorphous Al is approximately 10 ppm/K lower than that of crystalline Al, and decreases to -10 ppm/K at 450 K. This decrease in thermal expansion is attributed to thermally activated recrystallization in which the amorphous atomic structure transforms into a more favourable and denser crystalline state. Since each simulation begins with varying initial atomic velocities, the trajectories of the system will differ. The variation between simulations is illustrated by the error bars representing plus and minus one standard deviation of the ten CTEs calculated at each temperature. In general, there is more spread in the simulated results at higher temperatures. At 350 K and below, the standard deviation is approximately 1.0–2.4 ppm/K. For 400 K and higher, the standard deviation grows significantly as simulations produce drastically different results. The increased variability at high temperatures can be explained by the unstable manner in which amorphous Al transitions to a crystalline phase. Furthermore, pressure fluctuations inherent to MD simulations are found to create prominent volume fluctuations in the system, particularly near T_x because of the metastable amorphous state of Al. These factors affect the polynomial fitting of simulation data, which causes variations in α since it is sensitive to the slopes of the cubic interpolant. As a result, large variations in the predicted CTE near T_x are observed.

The CTE of Ti in both crystalline and amorphous states are illustrated and contrasted in Figure 3.10. Two sources in the literature have been found that give the experimental CTE of crystalline Ti as a function of temperature, those from a study by Sirota and Zhabko [59] and the American Institute of Physics Handbook [30]. Once again, no studies have been found which investigate and quantify the thermal expansion of amorphous Ti. The two experimental sets of data show good agreement with one another. Both sources give similar CTEs and an increasing trend with higher temperature. Sirota and Zhabko [59] reports values that are slightly lower than those from the American Institute

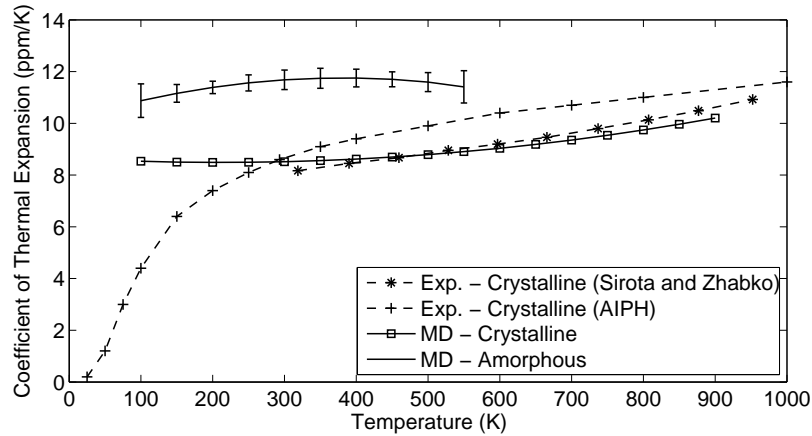


Figure 3.10: CTE of amorphous Ti plotted as a function of temperature. Crystalline CTEs from simulation and literature are also shown for comparison.

of Physics Handbook, but the differences are no greater than 1.2 ppm/K. Using the potential by Zope and Mishin [74], the thermal expansion of crystalline Ti shows excellent conformance with both experimental sources as seen in Figure 3.10. Results are very close to the experimental CTEs given by Sirota and Zhabko [59], but are slightly lower than those from the American Institute of Physics Handbook [30]. The disagreement between the simulated and experimental CTEs is once again attributed to the limited accuracy of the interatomic potential. Comparing MD results between amorphous and crystalline Ti reveals that the CTE of amorphous Ti is consistently higher than that of its crystalline state. Differences between 2.3–3.2 ppm/K over the simulated temperature range of 100–550 K are observed. The CTE of amorphous Ti remains more or less steady as the temperature approaches T_x , unlike amorphous Al where a sudden decrease in thermal expansion is observed. The difference in behaviour can be explained by comparing the volumes of Al and Ti in both their amorphous and crystalline states. At 300 K, the atomic volumes of amorphous and crystalline Al are 18.18 and 16.73 Å³/atom respectively, corresponding to a negative 8% change in volume. This value is comparable to the 9% predicted by Becquart et al. [4]. Amorphous and crystalline Ti have atomic volumes of 17.83 and 17.80 Å³/atom respectively, a difference that is extremely small. A large discrepancy in atomic volume, and therefore density, is found between the two phases of Al. This disparity is minimal when comparing the two states of Ti. Thus as amorphous Ti recrystallizes, the decrease in volume is much smaller when contrasted with the phase transition of Al. This is evident from Figure 3.11 which illustrates the atomic volume

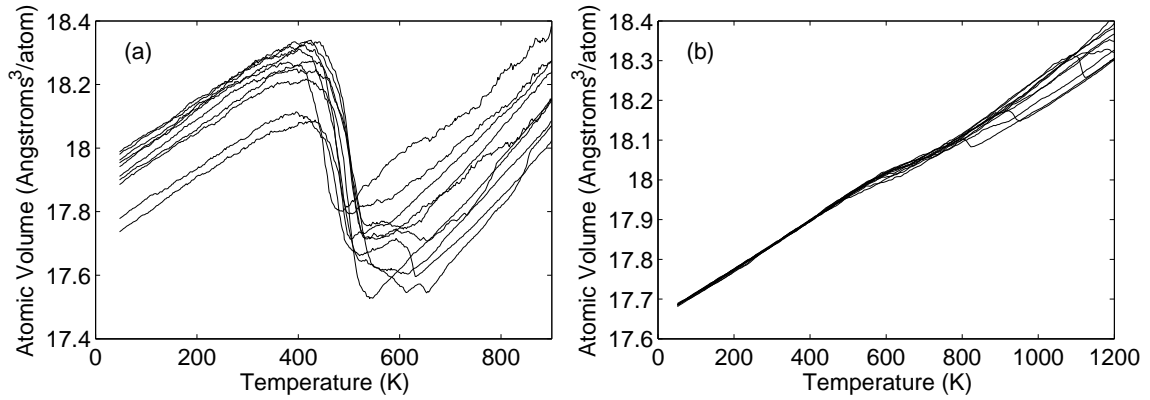


Figure 3.11: Atomic volume versus temperature profiles of amorphous (a) Al and (b) Ti during recrystallization. Each line represents one of the ten simulations performed.

versus temperature profiles of amorphous Al and Ti during recrystallization. In the case of Al, a negative change of roughly $0.6 \text{ \AA}^3/\text{atom}$ is observed, while very slight differences are noted for Ti. Furthermore, the MD simulations show that the process of devitrification for Ti takes place gradually over a greater temperature range and is less abrupt than that of Al. As a result of these two factors, the thermal expansion of amorphous Ti does not exhibit an extreme and sudden decline near T_x . Another consequence of the gentle amorphous to crystalline transition is noted in the variation between simulations as illustrated by the error bars in Figure 3.10. For amorphous Ti, the standard deviation in CTE ranges between 0.2–0.7 ppm/K, much lower than that of amorphous Al. The variability in results are also more or less constant throughout the simulated temperature range and do not increase as temperatures approach T_x , unlike the behaviour noted for amorphous Al.

Recrystallization

The devitrification of amorphous Al and Ti is first confirmed by examining the evolution of their RDFs and via visualization. Figure 3.12 shows the RDF of Al at 300 K and 800 K (before and after recrystallization), and a visual snapshot of the atoms at 800 K. The RDF at 300 K clearly shows an amorphous structure as noted by the split second peak. At 800 K, the profile has changed significantly with the appearance of new peaks indicating a crystalline atomic structure. Figure 3.12 (b) illustrates the atomic coordinates of Al at 800 K rendered via VMD. The snapshot reveals that the atoms are neatly arranged in crystalline structures. From this evidence it is therefore confirmed that Al,

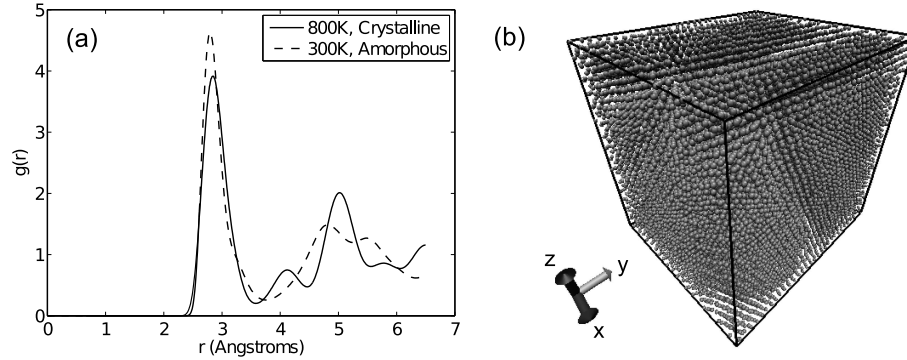


Figure 3.12: RDFs of Al simulation at 300 K and 800 K shown in figure (a). Figure (b) illustrates the atomic coordinates of Al at 800 K.

beginning from an amorphous state, has recrystallized once sufficiently high temperatures are reached. Although not shown, similar observations are found for Ti. To pinpoint the phase transition temperatures of Al and Ti, their potential energy versus temperature profiles as shown in Figure 3.13 are analyzed.

Figure 3.13 (a) illustrates how the potential energy of amorphous Al varies as a function of temperature. Each solid line represents the data obtained from one of the ten simulations. As the system is heated from 50 K, the potential energy grows at a roughly linear rate until the point of recrystallization, where the potential energy suddenly falls with increasing temperature. This abrupt drop is observed because the metastable amorphous structure transforms into a more energetically favourable crystalline state that is of lower potential energy. In most instances, the potential energy is found to decrease in multiple steps and in a discontinuous fashion. This behaviour is attributed to the sudden nucleation and growth of the crystalline phases and the formation of multiple grains in the system. Grain boundaries introduce additional energy to the system because the bonds in this region are stretched and the atoms are in a suboptimal state [8]. Further heating eliminates these boundaries to create larger grains, thus the potential energy continues to decrease with higher temperatures. Since the recrystallization process varies for each simulation, the final potential energy after the amorphous to crystalline phase transition is not necessarily the same and is found to differ slightly. After amorphous Al has recrystallized, the potential energy once again resumes an approximately linear increase with temperature. Using the curves in Figure 3.13 (a), T_x is estimated for the ten simulations. The average value of T_x for amorphous Al is therefore calculated to be 453.4 K with a standard deviation of 22.7 K and is illustrated by the vertical dashed

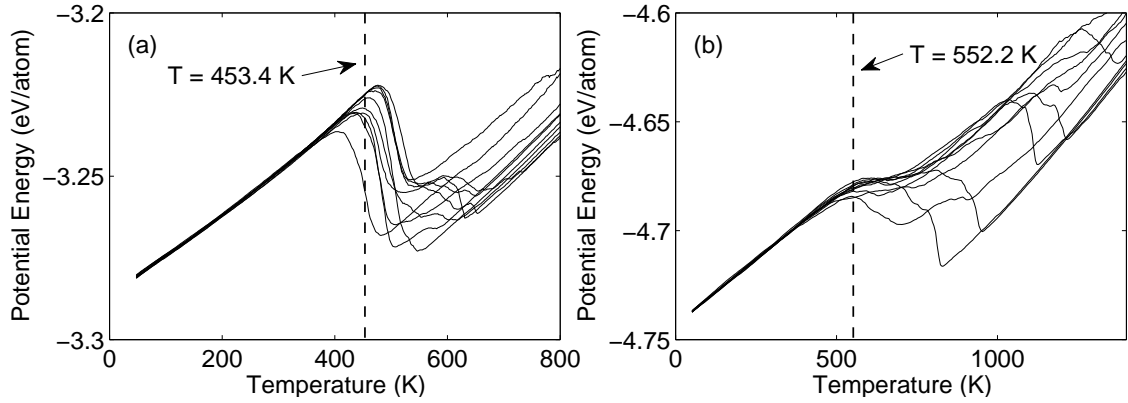


Figure 3.13: Potential energy of amorphous (a) Al and (b) Ti plotted as a function of temperature. Results from all ten simulations are shown and the average recrystallization temperature is illustrated by the dashed vertical line.

line. Considerable variability in T_x is noted between the ten simulations as seen in Figure 3.13 (a). As explained before, this is due to the variation of MD simulations within the statistical ensemble and the metastable amorphous phase of Al. The predicted T_x for amorphous Al from this work is compared to the results by Lu and Szpunar [44] and Shimono and Onodera [57] which give T_x to be 550–630 K and 230 K respectively. The estimated recrystallization temperature from this work is found to differ from the previous investigations, but is closer to the range given by Lu and Szpunar [44] being approximately 100 K lower.

Figure 3.13 (b) plots the potential energy of amorphous Ti as a function of temperature. Similar to the behaviour of Al, an approximately linear correlation between the potential energy and temperature is observed during initial heating. As temperatures approach T_x , subtle changes in potential energy are observed. Unlike Al, the potential energy of the Ti system does not exhibit extreme and abrupt decreases during devitrification. In general, a small dip in potential energy is found to occur at T_x , followed by a large and sudden decrease at elevated temperatures. This behaviour can be explained by the fact that amorphous Ti tends to crystallize into many small grains as seen through visualization of the atomic coordinates. Figure 3.14 illustrates a slice of the simulation cell at 800 K where numerous groups of crystalline atomic structures are visible, each with different directionalities. The cluster of atoms belonging to one specific orientation represents a grain. As explained previously, grain boundaries are non-ideal atomic configurations which add potential energy to the system. As the temperature of the system

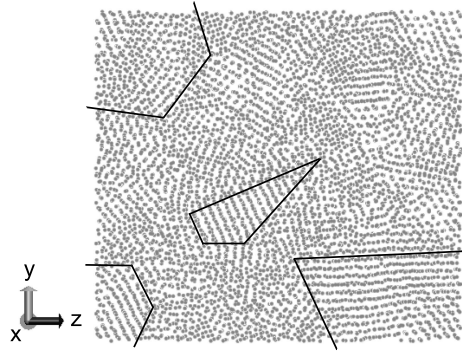


Figure 3.14: Slice of Ti simulation box at 800 K revealing multiple grains. Examples of grain boundaries are identified by the black lines.

is increased, the grain boundaries are eliminated to form larger grains, thus explaining the drop in potential energy observed at temperatures above T_x . Grain growth is found to initiate at different temperatures due to the variation between MD simulations. After amorphous Ti has recrystallized, the potential energy once again resumes a linear increase with temperature, similar to the trend observed with Al. Using the same method as before, the recrystallization temperature is estimated for the ten simulations using the potential energy profiles in Figure 3.13 (b). The average T_x for amorphous Ti is thus determined to be 552.2 K with a standard deviation of 28.1 K and is indicated in Figure 3.13 (b) by the vertical dashed line. Compared to T_x for amorphous Al derived from this work, it is approximately 100 K higher, while the standard deviation is of similar magnitude. The disparity between simulations is once again attributed to the variation from statistical sampling. MD simulations by Shimono and Onodera [57] predict T_x to be approximately 280 K for Ti, much lower than the value obtained from this research. However, both investigations predict T_x of Ti to be greater than that of Al. This trend is in accordance with intuition because the cohesive energy of Ti is higher than Al, thus more energy (higher temperature) is required to break the atomic bonds.

Via Equations 3.10 and 3.12, α_r for Al and Ti are determined using the volume versus temperature data from simulation. Figure 3.15 shows the average atomic volume profiles of amorphous Al and Ti with the volumes of crystalline Al and Ti illustrated for comparison. It is found that even after recrystallization has occurred, the volume of the system does not reach that of a perfectly crystalline state and is slightly elevated. As noted earlier, recrystallization from an amorphous state tends to create multiple grains and numerous defects which creates distortions in the lattice and affects the density of

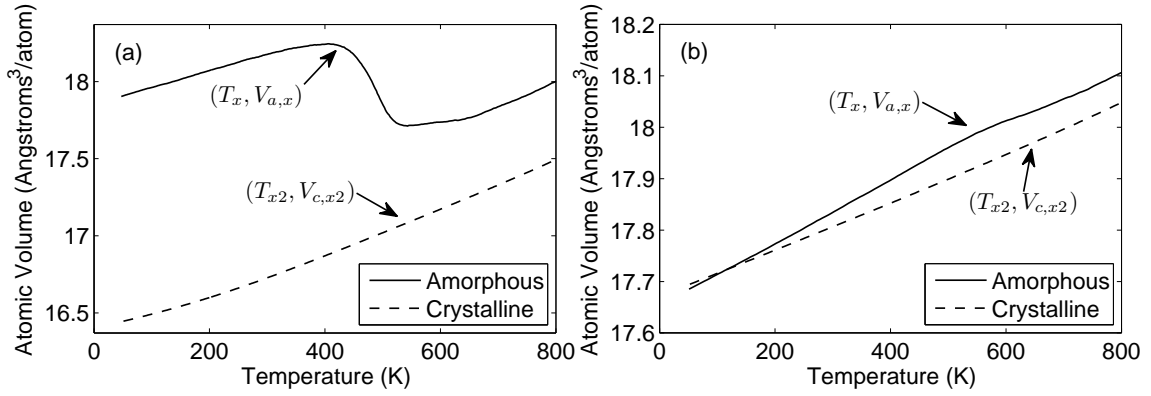


Figure 3.15: Mean atomic volume versus temperature profiles of amorphous and crystalline (a) Al and (b) Ti. Data points used to calculate β_r are identified.

the material. From the previous analysis, T_x was determined to be roughly 450 K and 550 K for Al and Ti respectively. Using this information, $V_{a,x}$ is extracted from the amorphous volume curves as depicted in Figure 3.15. From these profiles, it is estimated that the process of recrystallization occurs over a temperature range of 100 K, thus T_{x2} is selected to be equal to $T_x + 100$ K for both Al and Ti. With the knowledge of T_{x2} , $V_{c,x2}$ is determined from the crystalline volume curves as shown in Figure 3.15. Table 3.1 summarizes the values identified from the procedure described above which are used to calculate β_r for Al and Ti. Substituting the corresponding numbers into Equation 3.10 gives β_r to be $-5.94 \times 10^{-4} \text{ K}^{-1}$ and $-1.00 \times 10^{-5} \text{ K}^{-1}$ for Al and Ti respectively. The values of β_r are then used in Equation 3.12 to solve for the linear expansion coefficient due to recrystallization given $\Delta T = 100$ K. Using the `fsolve` function in MATLAB [32], the non-linear expression is solved to give α_r equal to $-2.02 \times 10^{-4} \text{ K}^{-1}$ and $-3.34 \times 10^{-6} \text{ K}^{-1}$ for Al and Ti respectively. Given the extreme change in volume during the transition between amorphous and crystalline Al, a large negative linear expansion coefficient due to recrystallization is computed for Al. The opposite is noted for Ti where a modest negative value of α_r is calculated because of the small transformation in volume during devitrification.

Table 3.1: Temperatures and atomic volumes for calculating β_r for Al and Ti.

Material	T_x (K)	$V_{a,x}$ (\AA^3)	T_{x2} (K)	$V_{c,x2}$ (\AA^3)
Aluminum	450	18.175	550	17.095
Titanium	550	17.989	650	17.971

Chapter 4

Mechanical Properties of Al and Ti Thin Films

The mechanical properties of Al and Ti thin films are examined via experimental nanoindentation and FE simulations in this chapter. Methods for determining the Young's modulus and plastic properties of materials from nanoindentation load-displacement curves are reviewed in Section 4.1. In Section 4.2, the experimental procedure for conducting nanoindentation on thin Al and Ti films is given, and the analysis of experimental data is described. The resulting elastic and plastic properties of the films are also discussed.

4.1 Identifying Material Properties via Nanoindentation

Nanoindentation tests are commonly used to derive the mechanical properties of small scale materials, such as thin films, where traditional tension or compression methods cannot be used. Typically, a sharp tip is used to indent the surface of a material while the applied force and indentation depth is measured. From the load-displacement curve, the elastic modulus and plastic properties of the material can be determined using the methods outlined in Sections 4.1.1 and 4.1.2.

4.1.1 Young's Modulus

The Oliver and Pharr [50] model is widely used to analyze nanoindentation data to determine the elastic modulus of small scale materials and is an improvement on the

procedure proposed by Doerner and Nix [18]. During a nanoindentation experiment, an indenter tip is penetrated into the material of interest while the applied load and displacement is continuously measured. Typical curves resulting from such experiments are illustrated in Figure 4.1 with the important features and quantities identified. Given the load-displacement data, the Young's modulus is calculated using the maximum load P_{\max} , maximum indentation depth h_{\max} , and the contact stiffness $S = (dP/dh) |_{h_{\max}}$. The underlying assumption of the Oliver and Pharr [50] model is that the contact between the indenter and material is purely elastic during unloading, and that the unloading curve can be written in the general form:

$$P = \alpha (h - h_f)^m \quad (4.1)$$

where P is the applied force, h is the elastic displacement, h_f is the final displacement after unloading, with α and m constants. By assuming the unloading curve follows a power law, the Oliver and Pharr [50] model differs from the method proposed by Doerner and Nix [18], which takes the unloading curve to be linear. The contact stiffness is therefore determined by evaluating the derivative of Equation 4.1 at h_{\max} .

Using Sneddon's solution for contact between a flat cylindrical indenter and an elastic half space [60], it can be shown that the contact stiffness is related to the reduced elastic modulus E_r , and projected contact area A , through the following equation:

$$S = \frac{2}{\sqrt{\pi}} E_r \sqrt{A} \quad (4.2)$$

A reduced Young's modulus is defined to account for deformations arising from the non-rigid indenter. E_r is thus a function of the mechanical properties of the specimen and

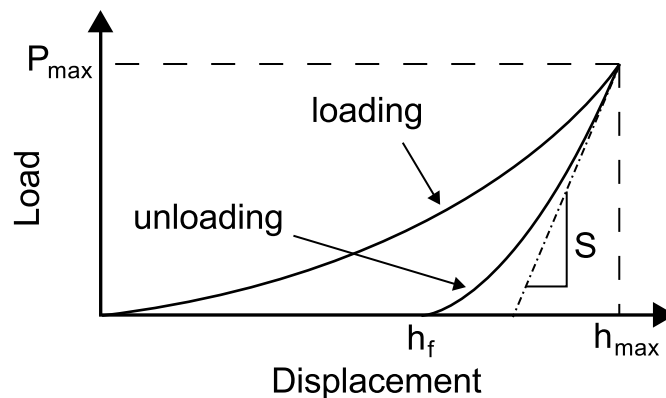


Figure 4.1: Schematic of nanoindentation load-displacement curves with key features identified.

indenter and is given by:

$$\frac{1}{E_r} = \frac{1 - \nu^2}{E} + \frac{1 - \nu_i^2}{E_i} \quad (4.3)$$

where E and ν are the Young's modulus and Poisson's ratio of the material of interest, and E_i and ν_i are those of the indenter. Although Equation 4.2 is derived under the assumption of a flat punch indenter, it has been shown by Pharr et al. [53] that it is equally applicable for indenters described by the revolution of a smooth function. Another assumption made by Oliver and Pharr [50] is that Equation 4.2 can be applied to surfaces that are not flat. Since the material is plastically deformed during the loading stage, there exists a residual impression in the surface upon unloading. Justification for this assumption is provided through empirical observations [50] and a mathematical analysis which reveals the load-displacement relationships for an indented or flat surface are the same if geometric parameters are redefined [53]. By rearranging Equation 4.2, E_r can be written in terms of the contact stiffness and the area of contact. With S known from the initial slope of the unloading curve, E_r can thus be found by determining A . Given the reduced modulus, the Young's modulus of the specimen is deduced by substituting the known mechanical properties of the indenter into Equation 4.3, and assuming a Poisson's ratio for the material of interest. It has been found that the result of the indentation analysis is insensitive to ν , thus a precise value of the Poisson's ratio of the material is not required to accurately determine E [18, 73].

In the procedure developed by Oliver and Pharr [50], a three-sided pyramid known as a Berkovich tip is used in the nanoindentation experiments. Figure 4.2 provides an illustration of how the indenter tip penetrates into the surface of a material. It can be seen that the total measured displacement is given by:

$$h = h_c + h_s$$

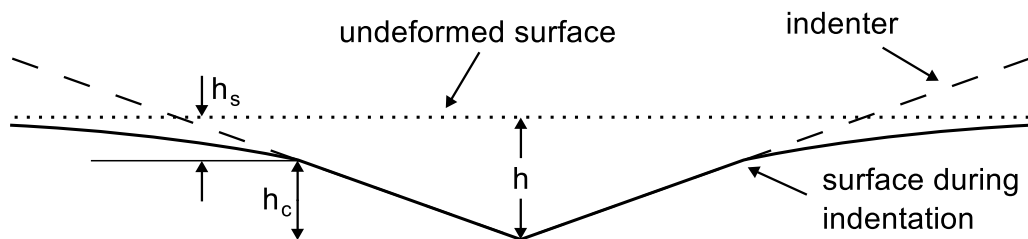


Figure 4.2: Cross section of indenter and material surface during nanoindentation process. The total displacement, h , is comprised of the depth of contact and the surface displacement represented by h_c and h_s respectively.

where h_c is the depth of contact, and h_s is the displacement of the surface perimeter. From Figure 4.2, it is evident that A is dependent on h_c and the geometry of the indenter. A function which relates the cross-sectional area to the distance from the tip can be determined for a given indenter such that:

$$A = F(h_c) \quad (4.4)$$

Assuming small deformations in the indenter itself, A is calculated using Equation 4.4 and the contact depth at maximum load:

$$h_c = h_{\max} - h_s \quad (4.5)$$

h_{\max} is readily available from the nanoindentation data, while h_s can be determined using Sneddon's solution for the shape of the deformed surface [60]. The result of Sneddon's analysis thus gives:

$$h_s = \epsilon \frac{P_{\max}}{S} \quad (4.6)$$

where ϵ is a constant whose value depends on the geometry of the indenter. For a conical indenter, ϵ has a value of 0.72, while for a paraboloid of revolution and flat punch, $\epsilon = 0.75$ and 1 respectively. To determine which value of ϵ is most suitable for a Berkovich indenter, Oliver and Pharr [50] analyzed the unloading curves of various materials. From Sneddon's analysis, it has been shown that the geometry of the indenter is correlated to the exponent m in Equation 4.1 as summarized in Table 4.1. The experimental nanoindentation curves obtained by Oliver and Pharr [50] show that m has a mean value of 1.4, thus it is determined that the Berkovich indenter is best described by a paraboloid geometry. Consequently, $\epsilon = 0.75$ is used in Equation 4.6 for calculating h_s . A paraboloid indenter, rather than a conical indenter, better simulates a sharp pyramidal Berkovich indenter due to the concept of an effective indenter shape [49]. The point of contact is not sharp and singular due to the fact that the indenter is pressed into a residual impression formed from plastic deformation during loading. Furthermore,

Table 4.1: Indenter shape and associated constants from Sneddon's analyses.

Geometry	ϵ	m
Flat punch	1	1
Paraboloid	0.75	1.5
Conical	0.72	2

elastic recovery during unloading creates a convex curvature on the surface and as a result, the pressure distribution about the tip is better predicted by a parabolic shape. Thus, utilizing Equations 4.1–4.6, the elastic modulus of a material can be determined from the load-displacement data obtained from nanoindentation experiments.

4.1.2 Plastic Properties

Characterizing the plastic properties of thin films via conventional methods, such as micro tensile, bulge, or cantilever beam deflection tests, requires careful micromachining to separate the film from the substrate while preserving the integrity of the film [73]. Researchers have therefore developed techniques where the elastic-plastic properties of thin films can be determined via nanoindentation experiments and finite element modeling with the substrate intact [73, 37]. In fact, the substrate plays a crucial role in determining unique material properties. In this work, the method developed by Zhao et al. [73] is used to extract the plastic properties of Al and Ti thin films, thus the concepts and procedures are briefly summarized and explained.

In traditional nanoindentation experiments, such as the Oliver and Pharr [50] method, the maximum depth of penetration must be less than 10% of the film thickness to avoid the influence of substrate effects [66]. The approach by Zhao et al. [73], however, utilizes deeper indentations to extract the mechanical properties of thin films. Cheng and Cheng [13] has shown, using dimensionless functions, that stress-strain relationships cannot be determined uniquely using only the loading and unloading curves from conical or pyramidal indenters. Thus it is possible for two materials with distinct mechanical properties to share the same load-displacement curves. Zhao et al. [73] proposes a method in which deep nanoindentation is used to take advantage of the substrate effect. During large penetration depths, the substrate stiffness introduces a new factor which affects the shape of the loading and unloading curves [72]. Materials that would otherwise have indistinguishable nanoindentation curves would thus give distinct profiles as the interaction with the substrate differs.

Shape Factors

The loading and unloading curves from deep nanoindentation are parameterized by non-dimensional factors and mapped to material and substrate properties. A typical nanoindentation load-displacement curve is illustrated in Figure 4.3 with the important pa-

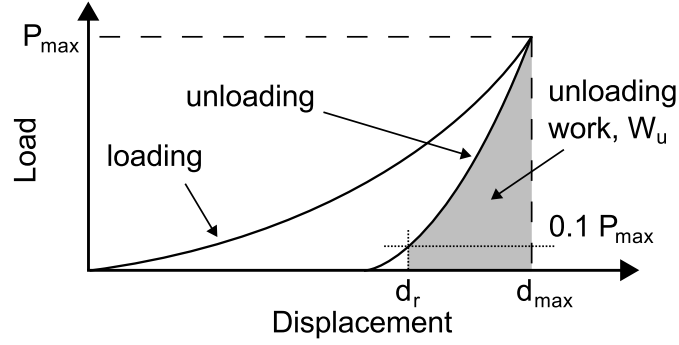


Figure 4.3: Schematic diagram of nanoindentation load-displacement curve with important parameters relevant to the analysis by Zhao et al. [73] labeled.

parameters required in the analysis identified. A reduced residual penetration depth d_r is defined when $P = 0.1P_{\max}$ to avoid errors in determining the true residual displacement [73]. The unloading work W_u is defined as the area under the unloading curve between d_r and d_{\max} as illustrated by the area in grey. To determine the shape factors and non-dimensionalize the nanoindentation curves, it is first assumed that the stress-strain curve of the film can be expressed by a power law of the form:

$$\sigma = \begin{cases} E_f \epsilon & \text{for } \epsilon \leq \sigma_f / E_f \\ R_f \epsilon^{n_f} & \text{for } \epsilon \geq \sigma_f / E_f \end{cases} \quad (4.7)$$

where E_f , σ_f , and n_f are the Young's modulus, yield stress, and work hardening exponent of the film, and $R_f \equiv \sigma_f (E_f / \sigma_f)^{n_f}$ to ensure continuity. Thus, the set of three quantities (E_f, σ_f, n_f) is sufficient to describe the elastoplastic properties of the film.

Using dimensional analysis, the following independent dimensionless functions can be constructed to parameterize the loading and unloading curves [73]:

$$\frac{P}{\sigma_f d^2} = \Phi \left(\frac{E_f}{E_s}, \frac{E_f}{\sigma_f}, n_f, \frac{d}{h} \right) \quad (4.8)$$

$$\frac{W_u}{E_f (d - d_r)^3} = \Omega \left(\frac{E_f}{E_s}, \frac{E_f}{\sigma_f}, n_f, \frac{d}{h} \right) \quad (4.9)$$

where Φ and Ω are non-dimensional functions, E_s is the Young's modulus of the substrate, P is the applied load, d is the penetration depth, and h is the thickness of the film. By performing two indentations at different depths, $d_1 = h/3$ and $d_2 = 2h/3$, four independent equations are obtained to determine the elastoplastic properties of the thin film. Penetration depths of one and two-thirds the thickness of the film are chosen such that the substrate effect is profound and distinct, but not too deep to cause delamination

of the film [73]. Since only three parameters are required to describe the mechanical properties of the material, only three independent equations are needed to obtain a unique solution. Thus, one penetration to a depth of two-thirds the film thickness is sufficient to compute the material properties since the applied load at d_1 and d_2 , P_1 and P_2 , can be measured on the same loading curve. Equation 4.9 for $d/h = 1/3$ provides redundant information and is therefore discarded. The following three non-dimensional functions are therefore obtained and correlated to the material and substrate properties:

$$\ln \left(\frac{P_1}{\sigma_f d_1^2} \right) = f_1(\xi, \eta, n_f) \quad (4.10)$$

$$\ln \left(\frac{P_2}{\sigma_f d_2^2} \right) = f_2(\xi, \eta, n_f) \quad (4.11)$$

$$\ln \left(\frac{W_{u2}}{E_f (d_2 - d_{r2})^3} \right) = h_2(\xi, \eta, n_f) \quad (4.12)$$

where $\xi \equiv \ln(E_f/E_s)$ and $\eta \equiv \ln(E_f/\sigma_f)$. For an indentation to a maximum depth of d_2 , the reduced residual displacement is d_{r2} , and the associated unloading work is W_{u2} .

Forward Analysis

The functions f_1 , f_2 , and h_2 in Equations 4.10–4.12 have been determined by Zhao et al. [73] using a series of FE simulations to map the shape factors to the dimensionless variables. In their simulations, an axisymmetric model is created using ABAQUS with the substrate width and height 100 times larger than the thickness of the film. The film is elastoplastic as described by Equation 4.7, and the substrate is assumed to behave elastically. Both the film and substrate are also taken to behave isotropically. The Berkovich indenter is modeled as a rigid conical surface with a half apex angle of 70.3° such that the same area function is retained. Loading and unloading curves obtained via pyramidal and conical indenters having the same area function have been shown to be almost identical [73]. In the simulations by Zhao et al. [73], a Poisson's ratio of 0.3 is taken for both the film and substrate, and Coulomb friction is assumed with a friction coefficient of 0.15. The influence of friction on the results are minimal, as a FE study showed little change in the loading and unloading curves as the coefficient of friction was varied between 0–0.4 [41]. The parameter E_f/σ_f is varied between 10 to 4000, n_f between 0 and 0.6, and E_f/E_s from 1/8 to 8. These ranges encompass commonly encountered materials and film-substrate pairings [73]. FE simulations are conducted for all combinations of parameters and the shape factors of the resulting nanoindentation

curves are determined. Thus, fitting the FE results to the input material and substrate properties gives f_1 , f_2 , and h_2 . The forms of these functions are not shown here for brevity, but can be found in the appendix of the paper by Zhao et al. [73].

Reverse Analysis

To extract the mechanical properties of the film, the elastic modulus of the substrate must first be known. This information may be found in literature or measured experimentally via the Oliver and Pharr [50] method. With E_s known, a deep indentation is performed using a Berkovich tip such that $d_{\max} = d_2 = 2h/3$. d_1 is equal to $1/3h$ by definition and the parameters P_1 , P_2 , d_{r2} and W_{u2} are determined from the experimental load-displacement curve. A total error function, e , is defined as follows:

$$\begin{aligned}
 e = & \left| \left(\ln \left\{ \frac{P_1}{\sigma_f d_1^2} \right\} - f_1(\xi, \eta, n_f) \right) / \ln \left(\frac{P_1}{\sigma_f d_1^2} \right) \right| \\
 & + \left| \left(\ln \left\{ \frac{P_2}{\sigma_f d_2^2} \right\} - f_2(\xi, \eta, n_f) \right) / \ln \left(\frac{P_2}{\sigma_f d_2^2} \right) \right| \\
 & + \left| \left(\ln \left\{ \frac{W_{u2}}{E_f (d_2 - d_{r2})^3} \right\} - h_2(\xi, \eta, n_f) \right) / \ln \left(\frac{W_{u2}}{E_f (d_2 - d_{r2})^3} \right) \right|
 \end{aligned} \tag{4.13}$$

The values of E_f , σ_f , and n_f that minimize Equation 4.13 are therefore the material properties of the film.

4.2 Elastic-Plastic Properties of Al and Ti Thin Films

4.2.1 Experimental Method and Analysis

The objective of this study is to characterize the mechanical properties of Al and Ti thin films in order to accurately model and understand the properties of the bi-material lattice. The microstructure of the films may deviate from that of their bulk form due to the manufacturing process, thus altering their mechanical properties. Using nanoindentation experiments, the elastic-plastic stress-strain curves of Al and Ti films are extracted using the methods described in the previous section. The experimental method and procedure for analyzing the results are described here.

A combination of both methodologies by Oliver and Pharr [50] and Zhao et al. [73] are used to determine the elastic-plastic properties of the thin films. To this end, two types of nanoindentation experiments must be performed: (i) shallow, and (ii) deep indentations.

All nanoindentation experiments are conducted with a MTS Nanoindenter G200 system at the California Institute of Technology. Thermal drift due to temperature variations is automatically calculated and accounted for by the machine. The Al and Ti films are created via e-beam deposition to a nominal thickness of $1\ \mu\text{m}$ and the thicknesses of the films are confirmed via a profilometer. For the shallow indentation experiments, a set of 10 penetrations to a maximum depth of 100 nm (10 % of the film thickness) are performed for each material with a Berkovich indenter to obtain a series of loading and unloading curves. The set of indentations are performed at different locations spaced 1 mm apart to provide sufficient sampling of the film. For each indentation, the sample is penetrated at a constant strain rate of $0.025\ \text{s}^{-1}$. Once the maximum penetration depth is reached, the applied load is held for a period of 10.48 s before unloading begins. From each data set, the Young's modulus is calculated according to the procedure by Oliver and Pharr [50] described in Section 4.1.1. A mean elastic modulus is therefore taken from the average of the results.

With the elastic moduli of the films known, the method by Zhao et al. [73] is utilized to determine their yield stress, and work hardening exponent. In this analysis, the Young's modulus of the Si (100) substrate is taken to be 130 GPa [71]. Since there are only two unknowns to solve for, the problem considered in the original paper by Zhao et al. [73] can be reduced. The unloading curves obtained via nanoindentation describe purely elastic contact, thus it does not provide any data regarding the plastic properties of the film. The loading curve, however, is rich with information as the material undergoes plastic deformation during the initial indentation. Thus the shape factor which describes the unloading curve via the elastic recovery and unloading work is no longer used. By discarding Equation 4.12, the following two dimensionless functions are considered:

$$\ln\left(\frac{P_1}{\sigma_f d_1^2}\right) = f_1(\eta, n_f) \quad (4.14)$$

$$\ln\left(\frac{P_2}{\sigma_f d_2^2}\right) = f_2(\eta, n_f) \quad (4.15)$$

Note that the parameter $\xi = \ln(E_f/E_s)$ no longer appears as a variable in f_1 and f_2 since it is now a known constant. The two functions shown in Equations 4.14 and 4.15 are sufficient to determine σ_f and n_f of the films through the same principles described in Section 4.1.2. As before, a set of 10 indentations are conducted on both Al and Ti to a maximum depth of 670 nm (roughly $2h/3$). The loading profile follows the same strain rate and holding period as used with the shallow indentations. The relevant parameters

P_1 and P_2 are thus identified from the nanoindentation loading curve and used to calculate the shape factors. A new reduced error function is defined as follows:

$$\bar{e} = \left| \left(\ln \left\{ \frac{P_1}{\sigma_f d_1^2} \right\} - f_1(\eta, n_f) \right) / \ln \left(\frac{P_1}{\sigma_f d_1^2} \right) \right| + \left| \left(\ln \left\{ \frac{P_2}{\sigma_f d_2^2} \right\} - f_2(\eta, n_f) \right) / \ln \left(\frac{P_2}{\sigma_f d_2^2} \right) \right| \quad (4.16)$$

Similar to before, the set of (σ_f, n_f) that minimizes \bar{e} represents the plastic properties of the film. A genetic algorithm programmed in MATLAB is used to minimize the function in Equation 4.16 with respect to σ_f and n_f . In this problem, the number of design variables is 2 and a population size of 40 is used. For convergence, it is required that the best value of \bar{e} over the last 10 iterations have a standard deviation less than 10^{-10} . Since genetic algorithms are probabilistic, the code is executed 10 times to ensure consistent results. The yield stress and work hardening exponent is determined from each load-displacement curve and then averaged together to obtain mean values of σ_f and n_f .

4.2.2 Results and Discussion

Figures 4.4 (a) and (b) illustrate the loading and unloading curves produced by indenting a Berkovich tip to approximately 100 nm on Al and Ti respectively. Each line represents the data obtained from one of the 10 indentations. Very consistent load-displacement profiles are observed for Al. The loading curves and unloading slopes between all 10 curves are in excellent agreement with one another. Load-displacement curves for Ti,

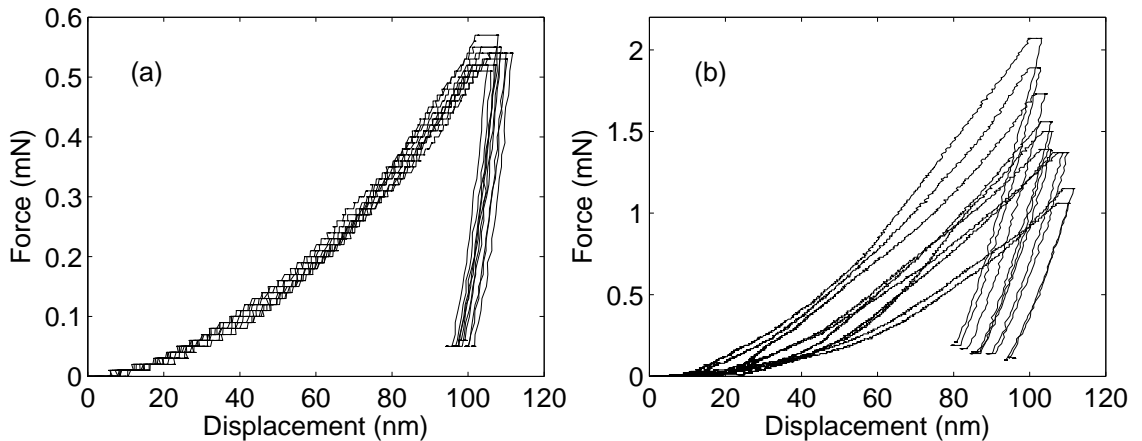


Figure 4.4: Ten load-displacement curves obtained from indenting a thin film of (a) Al and (b) Ti with a Berkovich tip to a maximum depth of roughly 100 nm.

however, exhibit large variability between runs due to the reasons unknown at this time. As the load is kept constant during the holding period, the material exhibits continued time-dependent deformations known as creep. This phenomenon is typically observed in nanoindentation experiments [18], but is ignored in the analysis by Oliver and Pharr [50] and Zhao et al. [73]. Following the method outlined in Section 4.1.1, P_{\max} , h_{\max} , and $S = dP/dh|_{h_{\max}}$ are extracted from each load-displacement curve and used to determine the average Young's modulus for both films. The average elastic modulus for Al and Ti is calculated to be 80 and 135 GPa with a standard deviation of 10 and 23 GPa respectively. Results from this analysis give Young's moduli that are slightly larger than bulk Al and Ti, which have values of 70 and 116 GPa respectively, but are of similar magnitude.

Deep indentations are performed on the metallic and Si film/substrate specimens to a maximum depth of approximately 670 nm. The resulting loading and unloading curves for Al and Ti are illustrated in Figures 4.5 (a) and (b) respectively which show similar characteristics to those obtained from shallow indentations. Creep is once again observed in both Al and Ti films during the holding period. The load-displacement curves between the 10 experiments are found to be consistent with each other for both Al and Ti, with the exception of those shown by dashed lines in Figure 4.5. These data sets show considerable deviation from the rest, and are therefore treated as outliers and discarded. The remaining curves are thus used to extract the yield stress and work hardening exponent of the thin films.

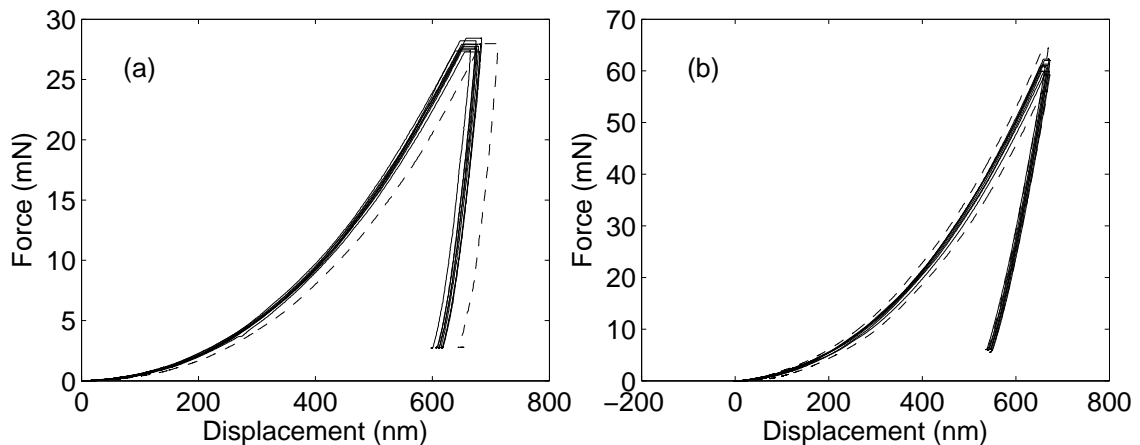


Figure 4.5: Nanoindentation load-displacement profiles obtained by indenting a thin film of (a) Al and (b) Ti to a depth of approximately 670 nm. Results from the ten indentations are shown, with outlying results illustrated in dashed lines.

Taking $E_f = 80$ GPa for Al, as determined above, σ_f and n_f are determined via the procedure described in Section 4.1.2. A genetic algorithm written in MATLAB is used to minimize the error function given by Equation 4.16, thus an optimal set of (σ_f, n_f) is obtained from each nanoindentation curve. The average yield stress and work hardening exponent for Al is calculated to be 0.80 ± 0.07 GPa and -0.039 ± 0.025 respectively, with the range of values indicating plus and minus one standard deviation. Repeating this analysis for Ti using $E_f = 135$ GPa gives $\sigma_f = 2.93 \pm 0.28$ GPa and $n_f = -0.130 \pm 0.028$. Stress-strain relationships resulting from the analysis of each load-displacement curve are illustrated by the blue lines in Figures 4.6 (a) and (b) for Al and Ti. The thicker red lines represent the average stress-strain curves having the mean values of σ_f and n_f . Two interesting characteristics are observed with the determined plastic properties of the films. First, the yield stresses obtained from the analysis are much higher than those of pure bulk Al and Ti which typically yield at approximately 20 MPa [14] and 190 MPa [7] respectively. The flow stresses of the thin films determined from nanoindentation are over an order of magnitude greater. Another note of interest is the negative work hardening exponent which indicates the material becomes softer as it is strained. This phenomenon has been observed in nanocrystalline Al with an average grain size of 150 nm [6]. Note that negative values of n_f were not considered in the study by Zhao et al. [73], therefore this result is an extrapolation of the data collected from their FE simulations.

To determine whether the determined elastoplastic properties are in fact representative of the thin films, FE simulations are performed in ABAQUS to mimic the nanoinden-

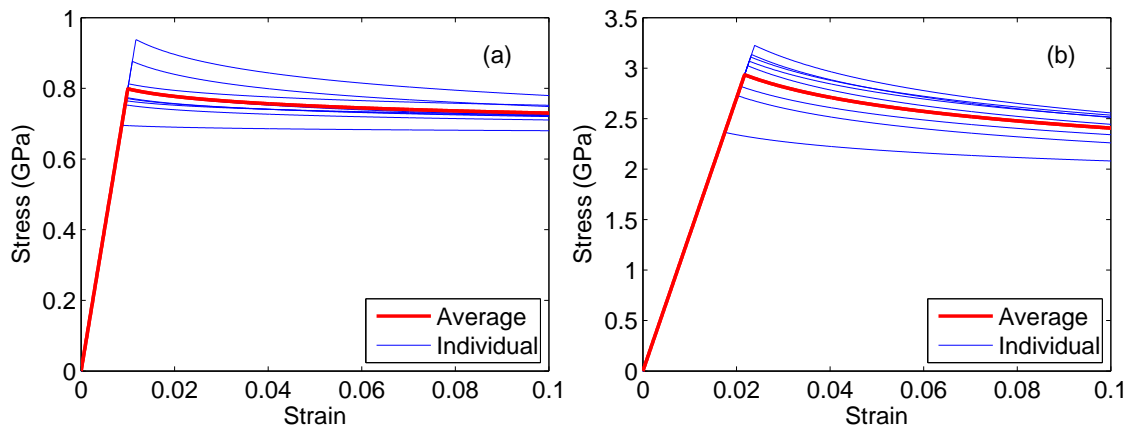


Figure 4.6: Stress-strain curves obtained from nanoindentation analysis for (a) Al and (b) Ti. Blue and red lines represent individual and averaged results respectively.

tation process. Similar to the study by Zhao et al. [73], a Berkovich indenter is described as a conical surface whose tip has a half angle of 70.3° in an axisymmetric model. The indenter is assumed to behave elastically with $E = 1140$ GPa and $\nu = 0.07$, the properties of diamond [37]. A thin film of either Al or Ti is modeled on top of a Si substrate, whose dimensions are taken to be 100 times the thickness of the film. Si is taken to behave elastically with a Young's modulus of 130 GPa as used in the initial analysis. The Al film is modeled as an elastic-plastic solid with the properties $E_f = 80$ GPa, $\sigma_f = 0.80$ GPa, and $n_f = -0.039$, with a stress-strain curve described by Equation 4.7. Similarly, the parameters $E_f = 135$ GPa, $\sigma_f = 2.93$ GPa, and $n_f = -0.130$ are used to model a Ti film. By applying a prescribed displacement to the indenter, the Berkovich tip is pushed into the films to the desired depth. The total reaction force on the bottom of the substrate gives the load applied by the indenter. Load-displacement curves from FE simulation are thus obtained for maximum indentation depths of 110 nm and 670 nm for both Al and Ti. The resulting curves are then compared to the data from experiments as shown in Figures 4.7 and 4.8 for Al and Ti respectively.

Shallow load-displacement profiles from experiment and FE analysis are compared in Figure 4.7 (a) for Al. The nanoindentation curve obtained via simulation appears wavy during loading due to the discretized meshing. Despite this fact, excellent congruency is found between the experimental and simulated load-displacement curves. Both the loading and unloading segments are accurately predicted and reproduced using the elastic-plastic properties of the Al film derived in the previous analysis. In Figure 4.7

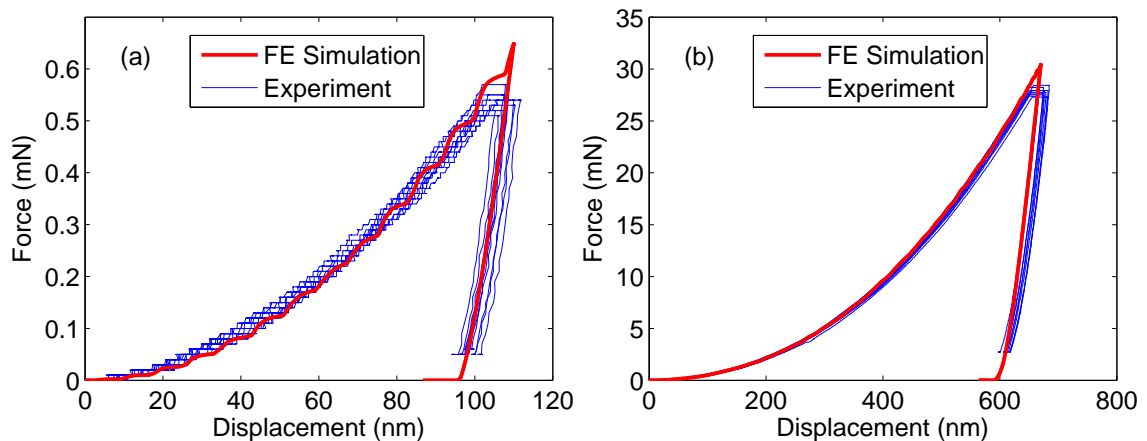


Figure 4.7: Experimental and simulated nanoindentation curves for (a) shallow and (b) deep indentations on Al.

(b), a comparison is made between the experimental and simulated deep nanoindentation curves for Al. Once again, an excellent correlation is observed between the load-displacement profiles during both loading and unloading. A minor discrepancy is noted in the lower portion of the unloading curve in Figure 4.7 (b), where the FE simulation predicts slightly less elastic recovery than those observed in experiments. The upper portion of the curve and initial unloading slope, however, are in excellent agreement. FE simulations using the extracted elastic-plastic properties of Al are found to produce load-displacement curves consistent with experiment, despite having extrapolated negative work hardening exponents. Thus the mechanical properties of the Al film determined from the reverse analysis have been validated.

Figure 4.8 (a) illustrates the simulated and experimental load-displacement curves from shallowly indenting a Ti thin film. Although the results from experimental nanoindentation show widespread variation, the FE loading and unloading curve appears to be situated in the middle. It can therefore be concluded that the solution from simulation is, on average, representative of the experimental data. Nanoindentation curves due to deep indentations into the Ti film are also compared in Figure 4.8 (b). Good agreement is noted between the experimental and simulated profiles upon initial loading. At larger displacements however, the results begin to deviate slightly. At a given indentation depth, forces predicted from the FE simulation are larger than those recorded from experiments. This difference grows to approximately 5% at the point of maximum depth and load.

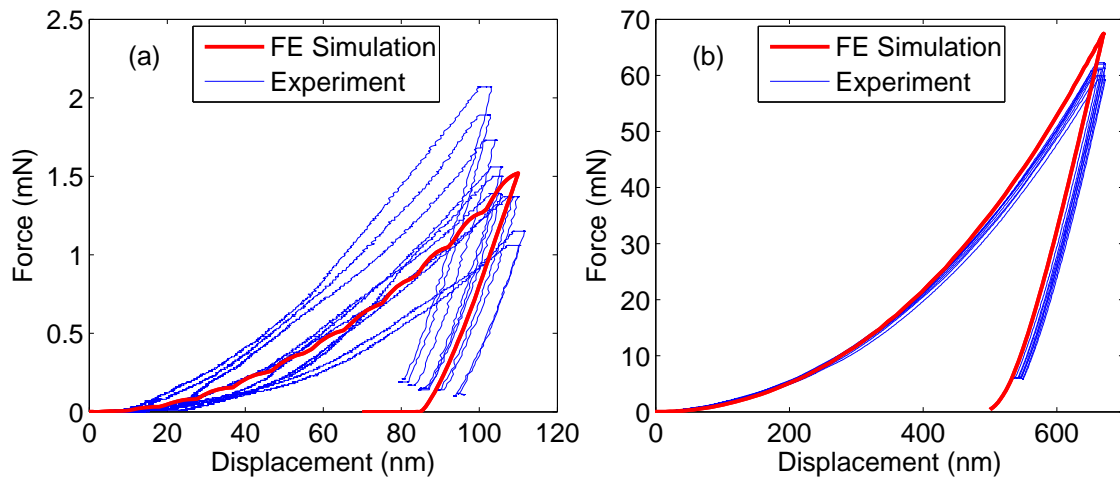


Figure 4.8: Experimental and simulated nanoindentation curves for (a) shallow and (b) deep indentations on Ti.

Unloading profiles from experimental data and FE simulation, however, show excellent agreement with the slopes matching throughout the entire unloading curve. The slight discord observed during the loading curve is within the standard deviation and error of the analysis, compounded with the fact that negative work hardening exponents have been extrapolated. Overall there is good agreement between the experimental and modeled results, and thus the elastoplastic properties of the Ti thin films are validated from this FE study.

Chapter 5

New Lattice Configuration with Low Thermal Expansion

Designs for microscale lattices that have near zero thermal expansion are described and analyzed in this Chapter. Two lattice configurations having near zero CTE are designed with the aid of FE simulations under different assumptions and presented in Section 5.1. An FE study is conducted on the two designs in Section 5.2 to validate and reveal the response of the lattice to thermal cycling.

5.1 Lattice Design

It is the goal in this section to design a bi-material lattice which exhibits near zero thermal expansion between 150–350 K, a conservative estimate of the expected temperature range experienced by the mirrors in the space telescope. The ideal configuration should also exhibit stable long term behaviour and achieve shakedown in a minimal number of thermal cycles. Due to a recent discovery, there is uncertainty in whether or not the thin films of Al and Ti are in fact amorphous. There exists the possibility that the metallic films are nanocrystalline with extremely fine grain sizes that have avoided detection thus far. Due to this unknown, two lattice configurations are designed under the assumption that the thin films are (i) amorphous, and (ii) nanocrystalline. In both scenarios, a lattice that is nearly solid has been put forth such that the empty spaces in the structure are kept to a minimum. The geometry of the proposed unit cell that is nearly filled is depicted in Figure 5.1 with red and blue structures representing Al and Ti respectively. In this design, a skewness angle of 30° is implemented to reduce the void

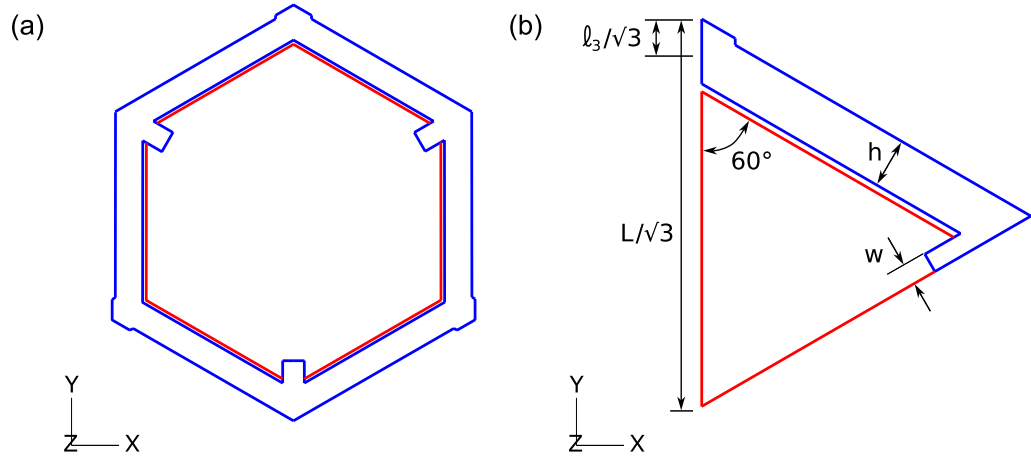


Figure 5.1: (a) Whole and (b) one sixth of a unit cell geometry with $\theta = 30^\circ$ that is nearly solid. Red and blue elements represent Al and Ti respectively.

regions in between adjacent unit cells. The Al constituents within the unit cell are also enlarged such that their shape follows that of the Ti lattice network. Small slits must be left between the Al and Ti members and in between adjacent cells to ensure there is no contact during thermal expansion. The configuration of the Al member has minimal influence on the thermal properties of the lattice given that it only contacts Ti at the three joints and behaves isotropically. The entire unit cell is depicted in Figure 5.1 (a) and one sixth of the unit cell modeled in ABAQUS, under the appropriate boundary conditions, is shown in Figure 5.1 (b). Important geometric parameters of the lattice which significantly affect its thermal expansion have also been identified and labeled. L and ℓ_3 represent the lengths of the unit cell and spacer as introduced before. The width of the Ti struts are identified as h , and the half-width of the joints are described by w . By tweaking the parameters ℓ_3/L , h , and w , a unit cell with $\theta = 30^\circ$ is designed to have near zero thermal expansion assuming either amorphous or nanocrystalline thin films.

5.1.1 Configuration Assuming Nanocrystalline Films

Working under the assumption that the thin films of Al and Ti are nanocrystalline, a microscale lattice is designed to have a CTE as close to zero as possible. The thermal expansion of nanocrystalline Al and Ti are assumed to be the same as their bulk polycrystalline forms, and are taken from the American Institute of Physics Handbook [30]. Although the stress-strain curves of the Al and Ti thin films were obtained via nanoindentation experiments in Chapter 4, the films were in an as-deposited state. To be more

realistic, the material properties of nanocrystalline Al and Ti are taken from literature where the grain sizes are larger, corresponding to an aged and annealed state. This is more representative of real world conditions where the metallic films will be subjected to thermal cycling and high temperatures. The stress-strain curves for nanocrystalline Al and Ti with an average grain size of roughly 100 nm are taken from the study by Khan et al. [35] and Sergueeva et al. [56] respectively to model Al and Ti.

The scaled theoretical thermal expansion of a lattice with spacers given by Equation 2.40 is used as a baseline in this design. Ultimately, however, iterative adjustments to the geometry through trial and error must be made due to slight discrepancies between the theoretical and actual joint configurations. The size of the spacer can be altered to either increase or decrease the net CTE of the lattice. Larger spacers will increase the overall CTE and vice versa. Adjustments to the width of Ti constituents can be made to change its aspect ratio. Recall that decreasing the slenderness ratio will soften the rotational resistance at the joints and lower the CTE of the lattice. Increasing the half-width of the joints adds to the bending inertia at the expansion joint and decreases the effective length of the Al members, thereby raising the overall CTE of the unit cell. The dimensions of the resulting configuration obtained through iteration are summarized in Table 5.1, and is hereby referred to as the nanocrystalline lattice.

Table 5.1: Dimensions of lattice with near zero CTE assuming nanocrystalline films.

θ (degrees)	L (μm)	ℓ_3/L	h (μm)	w (μm)
30	10	0.092	0.75	0.27

5.1.2 Configuration Assuming Amorphous Films

If the thin films of Al and Ti are in fact amorphous, their thermal expansion behaviour will differ from their crystalline forms and recrystallization will result in negative changes in volume. Although the recrystallization temperature of the films are predicted to be well above the working temperature range of the mirror, there is a chance that the lattice will recrystallize when the mirror segments are initially deployed. Since their orientations are not controlled upon deployment, the lattice may be subjected to direct sunlight, thus causing sufficiently high temperatures to induce devitrification. In this analysis it is assumed that through thermal cycling, the amorphous constituents will undergo complete recrystallization, thus resulting in a nanocrystalline structure. The

long term thermal properties of the lattice are therefore investigated in this approach. Information obtained from MD simulations in Chapter 3 are used in conjunction with FE analyses to study the behaviour of the unit cell and predict its thermal properties. The amorphous CTEs of Al and Ti are used to describe their thermal expansion prior to recrystallization, and the linear expansion coefficients due to recrystallization are used to emulate their behaviour during the phase transition. After the amorphous films have crystallized, the CTEs of Al and Ti from the American Institute of Physics Handbook [30] are used to describe their thermal expansion. In this approach, it is also assumed that the elastic-plastic properties of Al and Ti are independent of temperature, and are taken to be those of ultra-fine grained Al and Ti as used in the analysis of the nanocrystalline lattice.

Similar to before, Equation 2.40 is used as a guideline for estimating the thermal properties of the lattice. Adjustments must be made to the geometry, however, to account for the recrystallization of amorphous Al and Ti, in addition to the differences in the joint configuration. Al undergoes large changes in volume due to devitrification, therefore alterations to the lattice geometry are required to compensate for this distortion. Through an iterative process, the lattice parameters are fine tuned to obtain the desired changes in net CTE. Table 5.2 summarizes the dimensions of a unit cell that, in the long term, has nearly zero thermal expansion while assuming recrystallization of the amorphous constituents. This lattice design is hereby denoted the amorphous lattice.

Table 5.2: Dimensions of lattice with near zero CTE assuming amorphous films.

θ (degrees)	L (μm)	ℓ_3/L	h (μm)	w (μm)
30	10	0.072	0.55	0.20

5.2 FE Analysis of Lattice

5.2.1 Method

The two configurations presented in Section 5.1 are modeled and analyzed via FE simulations in ABAQUS. Details of the FE model are similar to those described in Section 2.3. Only one sixth of the unit cell is modeled using the appropriate boundary conditions, thus saving computational resources and time. Plane stress elements are used to model

the two constituents, which are taken to behave isotropically. As stated earlier, the elastic-plastic properties of Al and Ti are taken from Khan et al. [35] and Sergueeva et al. [56] respectively. It is assumed here that the Al and Ti members are bonded at the interface, therefore the degrees of freedom of the nodes at the joint are tied together.

To analyze the thermal properties of the unit cell, the temperature is cycled between 150 K and 350 K for 5 iterations to confirm shakedown of the lattice and stable long term behaviour. It is assumed that the lattice is undeformed and free of stresses at 293 K. The change in unit cell length dL , is recorded as a function of temperature over the course of the simulation. This quantity is then normalized with respect to the original length of the unit cell L_o . The derivative of this curve will therefore give the CTE of the lattice as a function of temperature. For the nanocrystalline lattice, the material properties will remain constant throughout the entire simulation. In the case of the amorphous lattice however, the thermal properties of the constituents will change as they undergo devitrification. In the analysis of the amorphous lattice, recrystallization is first induced by cycling the unit cell between 293–673 K.

During the initial heating of the amorphous lattice, the CTEs of Al and Ti constituents are taken from the results of the MD study in Chapter 3. Once T_x is reached for either Al or Ti, the material undergoes an amorphous to crystalline transition. In this stage, the values of α_r calculated in Section 3.2 are used to simulate the contraction of Al and Ti due to devitrification. When the temperature equals T_{x2} for either Al or Ti, it is assumed that the material has completely crystallized. The CTEs of crystalline Al and Ti from the American Institute of Physics Handbook [30] are therefore used to describe the thermal properties of both constituents from there forward. In order to accommodate these changes in material properties, the FE simulation is divided into 5 steps during the initial thermal cycle as summarized in Table 5.3, with the thermal properties listed for

Table 5.3: Thermal properties of amorphous lattice during initial thermal cycle.

Step	Temperature Range (K)	Al	Ti
1	293–450	Amorphous	Amorphous
2	450–550	Transition	Amorphous
3	550–650	Crystalline	Transition
4	650–673	Crystalline	Crystalline
5	673–293	Crystalline	Crystalline

Al and Ti. Once the amorphous lattice has undergone devitrification, the temperature is varied from 150 K to 350 K for 5 cycles and the same analysis as described for the nanocrystalline lattice is performed.

5.2.2 Results and Discussion

Nanocrystalline Lattice

Thermal cycling of the nanocrystalline lattice between 150–350 K reveals that the maximum stresses within the structure do not exceed the flow stresses for either material, thus repeatable behaviour is observed over the 5 cycles. The deformed state and stress distribution within the lattice at 150 K, the temperature with maximum internal stresses, is illustrated in Figure 5.2. Stress buildup is found in the Ti member due to bending, and at the material interface due to the mismatch in CTE. A maximum stress of approximately 126 MPa occurs around the joint, but is below the yield stress of both Al and Ti. Deformations within the unit cell are subtle and hard to detect, despite having multiplied the displacements by a factor of 3 for exaggeration. The variation in unit cell length with respect to temperature is illustrated in Figure 5.3 by the blue line. Small changes in L are found over the simulated temperature range. Sinusoidal behaviour is noted because the CTEs of Al and Ti vary over the temperature range of 150–350 K, thereby changing the ratio α_2/α_1 . A polynomial interpolant is fitted to the curve dL/L_0

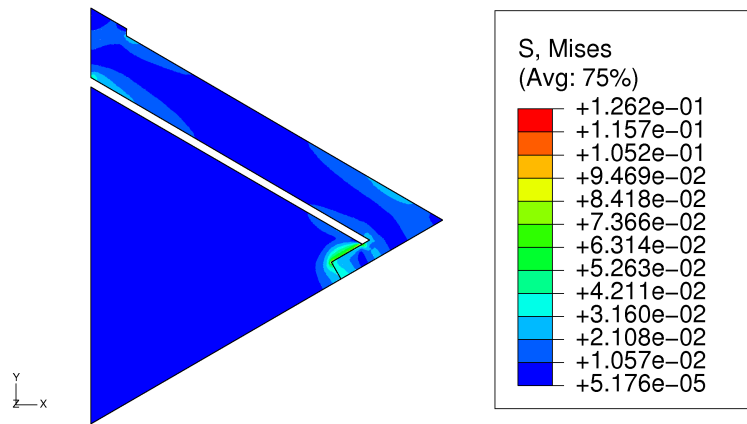


Figure 5.2: Stresses within the deformed unit cell structure at 150 K are illustrated by the coloured bands and have units of GPa. The displacements have been exaggerated by a factor of 3 to clearly show deformations.

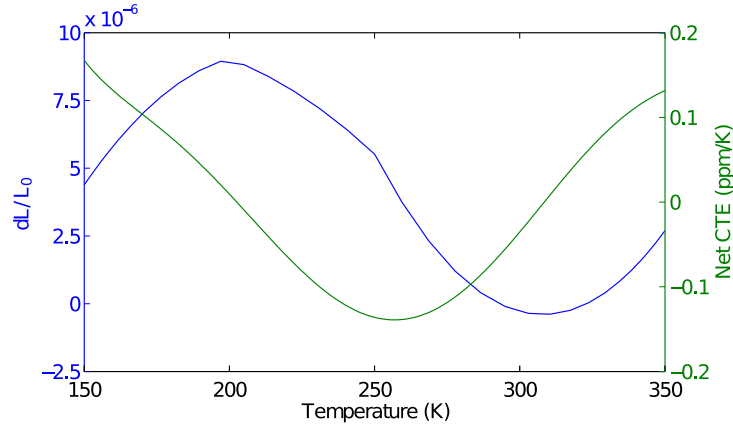


Figure 5.3: dL/L_0 and $\bar{\alpha}$ of nanocrystalline lattice plotted as a function of temperature in blue and green respectively between 150–350 K.

versus T , and the derivative is computed to determine the CTE of the lattice as shown by the green line in Figure 5.3. The CTE of the lattice is found to be very close to zero, and varies between +0.17 and -0.14 ppm/K over the simulated temperature range. The variation in $\bar{\alpha}$ is again due to the temperature dependent thermal expansion of Al and Ti. Since $\Sigma = \alpha_2/\alpha_1$ is not constant, it is difficult to create a lattice with exactly zero CTE over large ranges of temperature. The thermal expansion of the proposed nanocrystalline lattice, however, is only a fraction of 1 ppm/K in the worst case scenario, and can be considered a successful lattice design with near zero CTE.

Amorphous Lattice

To examine the thermal properties of the amorphous lattice configuration, the unit cell is first cycled from 293–673 K to induce recrystallization. Due to the large displacements in this process, significant internal stresses are created which ultimately lead to plasticity and permanent deformations in the structure. Figure 5.4 illustrates the evolution of the displacements and stress distribution within the unit cell during the initial heating cycle. Snapshots are taken at the beginning of the simulation and at the end of the 5 steps listed in Table 5.3. Deformations are scaled by a factor of 3 for clarity and stresses within the unit cell are colour coded by intensity. At the start of the simulation when $T = 293$ K, the unit cell is undeformed and thus there are no internal stresses and strains. Between 293–450 K, amorphous Al and Ti expand according to the CTEs derived from MD simulations. A slight buildup of internal stresses can be observed near the joint between Al and Ti

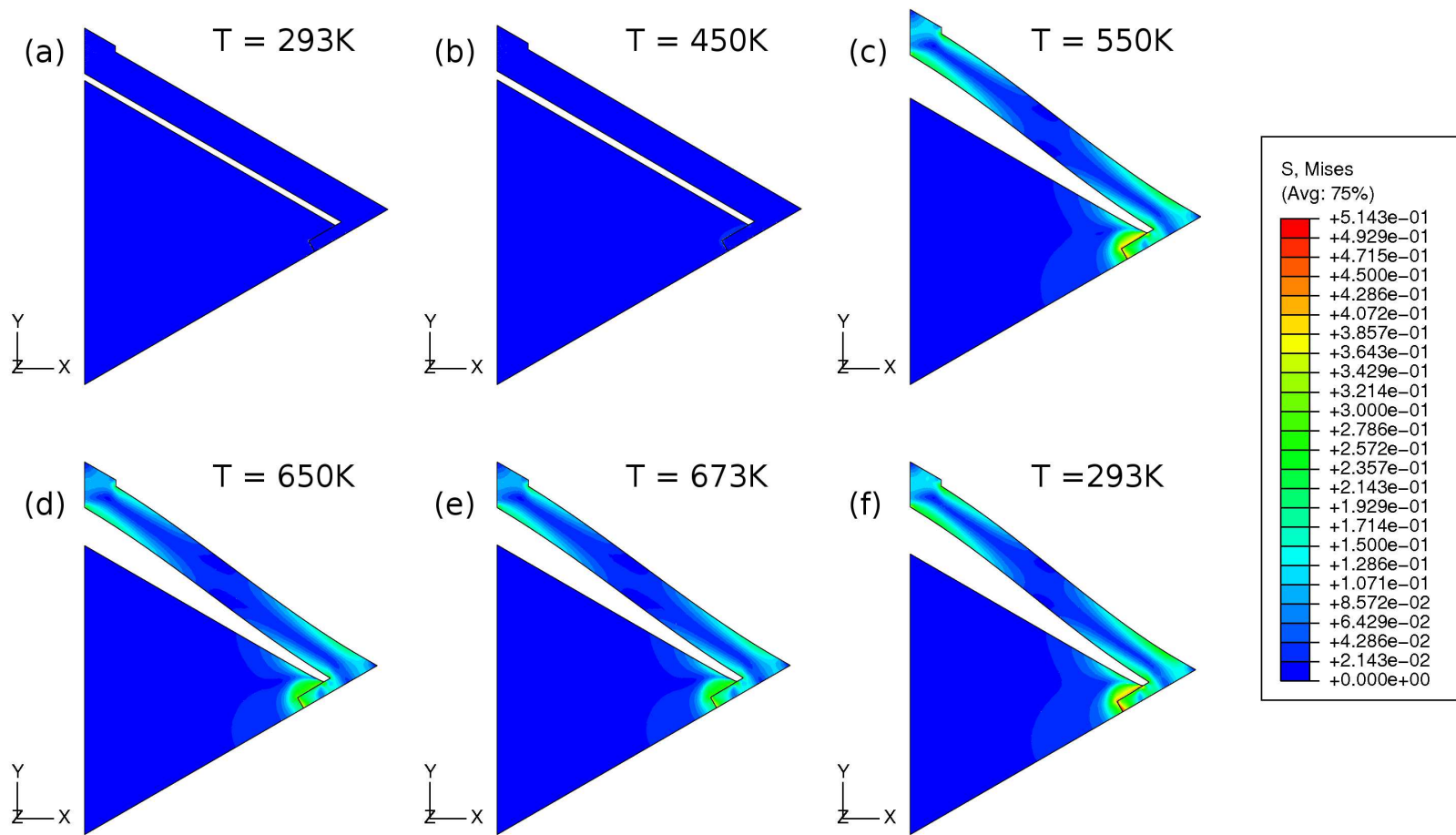


Figure 5.4: Figures (a) to (f) illustrate the evolution of the unit cell as the temperature is cycled between 293 K and 673 K. Displacements are exaggerated by a factor of 3 to clearly show displacements within the unit cell. The internal von Mises stresses (in GPa) are indicated by the colour bands whose values are given in the legend on the right.

in Figure 5.4 (b). Past 450 K, amorphous Al begins to recrystallize, thus from 450–550 K the Al constituent is shrinking while Ti continues to expand. This mismatch causes Al to pull inward on the Ti member, causing the bending shown in Figure 5.4 (c). High stresses are seen in Ti due to the large displacements in Al, and large thermal mismatch is noted at the interface. Between 550 K and 650 K, Al expands as though it were crystalline while Ti contracts slightly during its transition in phase. As a result of this behaviour, the stresses created from the previous step are somewhat alleviated as the geometric discrepancies are lessened as shown in Figure 5.4 (d). At 650 K, amorphous Ti is assumed to have completely recrystallized. Thus from here forward, both constituents take on the thermal properties of crystalline materials. Figure 5.4 (e) depicts the unit cell at $T = 673$ K, which shows little difference in comparison to the previous state due to the small change in temperature and lower CTE mismatch. After the heating stage is complete, the temperature of the unit cell is brought back down to 293 K. Al has a higher CTE than Ti and therefore contracts at a faster rate. Over the 380 K temperature range, the Al constituent recedes significantly more than Ti. This mismatch in CTE aggravates the already distorted unit cell to create even higher stresses at the joint. Large stress concentrations near the material interface can be seen in Figure 5.4 (f) which illustrates the unit cell at room temperature after the initial heating cycle. Significant residual stresses and strains are observed within the unit cell after the lattice has recrystallized. This is mainly due to the devitrification of Al which shrinks immensely, thus leading to large distortions and bending in the structure.

Figure 5.5 plots the change in unit cell length versus temperature over the course of recrystallization. The discontinuous line segments correspond to the different steps in

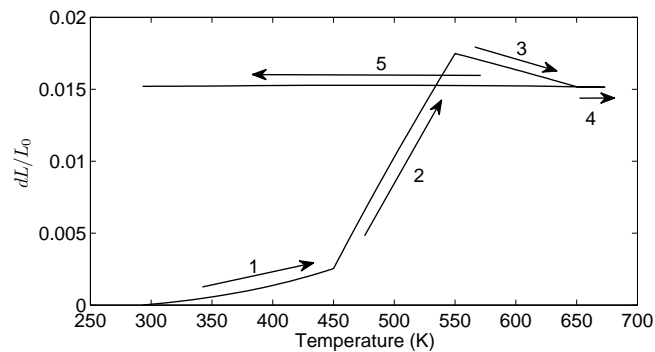


Figure 5.5: Plot of dL/L_0 during the initial heating cycle from 293–673 K with the 5 stages labeled and arrows indicating the progression in time.

the analysis where there are abrupt changes in material properties. Arrows and numbers are used to indicate the direction of increasing time and identify the corresponding step. During the first step, the thermal expansion of the unit cell is observed to be rather large since the CTEs of amorphous Al and Ti do not form the ideal ratio of roughly 2.5. As amorphous Al recrystallizes during step number 2, a very large increase in L is noted. When the Al member contracts inward, it causes rotations of the Ti members which push the lattice nodes outward, thereby increasing the overall length of the unit cell. At 550 K, Al has crystallized and Ti undergoes devitrification, thus a trend reversal occurs. The Ti constituents rotate in the opposite direction and the lattice nodes are drawn inward. As a result, the length of the unit cell shrinks as noted by the negative slope of the third line segment. During steps 4 and 5, Al and Ti constituents behave as crystalline materials, thus their ratio of CTEs is ideal. As the temperature increases, and decreases, there is little change in the length of the unit cell and lines 4 and 5 are nearly flat. Their zero slopes indicate that the unit cell has near zero CTE. Thus, as the unit cell is initially heated and the constituents recrystallize, the CTE varies between positive and negative values and is far from zero. The lattice exhibits the property of low thermal expansion only after the materials have crystallized to give the ideal ratio of CTEs. As a result of recrystallization however, the unit cell becomes distorted due to extreme changes in the Al members. The residual stress and strain in the structure causes the unit cell to grow by approximately 1.5% from its original length as seen in Figure 5.5.

After the amorphous lattice has recrystallized, the unit cell is cycled between 150 K and 350 K for 5 iterations to examine its thermal behaviour. The resulting change in unit cell size as a function of temperature is plotted in Figure 5.6. In this figure, the value of

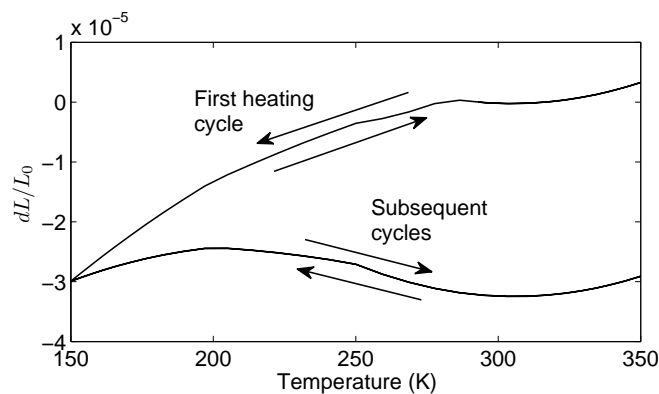


Figure 5.6: Plot of dL/L_0 versus T over the 5 thermal cycles between 150–350 K.

dL/L_0 at the beginning of the simulation ($T = 293$ K) is set to zero to show the relative changes in L after recrystallization. During the first cycle, the temperature is increased to 350 K and then dropped to 150 K, during which the lattice expands and shrinks. Upon contraction, large internal stresses develop at the joint which causes further plastic deformation near the interface. During the next heating cycle, the thermal expansion of the unit cell is observed to follow a different path from the first. The remaining cycles after the first show repeatable behaviour, indicating that plastic shakedown has occurred. Extremely small and constant changes are noted, however, between subsequent cycles after the first, but are attributed to numerical error and ignored. The stable thermal behaviour is plotted and analyzed in Figure 5.7. dL/L_0 at 293 K is set to zero in this plot to act as a reference point. Sinusoidal expansion is observed, similar to the behaviour of the nanocrystalline lattice. Again, this is attributed to the changing thermal properties of Al and Ti. Like before, the CTE of the lattice is calculated by fitting a polynomial to the curve dL/L_0 versus T and taking its derivative. The resulting CTE of the amorphous lattice between 150 K and 350 K is illustrated by the green line in Figure 5.7. For the amorphous configuration, its CTE is observed to vary between +0.19 and -0.13 ppm/K, similar to that of the nanocrystalline configuration. Thus through iterative designs, an amorphous lattice which undergoes recrystallization and shakedown has been successfully proposed which exhibits long term near zero thermal expansion.

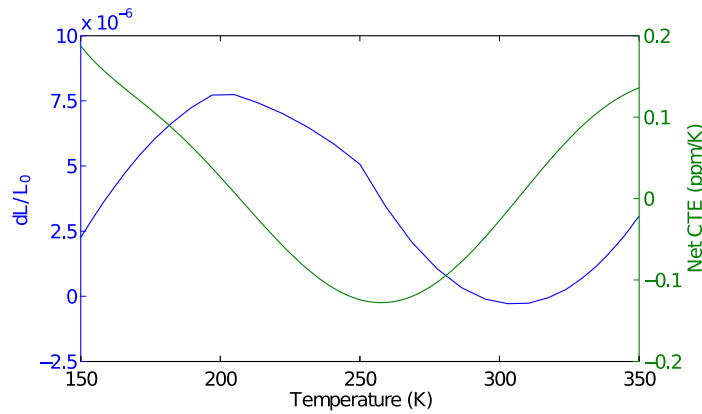


Figure 5.7: dL/L_0 and $\bar{\alpha}$ of amorphous lattice plotted as a function of temperature in blue and green respectively between 150–350 K.

Chapter 6

Conclusions

6.1 Summary of Research

Materials with low CTE are desired to minimize thermal stresses and strains and preserve geometric stability. In this thesis, the concepts of low thermal expansion lattices have been utilized at the microscale to design a thermally stable material for the application of optical elements in a space telescope. The key and original works of research that have aided this development are summarized as follows:

1. The influence of spacers on the thermal properties of a unit cell was studied. An analytical expression for the net CTE of a lattice with spacers was derived for both pinned and bonded joint configurations, and validated using FE simulations.
2. MD simulations were conducted to study the thermal expansion and recrystallization of amorphous Al and Ti. From simulation data, the CTEs of the amorphous metals were calculated and shown to differ from their crystalline counterparts. The contraction in length during devitrification and the temperature at which recrystallization occurred were also quantified in this study.
3. The mechanical properties of Al and Ti films have been determined via nanoindentation experiments. Load-displacement profiles produced by a Berkovich indenter were analyzed to deduce the Young's moduli and plastic properties of the films. The extracted mechanical properties were subsequently validated by simulating the nanoindentation process via FE models and comparing the resulting loading and unloading curves.
4. Two unit cell configurations assuming different material properties were designed

with the aid of FE simulations. Both lattices have been shown to exhibit near zero thermal expansion and long term stability, achieving shakedown in one thermal cycle or less.

6.2 Recommendations for Future Work

Numerous avenues of research remain open for further exploration and study. A few are listed here as follows:

1. Validate simulated findings in this thesis through experimental means.
2. Study the impact of oxidation on mechanical/thermal properties and reliability of lattice.
3. Perform a statistical analysis on the thermal properties of the lattice given variations in the unit cell geometry and material properties.
4. Develop an optimization algorithm which provides the best unit cell design to achieve the desired net CTE.
5. Investigate the use of different material combinations.

Bibliography

- [1] G. J. Ackland. Theoretical study of titanium surfaces and defects with a new many-body potential. *Philos. Mag. A*, 66:917–932, 1992.
- [2] B. J. Alder and T. E. Wainwright. Phase transition for a hard sphere system. *J. Chem. Phys.*, 27:1208–1209, 1957.
- [3] H. E. Alper and P. Politzer. Molecular Dynamics Simulations of the Temperature-Dependent Behavior of Aluminum, Copper, and Platinum. *Int. J. Quantum Chem.*, 76:670–676, 2000.
- [4] C. S. Becquart, P. C. Clapp, M. V. Glazon, and J. A. Rifkin. Molecular dynamics simulations of amorphisation in Al and Ni₃Al. *Comp. Mater. Sci.*, 1:411–418, 1993.
- [5] J. Berger, C. Mercer, R. M. McMeeking, and A. G. Evans. The Design of Bonded Bimaterial Lattices that Combine Low Thermal Expansion with High Stiffness. In Press, 2011.
- [6] S. Billard, J. P. Fondère, B. Bacroix, and G. F. Dirras. Macroscopic and microscopic aspects of the deformation and fracture mechanisms of ultrafine-grained aluminum processed by hot isostatic pressing. *Acta Mater.*, 54:411–421, 2005.
- [7] H. E. Boyer, editor. *Atlas of Stress-Strain Curves*. ASM International, 1987.
- [8] W. D. Callister. *Materials Science and Engineering: An Introduction*. John Wiley & Sons, Inc., 7th edition, 2007.
- [9] A. Cao and Y. Wei. Atomistic simulations of the mechanical behavior of fivefold twinned nanowires. *Phys. Rev. B*, 74, 2006.
- [10] F. A. Celik, S. Ozgen, and A. K. Yildiz. Molecular dynamics study on intermediate structures during transition from amorphous to crystalline state. *Mol. Simul.*, 32(6):443–449, 2006.
- [11] M. Chandross, C. D. Lorenz, M. J. Stevens, and G. S. Grest. Simulations of Nanotribology with Realistic Probe Tip Models. *Langmuir*, 24:1240–1246, 2008.
- [12] H. Chen, Y. He, G. J. Shiflet, and S. J. Poon. Deformation-induced nanocrystal

- formation in shear bands of amorphous alloys. *Nature*, 367:541–543, 1994.
- [13] Y. T. Cheng and C. M. Cheng. Can stress–strain relationships be obtained from indentation curves using conical and pyramidal indenters? *J. Mater. Res.*, 14(9):3493–3496, 1999.
- [14] N. Q. Chinh, G. Horváth, Z. Horita, and T. G. Langdon. A new constitutive relationship for the homogeneous deformation of metals over a wide range of strain. *Acta Mater.*, 52:3555–3563, 2004.
- [15] Dassault Systèmes Simulia Corp. Abaqus/CAE 6.8–4, 2009. Providence, RI.
- [16] M. S. Daw and M. I. Baskes. Embedded-atom method: Derivation and application to impurities, surfaces, and other defects in metals. *Phys. Rev. B*, 29(12):6443–6453, 1983.
- [17] V. S. Deshpande, M. F. Ashby, and N. A. Fleck. Foam topology: bending versus stretching dominated architectures. *Acta Mater.*, 49:1035–1040, 2001.
- [18] M. F. Doerner and W. D. Nix. A method for interpreting data from depth-sensing indentation instruments. *J. Mater. Res.*, 1(4):601–609, 1986.
- [19] Y. Duan and P. A. Kollman. Pathways to a protein folding intermediate observed in a 1-microsecond simulation in aqueous solution. *Science*, 282:740, 1998.
- [20] *Invar 36 Technical Data*. Electronic Space Products International, Ashland, Oregon, USA, 2010.
- [21] F. Ercolessi. A molecular dynamics primer, 1997. International School for Advanced Studies. Trieste, Italy.
- [22] F. Ercolessi and J. B. Adams. Interatomic potentials from first-principles calculations: the Force-Matching method. *Europhys. Lett.*, 26(8):583–588, 1994.
- [23] M. W. Finnis and J. E. Sinclair. A simple empirical N-body potential for transition metals. *Philos. Mag. A*, 50(1):45–55, 1984.
- [24] Y. Gan and J. K. Chen. Molecular dynamics study of size, temperature and rate dependent thermomechanical properties of copper nanofilms. *Mech. Res. Commun.*, 36:838–844, 2009.
- [25] C. W. Gear. *Numerical Initial Value Problems in Ordinary Differential Equations*. Prentice-Hall, Englewood Cliffs, NJ., 1973.
- [26] N. M. Ghoniem, E. P. Busso, N. Kioussis, and H. Huang. Multiscale modelling of nanomechanics and micromechanics: an overview. *Philos. Mag.*, 83(31–34):3475–3528, 2003.
- [27] L. V. Gibiansky and S. Torquato. Thermal expansion of isotropic multiphase com-

- posites and polycrystals. *J. Mech. Phys. Solids*, 45(7):1223–1252, 1997.
- [28] J. B. Gibson, A. N. Goland, M. Milgram, and G. H. Vineyard. Dynamics of Radiation Damage. *Phys. Rev.*, 120(4):1229–1253, 1960.
- [29] L. J. Gibson and M. F. Ashby. *Cellular solids: structures and properties*. Cambridge University Press, second edition, 1997.
- [30] D. E. Gray, editor. *American Institute of Physics Handbook*. McGraw-Hill, 3rd edition, 1972.
- [31] W. Humphrey, A. Dalke, and K. Schulten. VMD: Visual molecular dynamics. *J. Mol. Graphics*, 14(1):33–38, 1996.
- [32] The MathWorks Inc. MATLAB 7.7.0 (R2008b), 2008. Natick, MA.
- [33] G. Jefferson, T. A. Parthasarathy, and R. J. Kerans. Tailorable thermal expansion hybrid structures. *Int. J. Solids Struct.*, 46:2372–2387, 2009.
- [34] J. E. Jones. On the determination of molecular fields: II. From the equation of state of a gas. *Proc. R. Soc.*, 106:463–77, 1924.
- [35] A. S. Khan, Y. S. Suh, X. Chen, L. Takacs, and H. Zhang. Nanocrystalline aluminum and iron: Mechanical behavior at quasi-static and high strain rates, and constitutive modeling. *Int. J. Plasticity*, 22:195–209, 2006.
- [36] M. L. Klein and W. Shinoda. Large-Scale Molecular Dynamics Simulations of Self-Assembling Systems. *Science*, 321:798, 2008.
- [37] J. A. Knapp, D. M. Follstaedt, S. M. Myers, J. C. Barbour, and T. A. Friedmann. Finite-element modeling of nanoindentation. *J. Appl. Phys.*, 85(3):1460–1474, 1998.
- [38] R. Lakes. Cellular solid structures with unbounded thermal expansion. *J. Mater. Sci. Lett.*, 15:475–477, 1996.
- [39] J. C. S. Lévy and D. Mercier. Amorphous structures: A local analysis. *J. Appl. Phys.*, 53(11):7709–7712, 1982.
- [40] X. Y. Liu, F. Ercolessi, and J. B. Adams. Aluminium interatomic potential from density function theory calculations with improved stacking fault energy. *Modell. Simul. Mater. Sci. Eng.*, 12:665–670, 2004.
- [41] Y. Liu, B. Wang, M. Yoshino, S. Roy, H. Lu, and R. Komanduri. Combined numerical simulation and nanoindentation for determining mechanical properties of single crystal copper at mesoscale. *J. Mech. Phys. Solids*, 53:2718–2741, 2005.
- [42] C. Loken, D. Gruner, L. Groer, R. Peltier, N. Bunn, M. Craig, T. Henriques, J. Dempsey, C. H. Yu, J. Chen, L. J. Dursi, J. Chong, S. Northrup, J. Pinto, N. Knecht, and R. Van Zon. Scinet: Lessons learned from building a power-efficient

- top-20 system and data centre. *J. Phys.: Conf. Ser.*, 256(1):012026, 2010.
- [43] J. Lu and J. A. Szpunar. Molecular-dynamics simulation of rapid solidification of aluminum. *Acta Metall. Mater.*, 41(8):2291–2295, 1993.
- [44] J. Lu and J. A. Szpunar. Molecular dynamics simulations on crystallization of amorphous Al. *Scr. Metall. Mater.*, 32(12):1957–1963, 1995.
- [45] K. Lu. Nanocrystalline metals crystallized from amorphous solids: nanocrystallization, structure, and properties. *Mater. Sci. Eng. R*, 16(4):161–221, 1996.
- [46] M. I. Mendeleev, D. J. Srolovitz, G. J. Ackland, and S. Han. Effect of Fe segregation on the migration of a non-symmetric $\Sigma 5$ tilt grain boundary in Al. *J. Mater. Res.*, 20(1):208–218, 2005.
- [47] P. M. Morse. Diatomic molecules according to the wave mechanics:II. Vibrational levels. *Phys. Rev.*, 34:57–64, 1929.
- [48] D. J. Oh and R. A. Johnson. Simple embedded atom method model for fcc and hcp metals. *J. Mater. Res.*, 3(3):471–478, 1988.
- [49] W. C. Oliver and G. M. Pharr. Measurement of hardness and elastic modulus by instrumented indentation: Advances in understanding and refinements to methodology. *J. Mater. Res.*, 19(1):3–20, 2004.
- [50] W. C. Oliver and G. M. Pharr. An improved technique for determining hardness and elastic modulus using load and displacement sensing indentation experiments. *J. Mater. Res.*, 7(6):1564–1583, 1992.
- [51] Q. X. Pei, C. Lu, and M. W. Fu. The rapid solidification of Ti_3Al : a molecular dynamics study. *J. Phys. Condens. Matter*, 16:4203–4210, 2004.
- [52] Q. X. Pei, C. Lu, and H. P. Lee. Crystallization of amorphous alloy during isothermal annealing: a molecular dynamics study. *J. Phys. Condens. Matter*, 17:1493–1504, 2005.
- [53] G. M. Pharr, W. C. Oliver, and F. R. Brotzen. On the generality of the relationship among contact stiffness, contact area, and elastic modulus during indentation. *J. Mater. Res.*, 7(3):613–617, 1992.
- [54] S. Plimpton. Fast Parallel Algorithms for Short-Range Molecular Dynamics. *J. Comput. Phys.*, 117:1–19, 1995. URL <http://lammps.sandia.gov/index.html>.
- [55] J. Roth, F. Gahler, and H. R. Trebin. A molecular dynamics run with 5.180.116.000 particles. *Int. J. Mod. Phys. C*, 11:317–322, 2000.
- [56] A. V. Sergueeva, V. V. Stolyarov, R. Z. Valiev, and A. K. Mukherjee. Advanced mechanical properties of pure titanium with ultrafine grained structure. *Scr. Mater.*,

- 45:747–752, 2001.
- [57] M. Shimono and H. Onodera. Molecular dynamics study on formation and crystallization of Ti–Al amorphous alloys. *Mater. Sci. Eng.*, A304–306:515–519, 2001.
- [58] O. Sigmund and S. Torquato. Design of materials with extreme thermal expansion using a three-phase topology optimization method. *J. Mech. Phys. Solids*, 45(6):1037–1067, 1997.
- [59] N. N. Sirota and T. E. Zhabko. X-ray study of the anisotropy of thermal properties in titanium. *Phys. Status Solidi A*, 63(2):K211–K215, 1980.
- [60] I. N. Sneddon. The relation between load and penetration in the axisymmetric Boussinesq problem for a punch of arbitrary profile. *Int. J. Eng. Sci.*, 3(1):47–57, 1965.
- [61] C. A. Steeves, S. L. dos Santos e Lucato, M. He, E. Antinucci, J. W. Hutchinson, and A. G. Evans. Concepts for structurally robust materials that combine low thermal expansion with high stiffness. *J. Mech. Phys. Solids*, 55:1803–1822, 2007.
- [62] C. A. Steeves, C. Mercer, E. Antinucci, M. Y. He, and A. G. Evans. Experimental investigation of the thermal properties of tailored expansion lattices. *Int. J. Mech. Mater. Des.*, 5:195–202, 2009.
- [63] G. Sutmann. Classical Molecular Dynamics. In J. Grotendorst, D. Marx, and A. Muramatsu, editors, *Quantum Simulations of Complex Many-Body Systems: From Theory to Algorithms*, pages 211–254. John von Neumann Institute for Computing, Jülich, Germany, 2002. NIC Series, Vol. 10, ISBN 3-00-009057-6.
- [64] J. Tersoff. Empirical interatomic potential for silicon with improved elastic properties. *Phys. Rev. B*, 38(14):9902–9905, 1988.
- [65] V. Timon, S. Brand, S. J. Clark, and R. A. Abram. Molecular dynamics calculations of the thermal expansion properties and melting points of Si and Ge. *J. Phys. Condens. Matter*, 18:3489–3498, 2006.
- [66] T. Y. Tsui and G. M. Pharr. Substrate effects on nanoindentation mechanical property measurement of soft films on hard substrates. *J. Mater. Res.*, 14(1):292–301, 1999.
- [67] A. A. Valladares. Generating amorphous and liquid aluminum: A new approach. *J. Non-Cryst. Solids*, 353:3540–3544, 2007.
- [68] L. Verlet. Computer ‘Experiments’ on Classical Fluids. I. Thermodynamical Properties of Lennard-Jones Molecules. *Phys. Rev.*, 159(1):98, Jul 1967.
- [69] D. D. Vvedensky. Multiscale modelling of nanostructures. *J. Phys. Condens. Matter*,

- 16:R1537–R1576, 2004.
- [70] A. J. C. Wilson. The thermal expansion of aluminium from 0° to 650° c. *Proc. Phys. Soc.*, 53(3):235, 1941.
- [71] C. J. Wilson and P. A. Beck. Fracture Testing of Bulk Silicon Microcantilever Beams Subjected to a Side Load. *J. Microelectromech. Syst.*, 5(3):142–150, 1996.
- [72] M. Zhao, X. Chen, N. Ogasawara, A. C. Razvan, N. Chiba, D. Lee, and Y. X. Gan. New sharp indentation method of measuring the elastic–plastic properties of compliant and soft materials using the substrate effect. *J. Mater. Res.*, 21(12):3134–3151, 2006.
- [73] M. Zhao, X. Chen, Y. Xiang, J. J. Vlassak, D. Lee, N. Ogasawara, N. Chiba, and Y. X. Gan. Measuring elastoplastic properties of thin films on an elastic substrate using sharp indentation. *Acta Mater.*, 55:6260–6274, 2007.
- [74] R. R. Zope and Y. Mishin. Interatomic potentials for atomistic simulations of the Ti-Al system. *Phys. Rev. B*, 68:024102, 2003.